

INFILTRATION OF DEFORMABLE POROUS MEDIA

by

Jared Lee Sommer

B.S. Metallurgy, University of Utah, 1985

Submitted to the Department of
Materials Science and Engineering
in Partial Fulfillment of the Requirements for the Degree of

DOCTOR OF PHILOSOPHY

at the

MASSACHUSETTS INSTITUTE OF TECHNOLOGY

February 1992

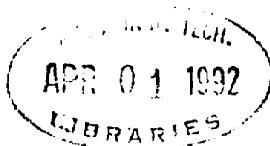
© Massachusetts Institute of Technology 1992

Signature of author _____
Department of Materials Science and Engineering
January 10, 1992

Certified by _____
Andreas Mortensen
Thesis Supervisor

Accepted by _____
Linn W. Hobbs
Professor of Materials Science
Chairman, Departmental Committee
on Graduate Students

ARCHIVES



Infiltration of Deformable Porous Media

by

Jared Lee Sommer

Submitted to the Department of Materials Science and Engineering on January 10, 1992 in partial fulfillment of the Requirements for the Degree of Doctor of Philosophy in Metallurgy.

ABSTRACT

General equations for the isothermal infiltration of deformable porous media by a liquid flowing in slug-flow under a constant pressure differential are solved using the Boltzmann transformation, to derive the progression of infiltration and local porous medium deformation at all times. This analysis is extended to include the effects of solidification of the infiltrating liquid caused by a low initial porous medium temperature, under the assumption that the liquid has a single melting point. For this case, upper and lower bounds on the infiltration kinetics and extent of medium relaxation in the presence of solidified infiltrant are given. Finally, the effects of friction between the porous medium and its container are analyzed.

In order to verify the isothermal model, a high-density polyurethane sponge is infiltrated hydrostatically with ethylene glycol. Liquid infiltration velocity and strain distribution within the sponge are recorded with time using a video camera. The infiltration kinetics and volume fraction distributions during infiltration agree with theory within experimental error.

Non-isothermal infiltration of compressible Saffil™ preforms by pure aluminum is also compared to the theoretical analysis. Friction at preform boundaries is found to control the onset of preform compression and can account for lack of relaxation of the preform when compression occurs. It is also found that this effect is strongly dependent on mechanical and thermal boundary conditions along the preform sides.

Thesis Supervisor: Professor Andreas Mortensen

Title: Associate Professor of Metallurgy

TABLE OF CONTENTS

ABSTRACT.....	2
TABLE OF CONTENTS.....	3
LIST OF ILLUSTRATIONS AND FIGURES.....	6
LIST OF TABLES.....	10
ACKNOWLEDGMENTS.....	11
I - INTRODUCTION.....	13
II - LITERATURE SURVEY.....	15
A - FLUID FLOW THROUGH DEFORMABLE POROUS MEDIA.....	15
B - PREFORM DEFORMATION IN INFILTRATION PROCESSING OF METAL-MATRIX COMPOSITES.....	20
III - THEORY.....	25
A - ISOTHERMAL INFILTRATION.....	25
1 - General problem statement.....	25
2 - General equations.....	27
a. Fluid flow.....	27
b. Conservation of mass.....	28
c. Conservation of force.....	28
3 - Unidirectional infiltration under constant applied pressure.....	29
a. Unidirectional infiltration.....	29
b. The similarity solution and boundary conditions.....	31
c. Special case.....	37
d. Numerical solution of equations.....	39
B - INFLUENCE OF SOLIDIFICATION AND WALL FRICTION.....	41
1 - Effect of metal solidification in adiabatic infiltration.....	41
2 - Effect of external surfaces, case of non-adiabatic infiltration.....	46
IV - EXPERIMENTAL PROCEDURES.....	58
A - INFILTRATION OF COMPRESSIBLE POLYURETHANE SPONGE.....	58

1 - Material systems.....	58
2 - Sponge infiltration apparatus.....	59
3 - Hydrostatic compression tests	61
a. V_f vs hydrostatic pressure	61
b. Viscoelastic behavior tests.....	62
4 - Foam permeability measurements	62
5 - Infiltration experiment data collection	67
B - INFILTRATION OF ALUMINA FIBER PREFORMS BY	
ALUMINUM.....	68
1 - Infiltration experiments	68
2 - Fiber compression tests.....	71
3 - Fiber permeability	72
4 - V_f determination in infiltrated specimens	74
5 - Metallography.....	75
V - RESULTS.....	82
A - INFILTRATION OF POLYURETHANE FOAM.....	82
1 - Hydrostatic pressure vs V_f	82
2 - Viscoelastic behavior of the sponge.....	83
3 - Sponge permeability.....	83
4 - Experimental results for sponge infiltration.....	84
B - INFILTRATION OF ALUMINA FIBER PREFORMS BY	
ALUMINUM.....	85
1 - Infiltration experiments	85
2 - Compressibility of Saffil™ alumina fiber preforms.....	90
3 - Permeability of the fiber preforms.....	92
VI - DISCUSSION.....	111
A - INFILTRATION OF POLYURETHANE FOAM.....	111
1 - Assumptions of the model	111
a. Darcy's Law	111
b. Wetting and permeability.....	112
c. Experimental error in V_f and χ	113
d. Effects of air evacuation and viscoelasticity.....	114
e. Effect of evaporation at the infiltration front.....	114
f. Influence of the fluid on mechanical properties	
of the sponge.....	117
2 - Comparison of theory with experiment.....	117

B - INFILTRATION OF ALUMINA FIBER PREFORMS BY ALUMINUM.....	119
1 - Validation of Darcy's Law	119
2 - Incidence of preform compression.....	120
3 - Kinetics of infiltration.....	124
VI - CONCLUSIONS.....	140
Appendix (3.1) - Program for sponge infiltration.....	142
Appendix (3.2) - Program for alumina fiber infiltration.....	152
Appendix (4.1) - Coring apparatus and coring procedure.....	164
Appendix (4.2) - Monofilament insertion procedure.....	166
Appendix (4.3) - Alternative method for measuring preform permeability	167
Appendix (5.1) - Viscosity of ethylene glycol.....	168
Appendix (5.2) - Estimation of experimental error for sponge experiments	169
Appendix (5.3) - Estimation of experimental error for composite experiments.	173
REFERENCES.....	179
BIOGRAPHICAL NOTE.....	189

LIST OF ILLUSTRATIONS AND FIGURES

Figure (3.1) - Infiltration by a non-wetting fluid.....	50
Figure (3.2) - Infiltration by a wetting fluid.....	51
Figure (3.3) - Schematic description of an elastic deforming porous medium during infiltration.....	52
Figure (3.4) - Coordinate system used in the analysis of the infiltration of a deformable porous medium.....	53
Figure (3.5) - Schematic showing the engulfed region dx_f at the infiltration front changing from V_f^c to V_f^f with a finite solid and liquid velocity.....	54
Figure (3.6) - Schematic illustrating a porous medium under unidirectional hydrostatic pressure infiltration.....	55
Figure (3.7) - Flow chart of algorithm used to solve the differential equations.....	56
Figure (3.8) - Schematic showing the frictional stresses of the mold wall opposing the compressive stresses induced on the fibers by the liquid.	57
Figure (4.1) - Micrographs of the polyurethane foam.....	76
Figure (4.2) - Schematic of the chamber used to infiltrate the sponge with ethylene glycol.....	77
Figure (4.3) - Setup to test permeability of sponge in same conditions as the actual hydrostatic infiltration.....	78
Figure (4.4) - Overview of the apparatus used to test sponge permeability under various strain and saturation conditions.....	79
Figure (4.5) - Illustration of method used to determine the permeability of Saffil™ fibers with water using the falling head method.....	80
Figure (4.6) - Dimensions used in calculating volume of composite slices for volume fraction measurements.	81
Figure (5.1) - Plot of the results for two separate foam hydrostatic pressure tests.....	94
Figure (5.2) - V_f vs. hydrostatic pressure.....	95

Figure (5.3) - Experimental sponge permeability as a function of volume fraction.....	96
Figure (5.4) - Video images of sponge infiltration experiment.....	97
Figure (5.4) - (Continued) - Reproduced video images of sponge infiltration experiment.....	98
Figure (5.5) - Total infiltrated length L^2 as a function of time.....	99
Figure (5.6) - Experimental V_f distribution along infiltrated length of sponge at various times.....	99
Figure (5.7) - Macrostructure of a longitudinal section of sample M (etched).....	100
Figure (5.8) - Macrostructure of a longitudinal section of compressed sample E.....	101
Figure (5.9) - Macrostructure of a longitudinal section of sample K (etched).....	102
Figure (5.10) - Measured V_f distribution along infiltrated length with predicted values of V_f for no relaxation, $\sigma = \frac{2\tau_s}{R_i}$, and full relaxation (sample I).....	103
Figure (5.11) - Measured V_f distribution along infiltrated length with predicted values of V_f for no relaxation, $\sigma = \frac{2\tau_s}{R_i}$, and full relaxation (sample J).....	104
Figure (5.12) - Measured V_f distribution along infiltrated length with predicted values of V_f for no relaxation, $\sigma = \frac{2\tau_s}{R_i}$, and full relaxation (sample K).....	105
Figure (5.13) - Schematic illustration of method of data collection from SiC monofilament when preform compression occurs.....	106
Figure (5.14) - Unidirectional compression curves for fiber preforms of $V_f^0 = 0.180, 0.188, \text{ and } 0.194$ and $T_f = 150^\circ\text{C}$	107

Figure (5.15) - Stress-strain cyclic compression of a fiber preform of $V_f^0 = 0.189$ and $T_f = 150^\circ\text{C}$, increasing the maximum load from 1.38 MPa (200 psi) to 3.45 MPa (500 psi).....	108
Figure (5.16) - Plots of initial and steady-state permeabilities vs. various V_f^0 . Permeability results for two preforms used by Masur (Masur, Mortensen et al. 1989) are also shown in the diagram.....	109
Figure (5.17) - Initial and steady-state hydraulic radii vs. V_f^0 . Hydraulic radii for preforms used in Masur (Masur, Mortensen et al. 1989) are also shown in the diagram.....	110
Figure (6.1) - see Figure (3.4) for definitions	128
Figure (6.2) - Plot of $l(\chi=1) - s(\chi=0)$ vs. time	129
Figure (6.3) - Experimental V_f distribution along infiltrated length of sponge at various times as compared with theoretical predictions.....	130
Figure (6.4) - Theoretical predictions along infiltrated length for	131
Figure (6.5) - Plot of maximum value of dP/dx vs. experimental compression results	132
Figure (6.6) - Pressure, dP/dx , and L^2 as a function of time for sample K.....	133
Figure (6.7) - Theoretical values of ψ^2 vs. ΔP_T at $T_f = 100^\circ\text{C}$ and $V_f^0 = 0.188$, assuming non-isothermal adiabatic infiltration and no wall friction.....	134
Figure (6.8) - Theoretical values of ψ^2 vs. ΔP_T at $T_f = 200^\circ\text{C}$ and $V_f^0 = 0.188$, assuming non-isothermal adiabatic infiltration and no wall friction.....	135
Figure (6.9) - Theoretical values of ψ^2 vs. T_f for $\Delta P_T = 2.07$ MPa and $V_f^0 = 0.188$, assuming non-isothermal adiabatic infiltration and no wall friction.....	136
Figure (6.10) - Micrographs showing compression distances and infiltration lengths of etched samples	137

Figure (6.11) - Comparison of experimental data with theory,
assuming no preform compression..... 138

Figure (6.12) - Comparison of experimental values of ψ with
theory, assuming compression with no relaxation,
according to case (ii) of Section III-B-1..... 139

Figure (A-4.1) - Procedure for coring Saffil™ fibers..... 177

Figure (A-4.2) - Schematic illustrating the method of drilling the
SiC monofilament into the preform core..... 178

LIST OF TABLES

Table 5.1 - Polyurethane foam permeability	84
Table 5.2 - Experimental conditions for the aluminum/alumina fiber composite samples.....	89
Table 5.3 - Compression distances, final infiltration distances, and experimental errors in L_c	90
Table 5.3 - Summary of alumina fiber compression tests.....	92
Table 5.4 - Fiber permeability summary.....	93
Table 6.1 - Comparison of experimental and theoretical infiltration rates.....	127

ACKNOWLEDGMENTS

I would like to express my gratitude to all the people who helped me to learn and grow while I have been at MIT. Foremost on the list is my advisor, Andreas Mortensen, for it was through his help, in nearly every aspect of this work, that this thesis was made possible. I would like to thank him for his patience and his understanding.

I would like to thank Tami Jonas, Nancy Dean, and Veronique Michaud for their friendship. Their smiles and laughter have many times helped me through the silent struggles and made the stay here more enjoyable.

Maria W. Due had always an unending desire to help those around her. She has been a "constant" while I've been here and I will really miss her. I would like to thank Tom Piccone for his willingness to share and help, as well as Nathan Taylor, Robert Calhoun, David Dunand, and Liz Earhart for their sense of humor and helpfulness. Tom Fitzgerald, Pavel Bystricky, Peter Grasty, Qi Zhao, and all my Japanese friends have also provided needed encouragement and friendship. I would also like to thank Henri Kytomaa in Mechanical Engineering for his helpful discussion in getting me started at the beginning of this project.

Others that have helped me by their examples have been Clayton and Christine Christensen. Clayton's trust in me has planted a seed of faith in myself and the opportunity in working with him will be always cherished. I would like to express my gratitude to Brett Sorenson for always supporting me and offering me his hand of friendship. Brett is truly a man without guile and a great friend. I am grateful to Bryant Collard, Craig and Catherine Christensen, and Ray and Brenda Christensen for their friendship.

I couldn't say enough for my "old roomy" Keith Dionne. He was always there to support me and has been an example in showing me the balance of life, even when times were rough. His insight into life and for the many great times that he created will always be remembered. I would also like to thank Steve Rowley, Wendy Milne, and Kathy Dollacker for their friendship and support.

I give my appreciation to my friends at church, for their Christ-like examples in serving others. The Rick Rawlins, Mary Johnstons, Nathan Sheets, and Susan Holbrooks have all set precedents for me to follow.

I will always remember the passion that John F. Elliott had for teaching and his desire to help me understand. I would like to thank also all the machinists and tinkerers that have taught me how to build equipment. Perhaps I will use those acquired skills someday.

I want to express my appreciation to Joe Weeks, for his friendship, patience, and help while I have been in Boston. I am eager to return.

I would like to let my parents know how much I truly love them for their support. The years have been long, but the teachings and principles that they have taught me throughout my life have become important and have buoyed me up in times of trial. I would like to thank my father, who continually encouraged me to go onward, work, and look through the eyes of faith. I love my mother for her thirst to learn and to apply correct principles within her life. Together, they have been a source of inspiration and direction for my life.

I appreciate all of my family members, for the long chats on the phone, the care packages, and encouraging letters. My 5-year-old niece, Amberly, has prayed every night for the past year or two that I may return home quickly. The only thing she knows is that it will be "soon," and so she keeps on praying and having a child-like faith. Derek and Teresa and their whole family has been a never-ending source of encouragement and understanding. I would like to thank Rebecca, my sister, for her continual thoughtfulness and support while I have been here. Peter and Lisa and their family have also contributed much through the family "Christmas projects" and letters. I appreciate Dan and Jonathan, as well as Paul and Marcus, for their sense of humor and friendship. I would also like to thank my brother Joel for being such a true friend. He will always be a friend to me.

Most of all, I would like to thank the Lord for the opportunity to receive knowledge, experience, forgiveness, guidance to principles, and help through trial. I pray that I will use the given talents for His glory.

INFILTRATION OF DEFORMABLE POROUS MEDIA

I- INTRODUCTION

Fluid flow through deformable porous media is an important topic in various engineering fields, ranging from soil mechanics to biomechanics. As fluid flows through a non-rigid porous medium or matrix, viscous drag exerted by the liquid on the solid transfers stress to the porous medium, causing deformation of the latter. This deformation of the solid, in turn, affects the rate of fluid flow through the porous medium.

Although extensive research and modeling have been done on the flow of a liquid through a non-rigid matrix, most analyses to date have focused on steady-state flow conditions in porous media that initially contain fluid within the pores. In this present work, we relax these assumptions and solve the time-dependent problem of the infiltration of an initially dry deformable porous medium by a pure liquid at a constant applied pressure. The effect of phase changes within the liquid upon the infiltration kinetics and deformation behavior of the porous medium are subsequently included in the analysis, a topic which to the best of our knowledge has not been addressed before in the literature. Finally, theoretical predictions are confirmed by experiments on two systems: hydrostatic infiltration of a polyurethane foam with ethylene glycol and

unidirectional infiltration of alumina fiber preforms with pure aluminum.

The motivation for this work is the practical importance of preform deformation during infiltration processing of metal-matrix composites. Previous studies have shown that deformation of the porous reinforcement preform influences infiltration kinetics, as well as the final microstructure and mechanical properties of the material produced. To date, virtually no research has been done in analyzing this problem in the processing of metal-matrix composites, and several erroneous qualitative concepts regarding the deformation of porous media during processing have been put forth in the literature.

The thesis is divided into three principal sections, covering in turn theory, experimental work on foams, and experimental work on metal-matrix composites. In the first of these sections, we state our assumptions, present the basic equations for the infiltration of a liquid into a deformable porous medium, and solve these for unidirectional and for hydrostatic infiltration, in both cases with a constant pressure drop driving the liquid. We also discuss effects of metal solidification and wall friction at the end of this section. In the second of these sections, the mechanical behavior and infiltration rate of polyurethane foams are measured and compared with theory. In the third main section, experiments on infiltration of alumina fiber preforms by aluminum are described and discussed in light of the theoretical analysis. Before these, a brief survey of relevant background is presented.

II - LITERATURE SURVEY

A - FLUID FLOW THROUGH DEFORMABLE POROUS MEDIA

Some of the earliest studies of fluid flow through deformable porous media were concerned with the consolidation of soils containing water or other liquids. When such a porous medium is subjected to external stress, its deformation is controlled by the properties of the individual phases present in the soil, and by the motion of liquid within the porous medium. One central concern of research in this field is the influence exerted by liquid, with its hydrostatic "pore" pressure and its limited flow rate, on the rheology of the porous medium as a whole (Biot 1955; Biot 1957; Hubbert and Rubey 1959; Nur and Byerlee 1971; Garg and Nur 1973; Kenyon 1976; Kenyon 1976; Rice and Cleary 1976; Beavers, Hajji et al. 1981; Greenkorn 1983; Zienkiewicz and Shiomi 1984; Li, Zienkiewicz et al. 1990, pp. 30 - 33) (Bear and Bachmat 1990, pp. 298 - 312). This work has resulted in the definition of an "effective stress", which yields the same strain in a small volume element ΔV of the wet porous medium as an equal stress would on the dry porous medium. Properties entering the prediction of the effective stress include mechanical properties of the dry medium, those of the individual liquid and solid phases, as well as the saturation with liquid (fraction void filled by liquid). Often, linear relationships are assumed between stress and strain for both the solid material comprising the porous solid medium, and the porous medium itself.

This deformation of the porous medium in turn influences the rate of fluid flow within its pores. Work up to 1974 on this topic was

summarized by Scheidegger (Scheidegger 1974), pages 24-31 and 83-91, whose coverage of the topic is more specifically concerned with consolidation and prediction of flow rate through deformable porous media. Lewis and Schrefler (Lewis and Schrefler 1987) have also considered the topic of consolidation of deformable porous media and give an comprehensive review up until 1987.

Recently, the need to describe several important processes in areas as diverse as biomechanics and chemical engineering has brought about several analytical models of the mechanics of porous media containing a liquid. In the field of biomechanics, Kwan (Kwan, Lai et al. 1990) gives an extensive review of various models describing the compression behavior of articular cartilage, a fibrous elastic material composed of approximately 80% water, in which the primary compression behavior of the tissue is controlled by the viscous drag of the liquid. As in consolidation theory, many of the models have utilized the two-phase theory of mixtures to model the fluid flow.

Fisher (Fisher 1982; Fisher 1988) investigated the deformation of eye lens tissue as a function of pressure and the resulting tissue permeability under steady fluid-flow conditions. It was noted in his studies that the permeability of the membranes declined at higher pressures, in spite of the concomitant thinning of the tissues. This type of phenomenon has been noticed in soft gels and other tissue membranes used as ultrafilters, and has been modeled for steady-state flow conditions by several investigators (Scherer 1989; Holmes and Mow 1990). All of these models deal with fluid flow or the compression behavior of deformable porous media that start and remain saturated with liquid.

Beavers (Beavers and Wilson 1975) analyzed steady-state flow of liquid through polyurethane foams and obtained an analytical expression to describe the deformation behavior of a porous medium as a function of pressure drop. He included in the analysis a threshold pressure gradient necessary to initiate infiltration into the sponge, and transformed the deformation equations from a fixed reference frame to that of the displaced sponge. The solution predicted the final sponge length and liquid mass flow rate as a function of a constant pressure drop across the porous medium. These predictions were experimentally verified with one-dimensional liquid flow, at steady state, through a polyurethane foam block. The experimental results matched predictions quite well at lower sponge deformation regimes. However, at high pressure drops the predicted mass flow rate was too high compared to experiment, presumably because of the friction against the wall of the chamber hindering compression. Other problems may be due to the numerical fitting of the sponge parameters in the higher stress regions, or to deviations from the Forchheimer equation, a relationship used in the analysis to describe the fluid flow characteristics in porous media at higher liquid velocities. In later papers (Beavers, Hajii et al. 1981; Beavers, Wittenberg et al. 1981), Beavers widened the scope of the experimental analysis to include various types of sponges, gas, and liquid in order to validate a similar analytical solution used in the earlier study. Again, the results agreed well at lower pressure drops but deviated at higher compression ratios. Although friction was not considered a factor, the cross-sectional area of the sponge decreased at higher compression, causing air or fluid leakage.

Parker (Parker, Mehta et al. 1987), using Biot's theory of consolidation, performed a similar steady-state flow experiment using a glycerine-water mixture through polyurethane sponge in the Darcian flow regime. Analytical solutions were found, using simple functions for the mechanical properties and permeabilities of the porous medium. His experimental results agreed only qualitatively with theory. The discrepancy was attributed to the modeling and analysis, since no reduction of cross-sectional area of the sponge appeared to occur. Barry (Barry and Aldis 1990) used Parker's experimental sponge data to verify a numerical model predicting the flow of liquid through biological tissues at steady state. The model agreed quite well with the data.

Similar foam experiments were carried out and analyzed by Lanir et al. (Lanir, Saub et al. 1990). Rather than measuring the liquid flow rate and final length of the sponge, which tend to be sensitive to localized strains in the sponge, the strain distributions along the length of the sponge were measured and compared to the theoretical predictions. Experimental results tended to agree well with theory as long as the fluid flow was within the Darcy's Law regime. Pressure distribution along the length of the sponge was also predicted.

Numerical procedures were recently used by Xikui Li et al. (Li, Zienkiewicz et al. 1990) to model the flow and interaction of two immiscible fluids through a deformable material, taking into account the saturation level of the wetting fluid. The strains of the solid matrix, pressure distribution, and saturation levels relative to a fixed reference were predicted for a given constant applied pressure on the liquid. This is the only reference found in the literature that treats infiltration of a liquid into a deformable porous medium. Compared to this work, the geometry

assumed is more complex, and gradual imbibation of the displacing liquid is taken into account; however because numerical procedures were used, the results are specific to the case studied, and are less generally applicable than the analysis presented here.

Resin flow in the manufacturing of epoxy resin composites has been modeled recently by various investigators. Dave (Dave, Kardos et al. 1987) and Gutowski (Gutowski, Morigaki et al. 1987) have proposed mathematical models describing the unidirectional consolidation of laminate composites in autoclave processing. Elastic deformation of the fully saturated fiber structure is considered, as well as three-dimensional fluid flow. Dave (Dave 1990), in a later paper, presented general equations describing fluid flow for the cases of consolidation, pultrusion, and infiltration. Although the effect of fluid saturation was included in the overall analysis, deformation of the fiber bed was only considered for the case of consolidation of the fibers. Trevino et al. (Trevino, Rupel et al. 1991) experimentally characterized the permeability, porosity, and compressibility of various types of stacked fiber mats used in resin injection molding of epoxy resin composites. In a subsequent paper (Young, Rupel et al. 1991), the results were used to model numerically the process of resin injection molding into various fiber mats of differing permeabilities and fiber volume fractions. However, deformation of the fiber bed during infiltration was ignored in the analysis.

B - PREFORM DEFORMATION IN INFILTRATION PROCESSING OF METAL-MATRIX COMPOSITES

Other needs to model fluid flow in compressible porous media have arisen in the field of metal-matrix composite processing, where molten metal is frequently injected under high pressures (typically near 10 to 100 MPa) into a preform of the reinforcing material. The preform is typically composed of packed fibers, whiskers, particles, or mixtures thereof. By applying high pressures on the liquid, the effects of poor wettability between the metal and reinforcement can be overcome to produce near net-shape composites with no shrinkage porosity and few reaction products.

It has been noted by many researchers that high pressures during infiltration, as in squeeze casting, can induce large volume fraction gradients throughout the infiltrated length of the final composite. Imai (Imai, Nishida et al. 1987) found that the volume fraction of $K_2O \cdot 6TiO_2$ whisker preforms, originally at 0.27, had increased to 0.56 after squeeze casting with molten aluminum at an applied pressure of 100 MPa: the resulting preform height was one-half of its original height. No reason for the increase of volume fraction was given. An increase in volume fraction was also noted by Nishida (Nishida, Matsubara et al. 1988) in producing silicon nitride whisker reinforced aluminum matrix composites via squeeze casting. The applied pressure was 100 MPa, and the variation of whisker volume fraction was attributed to nonuniform stresses during the forming operations. Rasmussen et al. (Rasmussen, Hansen et al. 1991; Rasmussen, Hansen et al. 1991) also noted that preforms of Saffil™ alumina fibers were compressed to strains between

25% and 30% after infiltration by aluminum alloys in a die-casting apparatus.

Fukunaga (Fukunaga 1988), in a review of squeeze casting of SiC fibers by molten aluminum, stated that significant preform deformation would occur during infiltration in preforms below a critical volume fraction of fiber. It was proposed that this critical volume fraction tended to be more a function of infiltration velocity of the liquid than of the pressure at which the metal was held during solidification. Although the compression behavior was dictated by the compressive strength of the preform, it was believed that the "hydraulic interaction" between the fiber and metal would play only a small role in the compression mechanism.

Kloucek and Singer (Kloucek and Singer 1986) found that infiltrated SiC whisker composites exhibited an inhomogeneous distribution of reinforcement in the aluminum matrix. It was suggested that the poor distribution of the fibers contributed to the high scatter in the tensile strength data. It was also believed that the variations in whisker volume fraction and the cracks present in the whisker preform were caused by high pressure during the infiltration process.

Patent literature has also mentioned compression of fibers during infiltration. In one patent on squeeze casting (Ban, Arai et al. 1985), although the description is somewhat obscure, it is apparent that fibers of low initial bulk density tended to compress to a higher strain during squeeze casting than fibers with higher bulk density, although the resulting volume fraction within the final composites was not noticeably different. No deformation of the fibers was observed during solidification under high pressure.

Andrews (Andrews and Mortensen 1991), utilizing Lorentz forces, infiltrated alumina fiber preforms by subjecting molten metal to a transient magnetic field, whereby a sufficiently large body force was produced to infiltrate the liquid metal into the matrix of the submerged fibers. In the study, numerical procedures were used to predict the infiltration velocity and depth. It was found that the electromagnetic body forces were high enough to cause preform compression, which had to be taken into account to predict infiltration depths in agreement with experiment. A simplified approach was adopted to take preform compression into account in the model: the fibers were assumed to compress to the maximum volume fraction fiber dictated by inertial and body forces when these were at the infiltration front, and retain that volume fraction thereafter for each electromagnetic pulse. Global compression of the preforms was also neglected, and the preforms were assumed to relax completely between electromagnetic pulses. The effect of relaxation of the fibers behind the infiltration front was thus neglected, and relaxation between pulses was most likely incomplete; however, there was good overall agreement between the experimentally measured infiltration depth and that which was predicted by theory.

Clyne (Clyne and Mason 1987) analyzed theoretically the compressive elastic and fracture behavior of fiber preforms by classifying the fiber structure into two categories: "cross-linked" and in-plane fibers. Cross-linked fibers were described as fibers that lie at an angle between the interconnected arrays of successive in-plane fiber layers. Fiber bending moments and fracture stresses in these two structural situations were used to predict the general elastic and fracture behavior of fibrous preforms. The theoretical predictions matched fairly well with theory in

both the initial elastic and fracture regimes. Clyne proceeded then to predict analytically the necessary applied pressure to initiate infiltration of the liquid metal into the preform. He concluded that this pressure should be low enough to prevent substantial damage of Saffil™ alumina fiber preforms. A characteristic relaxation time, describing the elastic recovery of the compressed preform after infiltration, was used in numerical modeling of the time-dependent temperature profiles in squeeze casting processes. Although it was recognized that once infiltration had taken place, the preforms would relax, and that matrix solidification would interfere with this relaxation, no quantitative treatment was given. Clyne also found that preform delamination, i.e., tears in the preform after infiltration, results from high initial fiber temperatures.

Upon investigating the role of matrix solidification and segregation of an alloy during squeeze casting of an aluminum alloy into Saffil™ fiber preforms, Jarry et al. (Jarry, Dubus et al. 1990) observed volume fraction increases of the reinforcement by as much as 100 % within the infiltrated portion of the matrix. The fiber preforms were only compressed in regions downstream of the infiltration path. These regions were shown to be areas where solid metal-matrix, which had formed upon contact of the melt with initially cold fibers, had not been remelted by superheated metal. This work shows that the compressed fiber reinforcement can be held in place by solid metal which has formed as a result of cooling by the fibers.

In summary, although many qualitative observations and explanations have been made regarding the deformation behavior of reinforcement during composite processing, no formal analytical

treatment, and no experimental investigation of the problem have been found in the literature.

III - THEORY

A - ISOTHERMAL INFILTRATION

1 - General problem statement

Consider the infiltration of a porous medium by a liquid injected into the medium under applied pressure. We assume that the liquid and the solid porous medium are at the same constant temperature everywhere and that a negligible amount of heat is generated during the viscous flow of the liquid.

We simplify capillary phenomena at the liquid/air interface by assuming that a sharp front separates a fully infiltrated region, where the porous material is saturated with liquid, from the remaining uninfiltrated portion of the porous medium. Where the liquid is present, we assume that the liquid fills all pores in the solid porous material, with the exception of isolated pores which we assimilate to the solid phase. The liquid saturation is thus everywhere constant and independent of pressure in the liquid. This assumption, called the "slug-flow" assumption by several authors (Mortensen, Masur et al. 1989), ignores the gradual nature of wetting in infiltration (Mortensen and Wong 1990; Mortensen 1991). This is a simplification of the infiltration process which has been found to model overall infiltration kinetics appropriately in several previous studies (Bear 1972; Yang, Zografis et al. 1988; Masur, Mortensen et al. 1989; Mortensen, Masur et al. 1989; Dave 1990; Mortensen and Wong 1990, pp. 303 and 519). We assume that the gas ahead of the front is easily expelled through the porous regions of the

uninfiltrated fibrous preform, offering negligible resistance to flow because of the comparatively low viscosity of the gas. The pressure within the gas that occupies the uninfiltrated portion of the preform is then essentially constant.

Because the solid/air and liquid/solid interfacial energies generally differ, a jump in pressure exists across the infiltration front. This pressure jump, due to capillary forces, is assumed to be constant, and is defined as ΔP_γ . If $\Delta P_\gamma < 0$, the liquid "wets" the fibers, and will be drawn into the fiber matrix in order to minimize the surface free energy of the system. On the other hand, if $\Delta P_\gamma > 0$, flow of the liquid is hampered by capillary forces, and pressure must be applied to drive the liquid.

We assume that the liquid and solid materials themselves are incompressible. The saturated porous material, therefore, does not respond to hydrostatic stress, since we have assumed that its saturation is constant. The porous material will, on the other hand, respond to applied hydrostatic pressure if the volume of its pores can change, which can be effected by flow of liquid when it is saturated or by compression or flow of the gas when it is uninfiltrated.

We make no particular assumptions concerning the response of the porous solid material. In particular, it will often be irreversible, as deformation may break or deform individual elements, such as fibers, that constitute the porous material.

2 - General equations

a. Fluid flow

We assume that the pores are very small in comparison to the scale of infiltration, so we can assimilate the porous medium to a continuum. We can then take a small volume element ΔV containing several pores within an infiltrated portion of the composite. The volume fraction of the solid phase, including isolated pores which do not get filled by liquid, is V_f .

We assume that fluid flow within the volume element follows Darcy's Law, taking into account the average movement of the solid phase:

$$\mathbf{v}_l - \mathbf{v}_s = - \frac{\mathbf{K}}{(1-V_f) \mu} (\nabla P - \rho_l \mathbf{g}) \quad (3.1)$$

where:

- \mathbf{v}_l = average local velocity of the liquid within the pores of ΔV
- \mathbf{v}_s = average local velocity of the solid within ΔV , measured in the same reference frame as \mathbf{v}_l
- \mathbf{K} = permeability tensor of the porous medium in ΔV
- μ = liquid viscosity
- P = pressure in the liquid
- ρ_l = density of the liquid
- \mathbf{g} = acceleration due to body forces including gravity

We assume that μ is constant, whereas K is dependent upon V_f , and, in some instances, on the previous strain history of the porous material.

b. Conservation of mass

We assume that the fluid and the material making the porous medium are incompressible. A balance of the masses of solid and liquid entering, exiting and accumulating within ΔV then dictates the mass conservation equations:

$$\text{solid} \quad \frac{\partial V_f}{\partial t} + \nabla \cdot (V_f \mathbf{v}_s) = 0 \quad (3.2)$$

$$\text{liquid} \quad - \frac{\partial V_f}{\partial t} + \nabla \cdot ((1-V_f) \mathbf{v}_l) = 0 \quad (3.3)$$

c. Conservation of force

We neglect inertial effects in both solid and liquid. Stress equilibrium of ΔV then dictates:

$$\frac{\partial P}{\partial x_i} + \sum_{j=1}^3 \frac{\partial \sigma_{ij}}{\partial x_j} - \rho_l g_i = 0 \quad (3.4)$$

where P is the pressure in the liquid, g_i is the average body force in ΔV and σ_{ij} are components of the (symmetric) effective stress tensor acting in the solid, counted as positive in compression and averaged over a surface area comprising both solid and liquid, and ρ_l is the density of the liquid. The effective stress, which equals the actual average stress in all material within ΔV minus the fluid pressure P , determines the macroscopic deformation of the porous material in ΔV , provided that the volume fraction of the liquid phase is not vanishingly small (Hubbert and Rubey 1959; Nur and Byerlee 1971; Garg and Nur 1973; Beavers, Hajji et al. 1981; Li, Zienkiewicz et al. 1990).

3 - Unidirectional infiltration under constant applied pressure

a. Unidirectional infiltration

We now consider the case where infiltration takes place along one direction only, defined as the x axis, and where strain in the porous material is only along that direction. We assume that the porous medium is homogeneous, and isotropic in a plane perpendicular to the infiltration direction. The liquid penetrates the porous material at one of its ends, infiltrating it toward the other end under a constant pressure P_o , applied on the liquid at the entrance of the porous medium. We assume that the porous medium is fixed at the other end. The gas pressure in the uninfiltred porous material is assumed to be constant and is defined as P_g , and the pressure difference driving the flow is $\Delta P_T = P_o - P_g$.

The basic physics of the situation can be understood by simple examination of the problem. Assume that the stress-strain curve

measured on the porous medium by unidirectional compression takes the form depicted at the top of Figure 3.1a, for loading to ΔP_T and unloading to zero stress. Assume also that there are no strains in the y or z directions. This curve could be measured on a dry sample of the porous material if its behavior is unaffected by chemical interaction in contact with the liquid phase.

It is clear that if inertial effects can be ignored, the porous solid material ahead of the infiltration front must be stressed under the full effective compressive stress $\sigma_{xx} = \Delta P_T$, correspondingly straining the porous preform as indicated in the figure. As the infiltration front passes, it engulfs a slice dx of the porous material, which sees its effective stress altered by the capillary pressure ΔP_γ . The porous material immediately behind the front will therefore relax somewhat (following the unloading stress-strain curve) if $\Delta P_\gamma > 0$, i.e., if the liquid does not wet the porous material. Its strain will therefore decrease, to a value given by the unloading portion of the stress-strain curve at $\sigma_{xx} = \Delta P_T - \Delta P_\gamma$. Conversely, if $\Delta P_\gamma < 0$, corresponding to wetting by the liquid, the porous medium will contract somewhat, climbing further up the loading stress-strain curve to $\sigma_{xx} = \Delta P_T - \Delta P_\gamma$, as depicted in Figure 3.2a.

From behind the infiltration front to the preform entrance, the liquid pressure P increases from $\Delta P_\gamma + P_g$ to P_o , and the effective stress σ_{xx} acting on the porous medium correspondingly decreases to zero. The compressive strain on the porous medium therefore decreases toward the entrance, following the stress strain curve for unloading from $\Delta P_T - \Delta P_\gamma$. To see this in a more physical way, picture the porous medium as a series of small solid objects connected by infinitely thin springs, as in Figure 3.3. As the liquid flows past these, it exerts a viscous drag force on the objects,

which pushes these toward the infiltration front. For this reason, the stress on the springs (the effective stress σ_{xx} on the porous solid medium for this example) increases as one moves from the entrance to the infiltration front, from a value near zero at the entrance to $\Delta P_T - \Delta P_\gamma$ right before the infiltration front. At the infiltration front, capillary forces additionally act on the last row of objects being engulfed, further compressing the springs upstream if wetting is poor.

The pressure gradient within the infiltrated portion of the porous material depends on the local volume fraction of the solid phase, V_f , because the permeability K depends on V_f . Therefore, the infiltration kinetics and the shape of the porous material during infiltration are linked, and must be solved together.

b. The similarity solution and boundary conditions

When a constant pressure P_0 is applied on the liquid, it will travel toward the porous medium, contact, and compress the latter to a volume fraction $V_f = V_f^c$, corresponding to $\sigma_{xx} = \Delta P_T$ on the stress-volume fraction curve (Figures 3.1 and 3.2). The position to which the preform entrance is initially compressed is defined as $x = 0$, and the time of initial contact as $t = 0$. The x -axis is fixed in relation to the uninfiltated end of the preform. In what follows, we drop the suffix x from vectorial or tensorial components.

Governing Equations (3.1) to (3.4) can be simplified considerably in the case of present interest if we neglect body forces g . Equations (3.1) to (3.4) become:

$$\text{Darcy's Law} \quad v_l - v_s = \frac{-K}{(1 - V_f) \mu} \frac{\partial P}{\partial x} \quad (3.5)$$

$$\text{Solid} \quad \frac{\partial V_f}{\partial t} + \frac{\partial(V_f v_s)}{\partial x} = 0 \quad (3.6)$$

$$\text{Liquid} \quad -\frac{\partial V_f}{\partial t} + \frac{\partial((1 - V_f) v_l)}{\partial x} = 0 \quad (3.7)$$

$$\text{Stress equilibrium} \quad \frac{\partial P}{\partial x} = -\frac{\partial \sigma}{\partial x} \quad (3.8)$$

We use the Boltzmann transformation to transform these partial differential equations into ordinary differential equations by combining x and t into a single variable, which describes the present problem in its entirety.

We define χ as:

$$\chi = \frac{(x - x_e)}{\psi \sqrt{t}} \quad (3.9)$$

where x_e is the position of the fiber preform entrance at time t . Because the preform relaxes, $x_e < 0$. The scalar ψ is chosen such that the position of the infiltration front corresponds to $\chi = 1$. Therefore,

$$L = \psi \sqrt{t} \quad (3.10)$$

where L is the total length of the infiltrated portion of the preform, as shown in Figure 3.4.

Taking the partial derivatives of χ with respect to x and t :

$$\frac{\partial \chi}{\partial x} = \frac{1}{\psi \sqrt{t}} \quad (3.11)$$

$$\frac{\partial \chi}{\partial t} = -\frac{(x - x_e)}{2 \psi t^{3/2}} - \frac{v_s(\chi=0)}{\psi \sqrt{t}} = -\frac{\chi}{2t} - \frac{v_s(\chi=0)}{\psi \sqrt{t}}. \quad (3.12)$$

Expansion of Darcy's law and insertion of the stress equilibrium Equation (3.8) yields:

$$v_l - v_s = \frac{K}{(1-V_f) \mu} V_f'(\chi) \frac{1}{\psi \sqrt{t}} \sigma'(V_f) \quad (3.13)$$

where

$$V_f'(\chi) = \frac{\partial V_f}{\partial \chi} \quad \text{and} \quad \sigma'(V_f) = \frac{\partial \sigma}{\partial V_f}.$$

We define l and s as given by:

$$v_l = \frac{\psi l(\chi)}{\sqrt{t}} \quad (3.14)$$

$$v_s = \frac{\psi s(\chi)}{\sqrt{t}}, \quad (3.15)$$

where l and s are functions of χ only. Equation (3.13) now becomes:

$$\boxed{V_f'(\chi) = \frac{(1-s)(1-V_f) \mu \psi^2}{K \sigma'(V_f)}} \quad (3.16)$$

Mass conservation Equations (3.6) and (3.7) become:

$$\boxed{s' = \frac{-V_f'}{V_f} \left(-\frac{\chi}{2} - s(0) + s \right)}, \quad (3.17)$$

and

$$\boxed{l' = \frac{-V_f'}{(1-V_f)} \left(\frac{\chi}{2} + s(0) - l \right)}. \quad (3.18)$$

As discussed earlier, each end of the infiltrated portion of the composite has its volume fraction of fibers fixed by the unloading stress-strain curve for initial compression to ΔP_T . Two boundary conditions follow:

$$\boxed{V_f = V_f^f \text{ at } \chi = 1^-} \quad (3.19)$$

$$\boxed{V_f = V_f^r \text{ at } \chi = 0} \quad (3.20)$$

where V_f^f corresponds to $\Delta P_T - \Delta P_\gamma$ on the unloading curve after loading to ΔP_T for a non-wetting liquid, and on the stress-strain curve for further loading from $\Delta P_T - \Delta P_\gamma$ for a wetting liquid. V_f^r corresponds to the fully relaxed state of the fibers after compression to ΔP_T for a non-wetting liquid, and $\Delta P_T - \Delta P_\gamma$ for a wetting liquid.

Consider a slice of thickness dx_f in the dry porous material immediately ahead of the infiltration front. In both the wetting and non-wetting cases, dx_f ahead of the infiltration front (i.e., corresponding to $\chi \geq 1^+$) is compressed to $V_f = V_f^c$, the volume fraction solid that corresponds

to compression of the porous material under $\sigma = \Delta P_T$ (Figures 3.1 and 3.2). As the infiltration front engulfs dx_f and V_f changes to V_f^f , the width of porous material changes from dx_f to $dx_f + dx_x$, as shown in Figure 3.5. As the porous medium expands or shrinks, its solid phase acquires a finite velocity $v_s (\chi = 1^-)$ in the reference frame we use here. If $\Delta P_\gamma > 0$, $dx_x > 0$ and $v_s (\chi = 1^-) < 0$. A mass balance on the solid dictates:

$$dx_f \cdot V_f^c = (dx_f + dx_x) \cdot V_f^f . \quad (3.21)$$

Differentiating with respect to time and rearranging yields:

$$v_{s(\chi=1^-)} = - \frac{dx_x}{dt} = - \frac{dx_f}{dt} \cdot \frac{V_f^c - V_f^f}{V_f^f} . \quad (3.22)$$

The velocity of the liquid, $v_l (\chi=1^-)$, within the porous structure immediately behind the infiltration front is similarly obtained from a simple mass balance:

$$v_l (\chi=1^-) = \frac{dx_f}{dt} \cdot \frac{(1 - V_f^c)}{(1 - V_f^f)} . \quad (3.23)$$

Knowing that $x_f = L + x_e$, inserting Equations (3.14) and (3.15) into Equations (3.22) and (3.23) yields:

$$s(\chi=1^-) = \left(\frac{1}{2} + s(0) \right) \cdot \frac{V_f^c - V_f^f}{V_f^f} \quad (3.24)$$

and

$$l(\chi=1^-) = \left(\frac{1}{2} + s(0) \right) \cdot \frac{(1 - V_f^c)}{(1 - V_f^f)} \quad (3.25)$$

Equations (3.24) and (3.25), in addition to (3.19) and (3.20), are boundary conditions that must be met in solving Equations (3.16) to (3.18), the solutions of which will be the parameter ψ and the functions $V_f(\chi)$, $l(\chi)$, and $s(\chi)$.

A simpler limiting case is obtained if there is no capillary pressure drop across the infiltration front, i.e., if $\Delta P_\gamma = 0$. Then, $V_f(\chi=1^+) = V_f(\chi=1^-)$ and Equation (3.25) simplifies to:

$$l(1) - s(0) = \frac{1}{2}, \quad (3.26)$$

while Equation (3.24) becomes:

$$s(1) = 0, \quad (3.27)$$

stating that, at the infiltration front, no movement of the solid initially takes place. When $\Delta P_\gamma = 0$, Equation (3.26) can also be obtained by taking the time-derivative of Equation (3.10), knowing that $v_l(\chi = 1^-)$ is the velocity of the infiltration front.

c. Special case: unidirectional infiltration in hydrostatic pressure conditions

We assume in this case that the liquid essentially infiltrates the porous medium along one direction but replace the assumption that there is no lateral strain of the porous medium by the assumption that the side-walls of the medium are subjected to a constant hydrostatic pressure equal to P_0 . This hydrostatic pressure can be exerted by the liquid infiltrant via an impermeable membrane covering the sides of the porous medium (Figure 3.6). In this configuration, the porous medium will experience some lateral strain, resulting in finite solid velocities in the y and z directions.

To treat this case, we make the simplifying assumption that the porous material is isotropic, and that it is slender enough for flow to remain predominantly in the x direction and for planes initially perpendicular to that direction not to bend appreciably. With these assumptions,

$$\frac{\partial V_f}{\partial y} = \frac{\partial V_f}{\partial z} \approx 0 \quad (3.28)$$

The velocity gradient terms of solid phase can be written as strain-rate terms in the following manner:

$$\frac{\partial v_{sj}}{\partial j} = \frac{\partial^2 u_{sj}}{\partial j \partial t} = \dot{\epsilon}_j \quad (3.29)$$

where u_{sj} is the average displacement of the solid in the j direction and $\dot{\epsilon}_j$ is the average strain rate of the solid in the j direction.

In the present configuration, effective stress components σ_{xx} , σ_{yy} , and σ_{zz} are equal. Since the porous medium is isotropic, we therefore have $e_{xx} = e_{yy} = e_{zz}$. Equation (3.2) then becomes:

$$\frac{\partial V_f}{\partial t} + 3V_f \frac{\partial v_{sx}}{\partial x} + v_{sx} \frac{\partial V_f}{\partial x} = 0 \quad (3.30)$$

Insertion of Equation (3.28) into Equation (3.3) yields:

$$-\frac{\partial V_f}{\partial t} - v_{1x} \frac{\partial V_f}{\partial x} + (1 - V_f) \left(\frac{\partial v_{1x}}{\partial x} + \frac{\partial v_{1y}}{\partial y} + \frac{\partial v_{1z}}{\partial z} \right) = 0. \quad (3.31)$$

Because of the geometry and assumptions of the problem, $\frac{\partial v_{1y}}{\partial y}$ and $\frac{\partial v_{1z}}{\partial z}$ are equal (due to symmetry), and zero both along the central axis of the porous medium and at the wall of the impermeable membrane. If we assume that v_{1x} is not a function of either y nor z for the slender porous medium, then according to Equation (3.31), $\frac{\partial v_{1y}}{\partial y}$ and $\frac{\partial v_{1z}}{\partial z}$ are also constant, and hence zero, at fixed x and t . Then, Equation (3.31) becomes identical to Equation (3.7).

Equation (3.30) replaces Equation (3.6). Therefore, Equation (3.17) becomes:

$$\boxed{s' = \frac{-V_f}{3V_f} \left(-\frac{\chi}{2} - s(0) + s \right)}. \quad (3.32)$$

The solution of this case is otherwise similar to that of unidirectional infiltration.

d. Numerical solution of equations

Equations (3.16), (3.17), and (3.18) are nonlinear first-order equations, which were solved using numerical methods. The functions V_f , l , and s were all simultaneously integrated across χ by assuming initial values for ψ^2 , $l(\chi=0)$, and $s(\chi=0)$. $V_f(\chi=0)$ is the volume fraction of the sponge in its totally relaxed state, obtained from unidirectional or hydrostatic pressure experiments on the porous medium.

The mid-point Runge-Kutta scheme was used for integration (Press, Flannery et al. 1989, pp. 271, 551, 583). The method consisted of taking the values and initial derivatives at the beginning of an interval to find the values and derivatives at a point halfway across the next interval, N , from which the values and derivatives at the beginning of the next interval, $2N$, were found. After integrating from $\chi=0$ to $\chi=1$, the final values and functions involving V_f , l , and s were compared with the boundary conditions (3.19), (3.24), and (3.25), for the unidirectional infiltration case, and with (3.19), (3.24), and (3.31) for infiltration under hydrostatic conditions (described in the preceding subsection).

A multi-dimensional Newton-Raphson method was used for adjusting the initial guesses of ψ^2 , $l(\chi=0)$, and $s(\chi=0)$ for convergence. This consisted of transforming the end boundary conditions into functions, f_i , that were to be zeroed, or:

$$f_i(\psi^2, l(\chi=0), s(\chi=0)) = 0. \quad (3.33)$$

By using the Taylor series expansion for each function in the neighborhood of the vector of variables, \mathbf{X} , yields:

$$f_i(\mathbf{X} + \delta\mathbf{X}) = f_i(\mathbf{X}) + \sum_{j=1}^3 \frac{\partial f_i}{\partial x_j} \delta x_j + \text{higher order terms} \quad (3.34)$$

A set of linear equations is obtained by neglecting the higher order terms of Equation (3.34), or:

$$\sum_{j=1}^3 \frac{\partial f_i}{\partial x_j} \delta x_j = -f_i(\mathbf{X}) \quad (3.35)$$

The matrix in Equation (3.35) was solved by using Lower-Upper Decomposition (Press, Flannery et al. 1989, p.31), the solution of which gives the adjustments for x_1 , x_2 , and x_3 to bring each function f_i closer to zero. The old variable values were adjusted by adding to them the errors obtained from the solution of Equation (3.35) to find the new values, i.e:

$$x_i^{\text{new}} = x_i^{\text{old}} + \delta x_j \quad (3.36)$$

Iteration was continued until δx_j was less than a specified limit for all j . In order to insure that the error values were not so large as to cause instability while integrating, the errors were multiplied by a constant less than one before addition to the old value of x_i .

The flow chart for the program is shown in Figure 3.7 and the program is presented in detail in Appendix (3.1) for sponge infiltration. To check for internal consistency within the program, the actual viscous pressure drop was compared with the summation of the drops in

pressure over various increments of $\Delta\chi$, as shown in the following equation:

$$\Delta P_{\mu} = \sum_{\chi=0}^1 \frac{(1-s)\mu\psi^2(1-V_f)}{-K} \Delta\chi \quad (3.37)$$

The values all were taken at the mid-point of the increment $\Delta\chi$ (calculated during the Runge-Kutta integration) to obtain the average for that interval.

B - INFLUENCE OF SOLIDIFICATION AND WALL FRICTION.

1 - Effect of metal solidification in adiabatic infiltration.

We now relax the assumption made in Part A that no exchange of heat takes place between the porous medium and the liquid. We assume that the liquid and the reinforcement are initially at constant but different temperatures, T_0 and T_f , respectively. We also assume that the liquid solidifies with no solute segregation and at a single temperature, T_m .

If T_f is lower than T_m , solidification of the infiltrating liquid will occur during infiltration (Fukunaga and Goda 1984; Fukunaga and Goda 1985; Fukunaga 1988; Mortensen, Masur et al. 1989). As shown in Reference (Mortensen, Masur et al. 1989), assuming liquid/solid interfacial equilibrium for the liquid, a fraction of the infiltrant at the infiltration front tip will solidify on the porous solid, such that the latent heat released by solidification warms the solid phase to T_m . In this

subsection, we modify the theory presented in Section III-A-3 to take into account the effect of such solidification of the liquid during infiltration of a deformable porous medium. We retain for now the assumption made in Part III-A that there is no friction or other effects at the wall restricting deformation of the porous medium. For consistency with previous work on infiltration for the production of metal-matrix composites, we assume henceforward that the liquid is a metal, and that the solid phase is a fiber preform. Results are generally applicable, however, to any porous medium and infiltrant so long as appropriate relations are used to calculate the permeability of the porous medium.

We assume in this subsection that the unidirectional infiltration process is adiabatic, meaning that no heat is exchanged between the fiber preform or the composite and their surroundings. As before, the preform ahead of the infiltration front is compressed under a pressure of ΔP_T . Right behind the infiltration front, where the metal first contacts the fibers, capillary forces will cause an abrupt change in the effective stress, in turn causing expansion or contraction of the preform, as in isothermal infiltration.

Immediately behind the infiltration front, heat is exchanged between fibers and metal, resulting in the solidification of a volume V_s of solid metal per unit composite volume. This results in the formation of a region within the infiltrated composite, called region 1 in Reference (Mortensen, Masur et al. 1989), where liquid and solid metal coexist. This region extends from the infiltration front upstream of the flowing metal to a remelting front, where superheated metal flowing in at the gate remelts the solid metal (see Figure 5 of Reference (Mortensen, Masur et al. 1989)).

Assuming for simplicity that no heat is conducted ahead of the infiltration front into the preform, V_s is calculated from Equation (58) of Reference (Mortensen, Masur et al. 1989):

$$V_s = \frac{\rho_f c_f (T_m - T_f) \cdot V_f}{\rho_m \Delta H_f} \quad (3.38)$$

where ΔH_f is the latent heat of fusion, c_f is the intrinsic heat capacity of the solid phase, and ρ_f and ρ_m are the densities of the solid and metal, respectively. Because there is no migration of the solidified metal with respect to the fibers, this relation between V_s and V_f remains valid everywhere within region 1 (even though V_f varies with position).

In the case of infiltration of fiber preforms by a pure metal, it was shown that the solidification configuration is approximately that of a sheath of solid metal covering the fibers. The coated fibers thus have an apparent radius, r_{sf} , given by:

$$r_{sf} = r_f \sqrt{\frac{V_{sf}}{V_f}} = r_f \sqrt{1 + \frac{\rho_f c_f (T_m - T_f)}{\rho_m \Delta H_f}} \quad (3.39)$$

where $V_{sf} = V_f + V_s$ is the total volume fraction of solid phase present. The new r_{sf} and V_{sf} replace the previous r_f and V_f in calculations of the permeability K , right behind the infiltration front and for all $\chi > \chi_s$, where incoming metal at the gate remelts solidified metal formed at the infiltration front. For $0 < \chi < \chi_s$, the permeability is calculated using the nominal fiber radius r_f and fiber volume fraction V_f .

Matrix solidification cannot prevent the applied pressure from compressing the preform ahead of the infiltration front. If we assume that capillary forces modify the effective stress of the preform before

matrix solidification occurs at the infiltration front, Equation (3.19) remains valid at the infiltration front. The apparent stress-strain curve of the preform containing solid metal must be known for solution of the problem to be possible. If the mechanical response of the preform is time-dependent in the presence of the solid metal, the Boltzmann transformation cannot be used to model infiltration.

There are, therefore, two extremes of behavior which provide bounds for the kinetics of infiltration because further behind the infiltration front, solid metal will stiffen the compressed preform, resulting in a lower degree of preform relaxation than for isothermal infiltration. These two bounds describe the greatest and the least possible extents of preform relaxation and correspond to the two following cases: case (i), where the solid metal does not influence the mechanical response of the preform, and case (ii) where the solid metal confers enough rigidity to the preform to completely prevent its relaxation. In both of these cases, the similarity solution holds. We consider these in turn, making for additional simplicity the assumption that there is no metal superheat, i.e., that $T_0 = T_m$. With no superheat, $\chi_s = 0$ and the temperature is uniform within the composite, equal to T_m .

In *case (i)*, governing equations for preform deformation and fluid flow within the composite are essentially identical to those of isothermal infiltration, save for changes in a few of the equations due to the increased apparent fiber radius behind the infiltration front. Darcy's law, Equation (3.5), is changed to become:

$$v_l - v_s = \frac{-K}{(1 - V_f - V_s) \mu} \frac{\partial P}{\partial x} \quad (3.40)$$

Eqs. (3.6) and (3.8) are unchanged, while Eq. (3.7) becomes:

$$\frac{\partial(1-V_f - V_s)}{\partial t} + \frac{\partial((1-V_f - V_s) v_l)}{\partial x} = 0 \quad (3.41)$$

These equations become, after transformation of x and t to χ :

$$\boxed{V_f'(\chi) = \frac{(1-s)(1-V_f - V_s)\mu\psi^2}{K\sigma'(V_f)}} \quad (3.42)$$

and

$$\boxed{l' = \frac{-V_f' - V_s'}{(1-V_f - V_s)} \left(\frac{\chi}{2} + s(0) - 1 \right)} \quad (3.43)$$

Equation (3.17) and boundary condition Equations (3.19), (3.20) and (3.24) remain unchanged, while Equation (3.25) becomes:

$$l(\chi=1^-) = \left(\frac{1}{2} + s(0) \right) \cdot \frac{(1 - V_f^c)}{(1 - V_f^f - V_s)} \quad (3.44)$$

In *case (ii)*, the fiber volume fraction is uniform, equal to V_f^f throughout the composite. s and l are then constant and given by Eqs. (3.24) and (3.44).

When the preforms are incompressible, $\sigma'(V_f)$ is infinite and V_f is everywhere constant (Eq. (3.16)), so that $s(\chi) = 0$ and $l(\chi) = \frac{1}{2} \cdot \frac{(1 - V_f^o)}{(1 - V_f^o - V_s)}$

for all χ (Eqs. (3.17), (3.43), (3.24), and (3.44)). Governing and boundary equations for case (ii) then reduce to equations of Reference (Mortensen, Masur et al. 1989) for adiabatic infiltration of incompressible preforms with no superheat.

2 - Effect of external surfaces, case of non-adiabatic infiltration.

We now relax the assumption that the preforms can move freely within their mold during infiltration. This is because, in actual infiltration experiments, there is very often a mold wall along the preforms. A necessary condition for preform compression to occur then appears, namely, that frictional forces between the fibers and contacting surfaces such as die walls be overcome.

When the mold initial temperature is lower than the metal melting point, solidification of the metal takes place during infiltration along the mold wall (Masur, Mortensen et al. 1989; Mortensen, Masur et al. 1989). This, too, may influence preform compression. When initial stages of infiltration take place under low applied pressure, solidified metal may "anchor" the preform to the die wall by increasing the apparent die wall friction and conferring strength to the infiltrated portions of the composite. Once preform compression has taken place, solidification at the mold wall may also prevent relaxation of the preform.

We consider a simplified geometry in which the metal infiltrates a fibrous preform contained within a mold of cylindrical geometry with an inner radius R_i and initial temperature T_f . We assume for now that the combined effects of friction and matrix solidification along the mold wall

result in a critical shear stress, τ_s , that must be overcome for the preform to slide along the mold wall. τ_s is clearly very system-dependent, and may vary with time and position as solidification, or chemical reactions between composite and mold wall, take place.

If we assume that the driving pressure, ΔP_T , increases with time from $\Delta P_T = 0$, preform compression will initially not occur because the applied pressure is low. If we consider a cross-sectional slice dx in the infiltrated portion of the preform before preform compression has taken place, we can predict in simple terms the moment at which preform compression takes place.

The liquid pressure drop during infiltration across dx is given by Darcy's law, Equation (3.1). If at time $t > 0$ preform deformation has not yet occurred, the mold wall frictional stresses are opposing the compressive stresses induced on the preforms by viscous friction of the liquid, as shown in Figure 3.8. A simple force balance between the interfacial shear force and pressure drop across dx then yields the following equation:

$$-\pi R_i^2 dP = \tau_f 2\pi R_i dx \quad (3.45)$$

where τ_f is the effective frictional shear stress between the composite and the die wall resisting preform compression. This yields, after rearrangement:

$$\tau_f = -\frac{R_i}{2} \frac{dP}{dx} \quad (3.46)$$

In summary, if τ_f equals or exceeds the shear strength of the interface between the composite and the mold wall, τ_s , then the preform will compress. Before compression occurs, the analysis of Reference (Mortensen, Masur et al. 1989) is valid with $V_f = V_f^0$. When there is superheat in the metal, the pressure gradient is constant within regions 1 and 3 of the infiltrated composite, being much greater in the former than in the latter. It is within region 1, therefore, that preform compression will initiate, possibly leading to tearing at the interface between regions 1 and 3 when the critical pressure gradient is attained in region 1. Because most of the pressure drop across the infiltrated composite, ΔP_μ , takes place within region 1, we can estimate the liquid pressure gradient within that region as being equal to

$$\frac{dP}{dx} \approx \frac{-\Delta P_\mu}{(1-\chi_s) L} \quad (3.47)$$

If we assume that τ_s is constant along the infiltrated composite, for compression of the preform to occur, at one time during infiltration the ΔP_T must be high enough to deform the dry preform and the pressure gradient within the infiltrated portion must be great enough to overcome the frictional stress, according to:

$$\frac{-R_i \Delta P_\mu}{2(1-\chi_s) L} > \tau_s \quad (3.48)$$

The effective mold/preform interfacial shear stress τ_s which must be overcome to cause deformation of the preform will depend on the materials and the boundary conditions at the mold/composite interface.

In particular, when substantial solidification or chemical interaction with the mold take place along the mold wall, τ_s will increase.

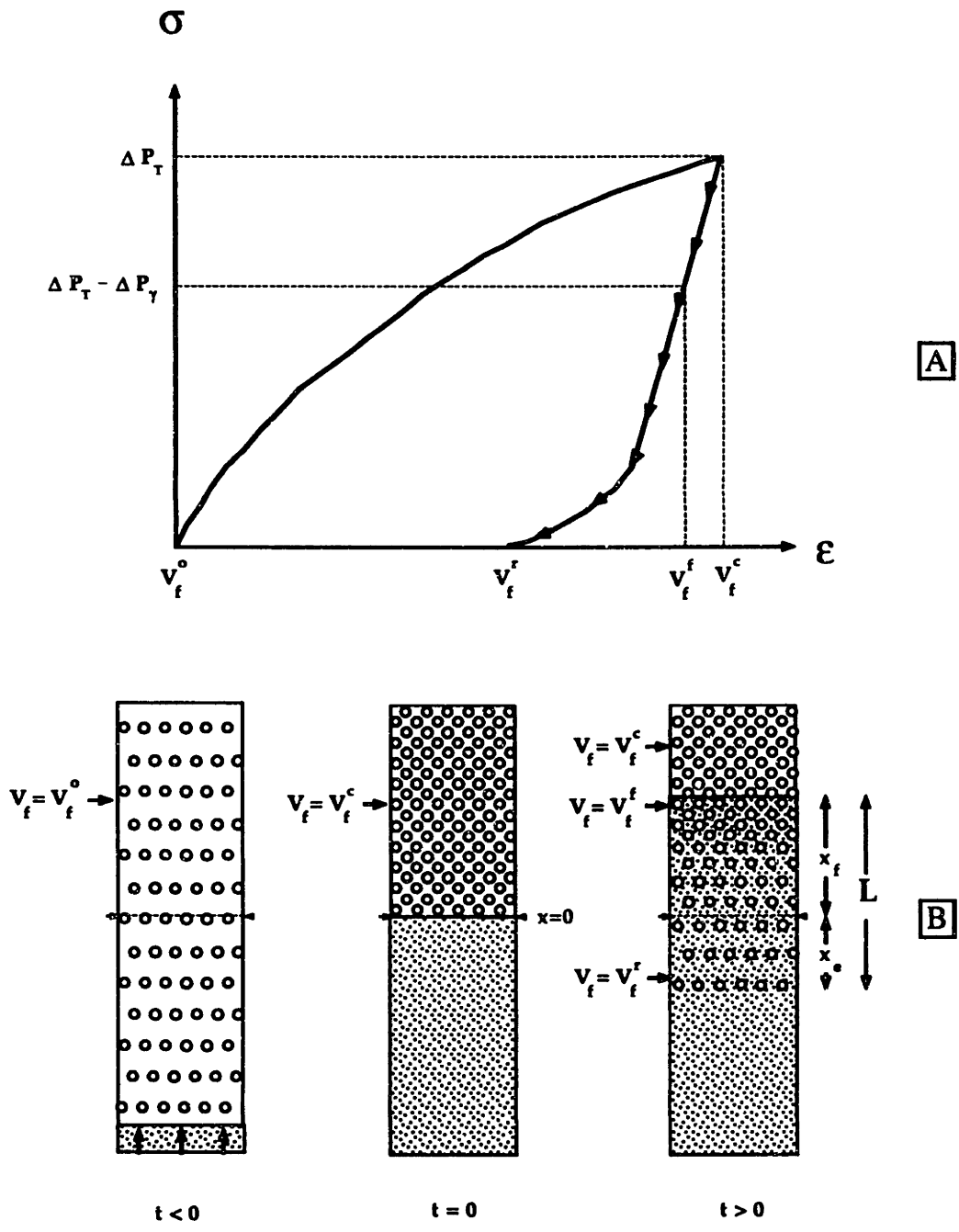


Figure (3.1) -
 (a) Schematic illustration showing the uniaxial compression behavior of a dry porous solid.
 (b) The same solid at various times during infiltration by a *non-wetting* liquid under a constant pressure drop ΔP_T .

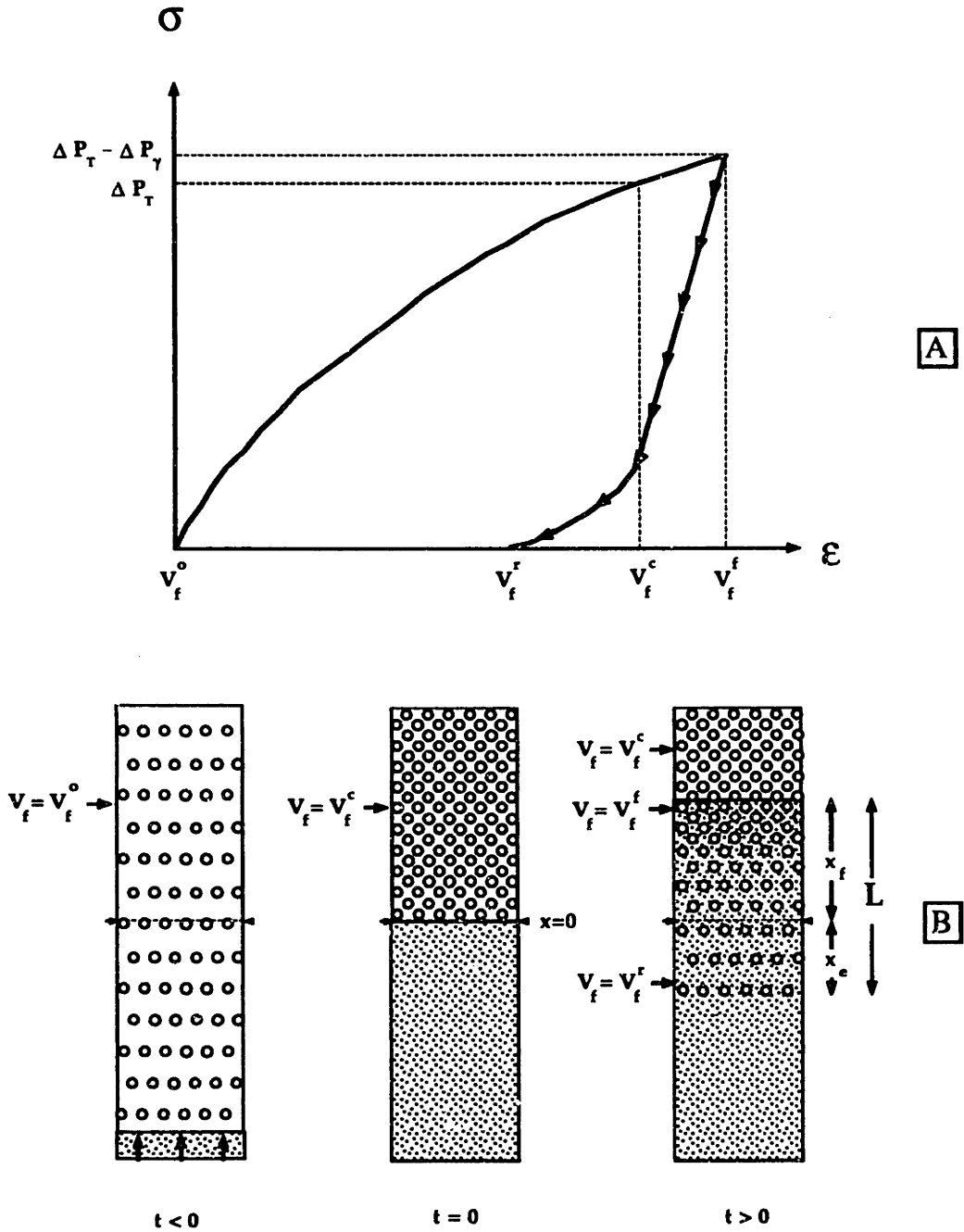


Figure (3.2) -
 (a) Schematic illustration showing the uniaxial compression behavior of a dry porous solid.
 (b) The same solid at various times during infiltration by a *wetting* liquid under a constant pressure drop ΔP_T .

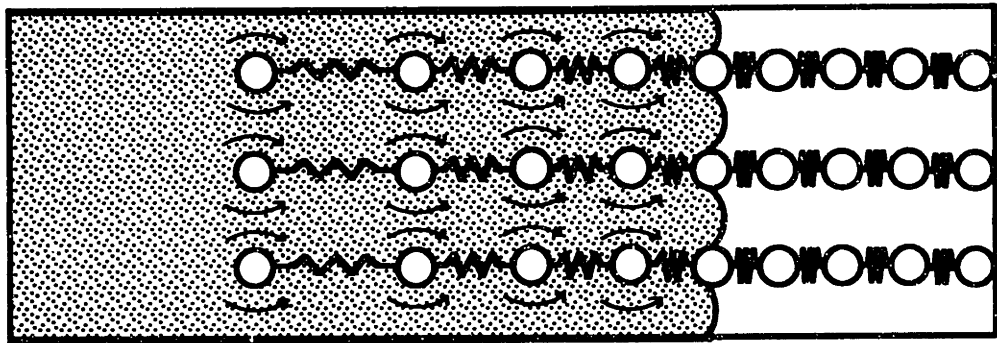


Figure (3.3) - Schematic description of an elastic deforming porous medium during infiltration: viscous drag pushes the solid elements toward one another until the force is balanced by the spring repulsion.

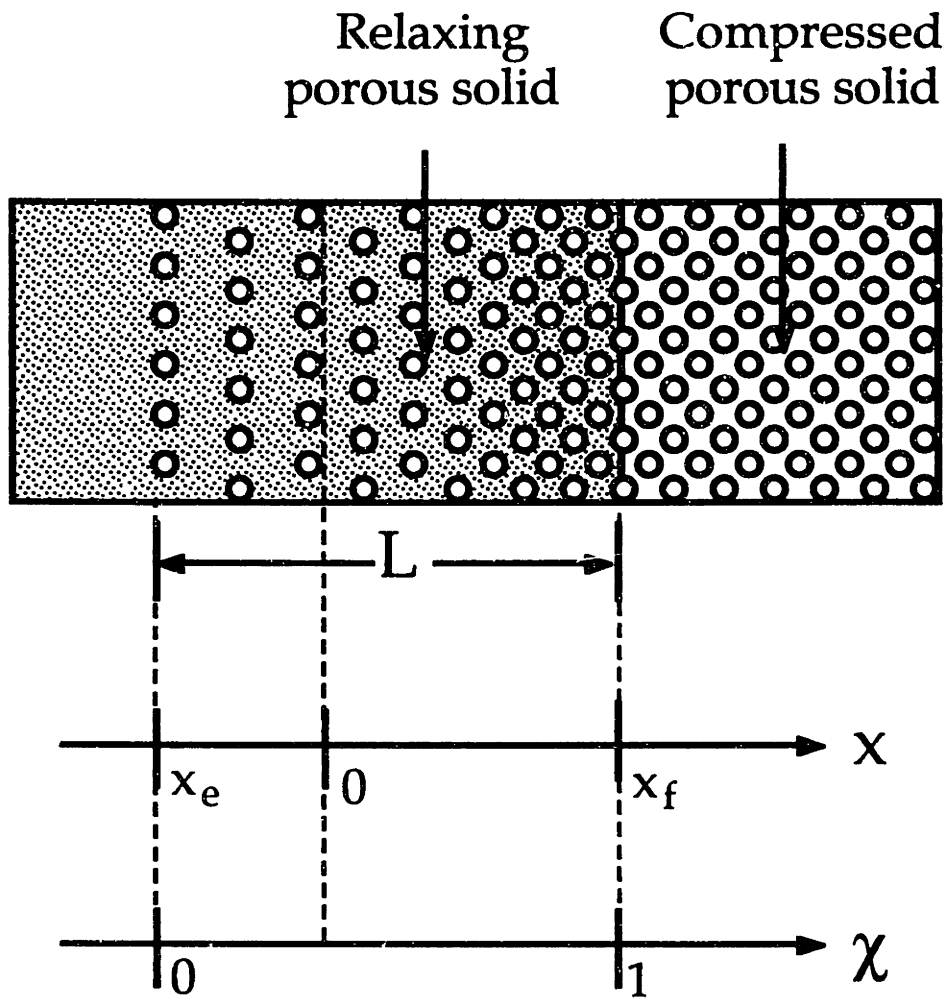


Figure (3.4) - Coordinate system used in the analysis of the infiltration of a deformable porous medium.

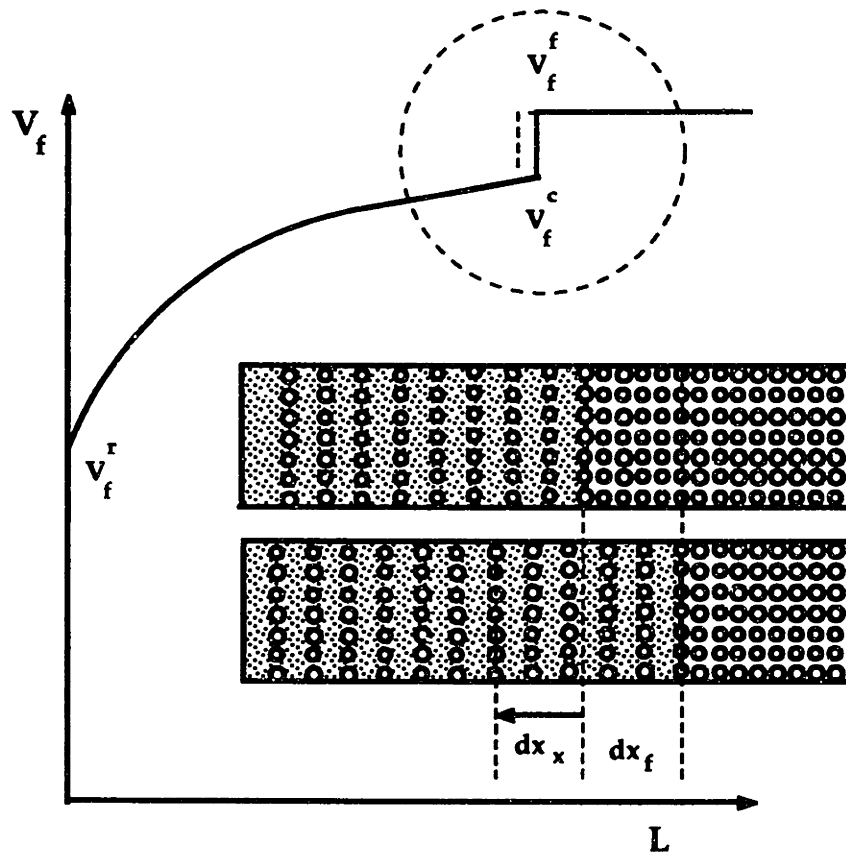


Figure (3.5) - Schematic showing the engulfed region dx_f at the infiltration front changing from V_f^c to V_f^f with a finite solid and liquid velocity.

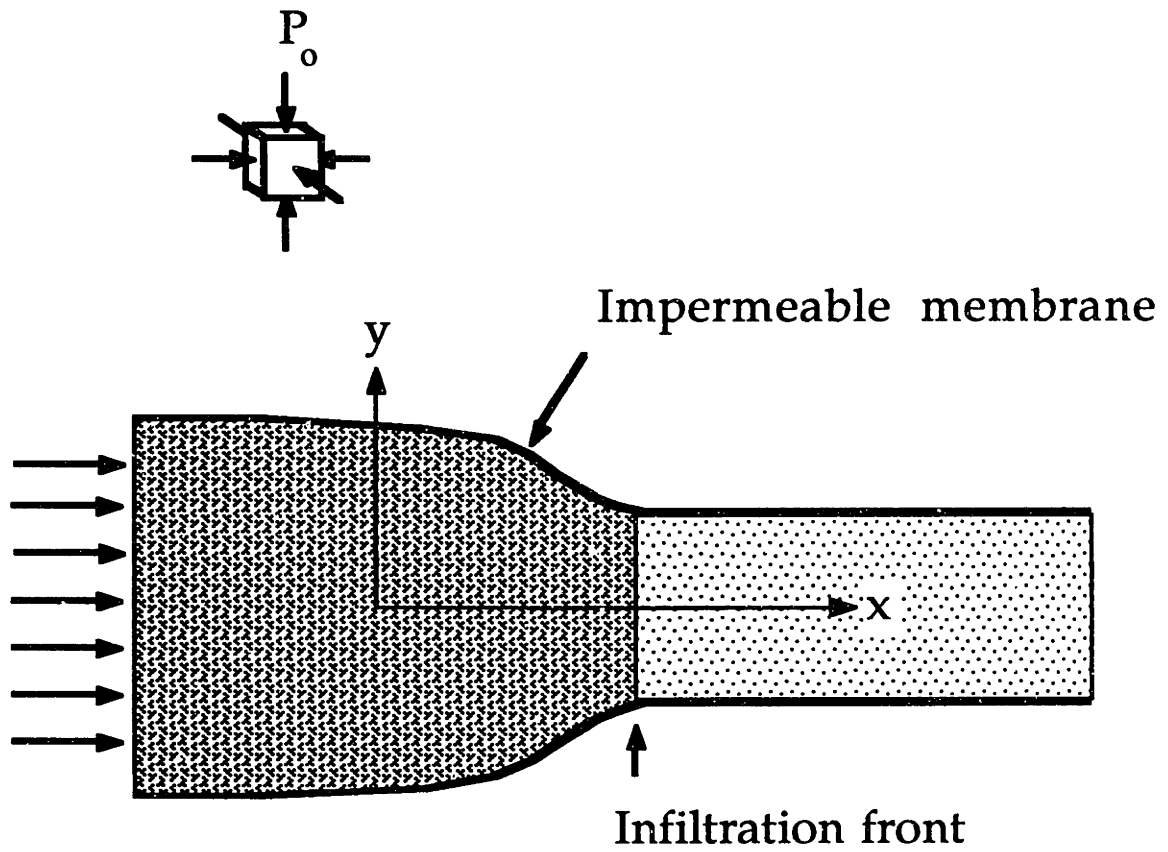


Figure (3.6) - Schematic illustrating a porous medium under unidirectional hydrostatic pressure infiltration.

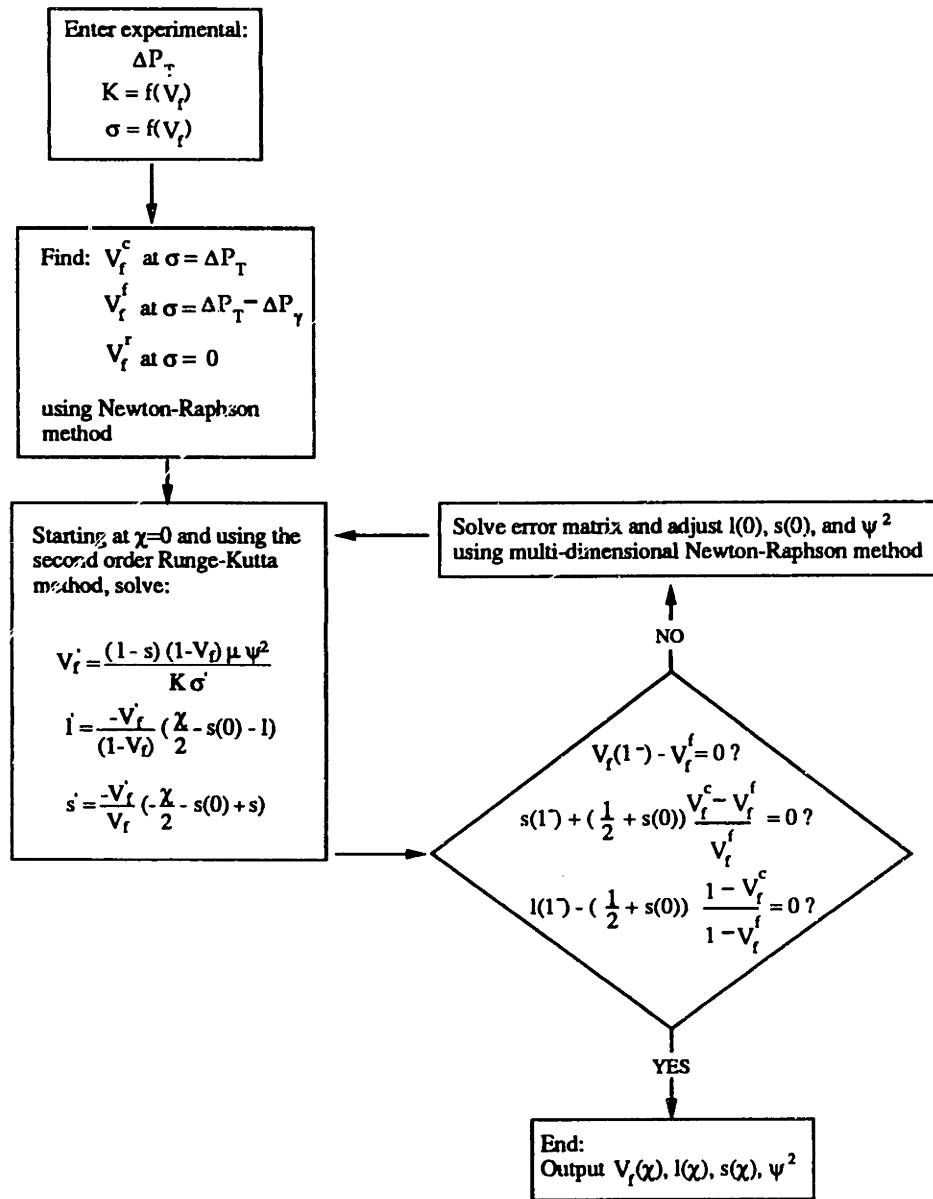


Figure (3.7) - Flow chart of algorithm used to solve the differential equations.

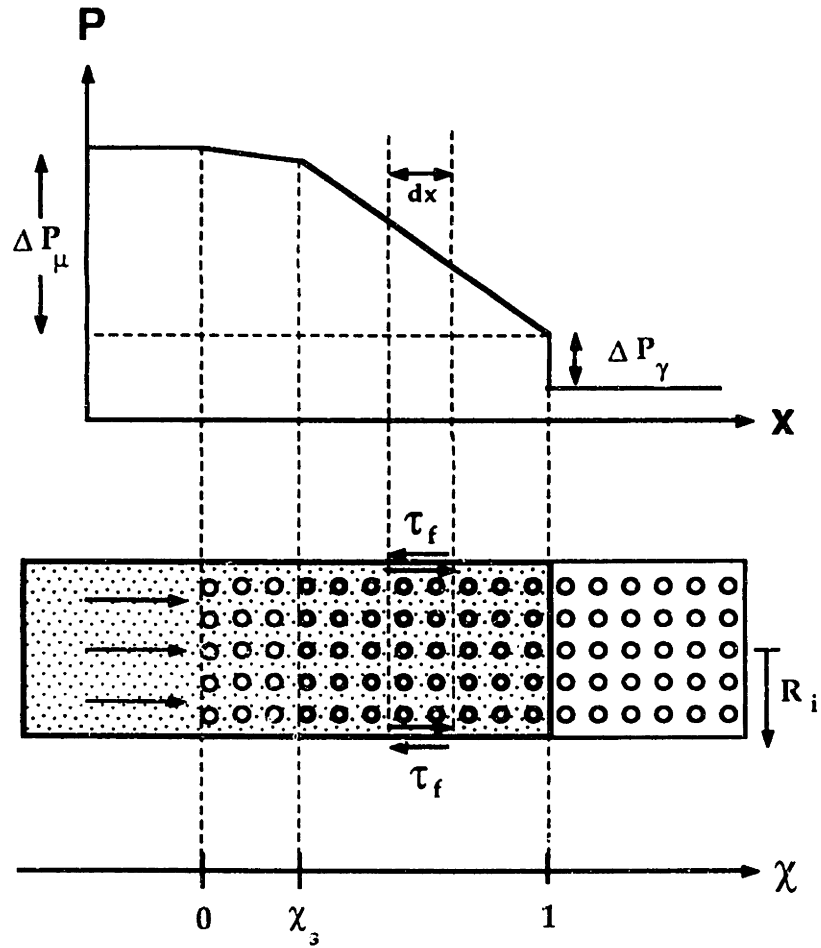


Figure (3.8) - Schematic showing the frictional stresses of the mold wall opposing the compressive stresses induced on the fibers by the liquid.

IV - EXPERIMENTAL PROCEDURES

A - INFILTRATION OF COMPRESSIBLE POLYURETHANE SPONGE

1 - Material systems

Type TF-5070-10 polyurethane sponge with a nominal density of 0.159 g/cm^3 or 13.36 volume percent polyurethane was obtained from General Plastics Manufacturing Company, Tacoma, WA. This open-celled polyurethane foam is anisotropic, in that the cells are slightly elongated along one direction, termed the "rise" direction. Figure 4.1a and 4.1b are electron micrographs of the sponge used in the experiment, respectively taken parallel and perpendicular to the rise direction. The interconnecting holes between the pores are approximately $70 \mu\text{m}$ in diameter. The sponge was found to have an average pore diameter of $450 \mu\text{m}$ cross-sectionally and $560 \mu\text{m}$ in the rise direction using the pore-intercept method on SEM micrographs. A few larger blow holes, that seem to be randomly dispersed within the matrix and are as large as 3 mm wide and 6 mm long, were also found (these were ignored in the averaging).

Prior to testing, the sponges were milled down to $7.1" \times 1.88" \times 1.88"$ ($17.8 \text{ cm} \times 4.8 \text{ cm} \times 4.8 \text{ cm}$) rectangular parallelepipeds. This was done by lining a vise on the milling machine with wide double-sided tape, inserting a sponge, and then gently closing the vise until the sponge was immobile. Using a 1" (2.54 cm) wide six-flue milling end at high speed, the sponge was gradually milled down to the proper dimensions. After machining, the sponges were weighed and their densities calculated from

their volume and the known density of polyurethane (1.19 g/cm^3). The density of the infiltrated sponges used in this work was $\rho_s = 0.159 \text{ g/cm}^3$.

Preliminary experimentation on new sponges indicated that the poroelastic behavior of new sponges varied with the number of times the sponges were compressed. Similar results were found by Parker (Parker, Mehta et al. 1987), Lanir (Lanir, Sauob et al. 1990), and Beavers (Beavers, Wittenberg et al. 1981). In order to eliminate this effect, the sponge was hydrostatically compressed at least 700 times before any characterization was done on the sponge, to allow the mechanical properties to reach a virtually unchanging state. This was done by enclosing the milled sponge inside a long, hermetically sealed plastic bag, evacuating the air out completely, and then releasing the vacuum. A thin buffer sponge was placed between the bottom of the experimental sponge and the vacuum port to ensure that the sponge was pressed uniformly along its length and to ensure uniformity of air flow throughout the sponge during cycling.

In order to measure volume fractions of the sponge and liquid velocity during infiltration, lines 0.25" (6.35 mm) apart were drawn across the width of the sponge, perpendicular to the infiltration direction.

2 - Sponge infiltration apparatus

The infiltration chamber is shown in Figure 4.2. The chamber was made of plexiglass and had inside dimensions of 2.00" by 2.00" (50.8 x 50.8 mm). The plexiglass backing consisted of a hollow aluminum base, two outlets for the vacuum reservoir, a manual vent, and an inlet for the pressure transducer. The hollow aluminum base was machined to fit loosely inside the infiltration chamber and then sealed to the plexiglass

backing with silicone rubber and epoxy to produce a vacuum seal. A 1.00" (2.54 cm) thick aluminum honeycomb along with a stainless steel screen (24 Tyler mesh) were epoxied within the aluminum base to act as supports for the sponge. The screen, which was flush with the outside edge of the aluminum base, was chosen to have very high permeability as compared with the sponge and yet have holes small enough to support the sponge effectively during infiltration. The O-ring between the plexiglass backing and the infiltration chamber prevented air leakage into the apparatus during infiltration.

The sides of the sponge were surrounded by a plastic dry-cleaning bag (0.00075" ($1.9 \cdot 10^{-2}$ mm) thick) that was hermetically sealed so as to allow the sponge to be somewhat loose inside the bag. The outer edges on one end of the sponge were sealed to the ends of the open bag by a thin 1 mm wide layer of 5-minute epoxy to prevent the bag from moving during infiltration. The other end of the sponge was supported on the aluminum base. The surrounding bag continued halfway over the outside surface of the aluminum base and was sealed vacuum-tight with electrical tape to the sides of the base. This configuration allowed liquid infiltration to occur only through the front face of the sponge, opposite the aluminum base.

Constant vacuum at the sponge end near the aluminum base was achieved by connecting the back of the aluminum base to a large 160 liter vacuum reservoir via two 0.5" (1.27 cm) internal-diameter hoses. A vacuum could be rapidly applied to the bottom of the sponge by opening two solenoid valves connected to the vacuum hoses. The open end of the infiltration chamber was submerged in a large vat of ethylene glycol containing colored dye. The entrance of the infiltration chamber was

suspended away from the bottom of the vat by a porous metal brace, built in such a way as to support the chamber during infiltration while allowing unimpeded liquid flow into the chamber mouth. A mercury thermometer was used to monitor the temperature of the fluid. A 15 psi differential pressure transducer (Omega Engineering Inc., Stamford, CT) was used between the top of the sponge and the inside of the hollow aluminum base to allow continuous measurement of the pressure drop across the sponge during infiltration.

A Panasonic AG-1830 digital video cassette recorder (VCR) was used to record the infiltration event. This VCR has the feature of being able to monitor the infiltration of the sponge and then replay the event one still field (1/60 sec) at a time. The ability to monitor progression of the infiltration front was improved significantly by using digital enhancement of the image contrast. This produced a clearer visual distinction between the infiltrated and uninfiltrated portions of the sponge.

3 - Hydrostatic compression tests

Two experiments were done to characterize the foam before actual infiltration by the liquid. These were: (1) measurements of the foam volume fraction solid, V_f , at different hydrostatic pressures, P , and (2) tests of the viscoelastic behavior of the sponge.

a. V_f vs hydrostatic pressure

The foam was placed inside a sealed plastic bag from which the air was evacuated into a vacuum reservoir. A thin "buffer" sponge was used

at the entrance of the vacuum reservoir port to shield the sponge used for infiltration from distortion caused by the vacuum port. Measurements were done using a caliper for the widths of the sponge and a ruler for the length of the sponge. Initial measurements were taken approximately 3 minutes after the sponge was totally evacuated. After the sponge dimensions were taken, a small amount of air was allowed into the vacuum reservoir and the sponge equilibrated at a lower constant hydrostatic pressure for approximately 40 seconds before distance measurements were taken again. This procedure was done from full vacuum to atmospheric pressure, taking approximately 50 minutes. From the measured dimensions of the sponge, the volume fraction of the sponge for a given hydrostatic pressure could be calculated, given the sponge weight. These tests were performed twice on the same sponge within a two-hour interval to verify reproducibility of the measurement.

b. Viscoelastic behavior tests

The strain changes of the sponge held under a constant hydrostatic pressure for both short and long time periods were measured by evacuating the sponge enclosed in a plastic bag and by measuring the width of the sponge over a duration of 40 minutes, starting from the moment when the vacuum was first applied.

4 - Foam permeability measurements

Although we neglect the progressive nature of infiltration by making the slug-flow approximation, it is important to duplicate the local liquid pressure (and hence local saturation, or volume fraction liquid)

and foam volume fraction simultaneously present in the sponge during infiltration when measuring permeability. The sponge infiltration experiment corresponds to the case described in section III-A-3-c, in which the sponge is subjected to an effective hydrostatic stress $\sigma_e = P_0 - P$, where P_0 , the applied pressure, equals one atmosphere, and P is the local pressure in the liquid. Therefore, permeability was measured for variable foam volume fractions with average liquid pressures corresponding to one atmosphere minus the mechanical hydrostatic stress required to compress the preform to that volume fraction.

In the hydrostatic pressure experiment, the volume fractions of the polyurethane foam were found by measuring the dimensions of the sponge for pressures ranging from zero to atmospheric. Four aluminum boxes, corresponding to 3.65 psi (0.0252 MPa), 4.31 psi (0.0297 MPa), 5.37 psi (0.037 MPa), and 7.58 psi (0.0522 MPa), were made to the appropriate widths and lengths derived from the hydrostatic pressure experiments on the dry sponge before infiltration. The boxes were fabricated by milling the ends of 2.00" x 2.00" (5.08 cm x 5.08 cm) aluminum square tubing (0.25" wall (6.35 mm)) to the required length needed and then cutting along the length of the square tube diagonally from opposite corners. The edges of one of the L-shaped pieces were then milled to the proper dimensions and epoxied to the inside of the other L-shaped mate, thus creating a box with the appropriate dimensions. The ends of the aluminum boxes were then sanded with a 600 grit sandpaper and smeared with a very thin layer of silicone rubber sealant to ensure a good vacuum seal.

The permeability apparatus consisted of a 100 ml graduated cylinder that had a half-inch hole drilled in the bottom. This was used to

determine permeability by recording the fluid level drop as a function of time. The base of the graduated cylinder was cemented onto a plexiglass plate that had a hole drilled through its middle to allow unimpeded fluid flow from the graduated cylinder to the sponge. On the opposite side of the plexiglass plate, a thin rubber sheet was glued to provide a vacuum seal to the aluminum box. A similar matching plate was made for the bottom of the apparatus. The aluminum box was placed between these two plates, as shown in Figure 4.3.

It was necessary for the sponge to be inserted in the box without causing damage to the sponge or allowing variational changes of localized strain within the sponge to occur from the effect of wall friction. Two sponges, with the same side dimensions as the one infiltrated, were hydrostatically compressed 700 times to full atmospheric pressure and cut into 3.00" (7.62 cm) lengths for a total of four samples, each being used for permeability measurements. Each of these cut sponges were placed in a separate sealed bag and evacuated. A thin coat of silicone vacuum grease was spread on the bag around the midsection of the evacuated sponge to prevent any side-channeling of the ethylene glycol down the folds of the plastic bag during the permeability test and to provide lubrication during packing of the sponge. Each evacuated sponge was then carefully inserted inside the aluminum box, centered between two scribed lines within the box, and allowed to expand slowly to the walls of the box. As mentioned previously, the sponge was somewhat anisotropic; the two widths of the sponge were different when evacuated, even though both sides were cut perpendicular to the rise direction; therefore, the sponge had to be inserted into the box with a proper orientation to insure duplication of

the infiltration experiment. The excess bag was then cut with a razor blade around the perimeter of the exposed face of the sponge.

Aluminum honeycomb supports and stainless steel screens cut to the inside cross-sections of the boxes were placed on both exposed faces of the sponge, with the screens lying between the sponge and honeycombs. Two 0.130" (3.3 mm) rolled aluminum foam plates (ERG Corporation, San Francisco, CA) with large pores were placed on each end of the box to allow fluid flow into the aluminum honeycomb. The aluminum box was then pressed in the permeability apparatus to create a vacuum-tight fit and bring the sponge to its proper strain using four threaded rods. The setup allowed fluid to flow directly from the graduated cylinder, through the sponge, and out through the bottom plexiglass plate. A clear Tygon tube connected to the bottom of the plexiglass plate was curved around to the level corresponding to the base of the sponge, thus ensuring that the liquid pressure head remained constant at the base of the sponge. The liquid level was maintained at this level until it ran off into the large liquid reservoir, also connected to the pressure system. An illustration of the setup is given in Figure 4.4.

To determine permeability, the system was first evacuated using a mechanical pump. The valve at the bottom of the sponge was then closed, and liquid was slowly sucked from an outside container until it rested on top of the evacuated sponge. A pressure equal to the atmospheric pressure minus the stress corresponding to the dimensions of the sponge in the box (measured in section IV-A-3-a) was slowly applied on top of the liquid until no observable drop in the liquid level was observed. An average liquid head was also included in the calculation of pressure P . This procedure caused the liquid to infiltrate

the sponge pores to the same saturation corresponding to the applied liquid pressure and sponge volume fraction that existed during the actual infiltration run. The bottom valve at the base of the sponge was then opened and the liquid was allowed to run freely through the sponge by gravitation.

Permeability was calculated from the liquid drop as a function of time using the following equation (Lambe and Whitman 1979, p. 281-292):

$$Kt = \frac{\mu L}{\rho g} \frac{A_c}{A_s} \ln \left(\frac{H}{H_0} \right) \quad (4.1)$$

where:

K = permeability of the sponge

L = length of the sponge

A_c = cross-sectional area of graduated cylinder

A_s = cross-sectional area of the sponge

H = distance from the liquid head to
the base of the sponge

H₀ = height of the head at t=0

By plotting t versus ln (H/H₀), the permeability K of the sponge could be calculated from the slope.

Saturation was determined by closing the valve on the base of the sponge and then measuring the liquid drop after atmospheric pressure had been applied on top of the liquid, assuming that the sponge is completely saturated at atmospheric pressure. Knowing the liquid drop volume and the volume of the enclosed sponge, the liquid saturation

could be calculated. The temperature of the liquid was measured immediately after the permeability experiment.

The pressure applied on the liquid was 14.44 psi (99500 Pa) minus the stress that the sponge held for its volume during the hydrostatic pressure test. The average height of the liquid to the center of the sponge was approximately 26 cm. This amounts to approximately 0.41 psi (2830 Pa), which was included in computing P . This pressure head, which drives flow of the liquid, produces negligible compression of the prestrained sponge during the experiment. This low pressure gradient driving the flow also had the advantage that pressure variations in the sponge were low during the experiment, allowing the sponge saturation to be kept constant with time and distance.

5 - Infiltration experiment data collection

The video image was used to determine the results of the hydrostatic infiltration, after image treatment to enhance the contrast and improve discernment of the infiltration front. Known distances from the screen were calibrated and converted to actual distances.

The moment when the infiltration front first contacted the sponge was defined as $t=0$. The infiltration front position was then recorded with time. By knowing the position of the infiltration front and the sponge entrance, χ , as defined in Eq. (3.9), could be calculated for each line drawn on the face of the infiltrated portion of the sponge. The width of the sponge at that point was used to determine the local V_f of the sponge, knowing the experimental curve of V_f vs. hydrostatic pressure.

B - INFILTRATION OF ALUMINA FIBER PREFORMS BY ALUMINUM

1 - Infiltration experiments

Preform blanks of Saffil™ (trademark of I.C.I., Runcorn, U.K.) alumina fibers 3 μm in nominal diameter were purchased from Thermal Ceramics (Augusta, GA). In the preforms, the fibers are randomly aligned within a plane, and are held together by a silica binder (5% percent). The volume fraction of fiber in the preforms varied between 17.8% and 20.1%. The preform blanks were 6" x 6" (15.24 x 15.24 cm) square, with the thickness varying between 0.434" (11 mm) and 0.55" (14 mm). Cylindrical plugs were cut from the blanks using a knife edge cutter and weighed to determine the fiber volume fraction V_f of each cored piece. Plugs that varied by no more than 0.2 fiber volume percent from each other were used in each experiment. Error in determining volume fraction of the cylindrical plugs is estimated to be 0.04 (Appendix 5.3-A).

These cylindrical fiber preforms were then cored to insert a sheath of Grafoil™ carbon paper (trademark of Union Carbide, Cleveland, OH) as in (Michaud 1991; Michaud and Mørtensen 1991). The Grafoil™ insert served two functions: (i) it minimized heat losses through the fused quartz tube during infiltration, and (ii) it reduced friction at the periphery of the central core, facilitating compression of the core during infiltration. To this end, a fiber coring apparatus was constructed to allow insertion of single Grafoil™ sheath through three or four preforms. In this apparatus, the preforms were placed on top of each other in a 17 mm I.D. fused quartz tube, and were then simultaneously cored together using a long 0.453" (11.5 mm) inside diameter knife-edge cutter with a 0.008" (0.2

mm) wall thickness. Once the inner cores were extracted, a sheath of Grafoil™, 1.5" (3.81 cm) to 3" (7.62 cm) wide, was placed within the inner diameter of the hole. The extracted cores were then inserted back to their original positions within the coiled Grafoil sheath. As in references (Masur, Mortensen et al. 1989; Michaud and Mortensen 1991), the preform preparation and the cutting process resulted in infiltration perpendicular to the plane within which the fibers are oriented. A detailed description of the coring apparatus and of the coring procedure is given in Appendix (4.1).

The infiltration apparatus and procedure were essentially identical to those described in (Masur 1988; Masur, Mortensen et al. 1989), with a few modifications for the present experiments. As in (Masur 1988; Masur, Mortensen et al. 1989), the position of the liquid infiltration front advancing through the preform was monitored using a SiC monofilament as a variable resistor. Because the inner core of the Saffil fiber preform was quite narrow, and because any misalignment of the SiC monofilament may interfere with preform compression, a procedure was devised to insert the monofilament straight through the middle of the preform core. This was achieved by drilling the monofilament using a pin vise together with a collapsing guide made of a 5 $\mu\ell$ glass pipette and a 100 $\mu\ell$ glass pipette to prevent the monofilament from buckling or breaking. An aluminum cylinder with a hole drilled in its center was also used to stabilize and center the glass pipettes during drilling. Prior to inserting the SiC filament into the preform, the upper portion of the SiC fiber was electroplated with a nickel coating. The bare portion of the filament was drilled and then pulled through the preform until the

nickel coating interface was exactly on top of the preform. The monofilament insertion procedure is given in detail in Appendix (4.2).

Essentially, the infiltration apparatus consists of two parts: a lower chamber, where an electrical resistance heater in the bottom is used to melt the aluminum in a high-density graphite crucible, and a cap, holding the sample, heater, thermocouples, pressure transducer, and other electrical devices.

In a typical experiment, the SiC monofilament was threaded through the center hole of a copper disk used to provide stable backing for the Saffil™ fibers during infiltration and as a chill to prevent overinfiltration by the molten aluminum. The copper was insulated from the fiber by a ceramic tube that fit snugly inside the center hole of the copper. On top of the disk, ceramic spacing tubes that extended to the back of the O-ring fitting were placed to brace the preforms during infiltration.

The fibers were heated separately from the metal using the same helically-wound resistance heater as in (Masur 1988; Masur, Mortensen et al. 1989). This heater tended first to heat the fibers well above 373 K regardless of the set temperature, which was only reached subsequently. The temperature range within a length of 45 mm inside the heater is less than ± 5 K (Masur 1988; Masur, Mortensen et al. 1989). Most experiments that were run in this study comprised three preform elements, with the total length of the preform being less than 45 mm. There were a few experiments, however, that required four preforms with the total length extending to 46 mm, for which experimental error was closer to ± 10 K.

The aluminum matrix, initially 99.999% pure, was donated by ALCOA, Pittsburgh, PA. Crucibles used to melt the metal were made of

graphite by Union Carbide, Cleveland, OH. To infiltrate the preforms, the cap of the apparatus was lowered over the main vessel, immersing the end of the fused quartz tube sample and melt thermocouple into the bath of molten metal. The molten metal was then pushed into the tube and the preforms by pressurizing the entire vessel with nitrogen gas via two apertures in the cap. Full pressurization was achieved in less than one second and was held until the infiltration front in the preform stopped, typically after about 8 seconds. During infiltration, the metal position and the pressure were continuously recorded on a chart recorder using the SiC monofilament and a pressure gauge, respectively.

2 - Fiber compression tests

Compression tests of fiber preforms were performed so as to replicate conditions inside the fused quartz tube during infiltration. Basically, one preform of a certain V_f was cored and sheathed in a fused quartz tube in the same manner as described above, except that the carbon sheath was allowed to extend above the preform approximately 1-2 cm. Within this sheath, a stainless steel plunger was placed, machined to the same diameter as the preform inner core diameter. A ceramic support centered on top of the plunger was used to push the plunger during the compression test. The preform rested on the surface of a stainless steel base, which was slightly smaller in diameter than the fused quartz tube. The specimen and its base were heated using a helically wound electric resistance furnace or heating tape that was wrapped uniformly on the outside of the fused quartz tube. In order to monitor the temperature of the fibers, a thermocouple was placed on the outside of the sheath to rest

on the surface of the outer preform core. All compression tests were done at 423 K to remove adsorbed moisture from the preforms. After holding the fibers at 423 K for 20 minutes, they were compressed unidirectionally by pushing down the upper ceramic support with an Instron™ (Canton, MA) testing machine at cross-head speeds of 0.02" or 0.05"min⁻¹ (0.51 mm·min⁻¹ or 1.3 mm·min⁻¹, respectively). Curves of preform volume fraction versus pressure were then derived from the cross-head displacement and the stress given by the load cell.

3 - Fiber permeability

The permeability of the fiber preforms was measured by mounting a fiber preform in an epoxy resin and measuring water flow rates through the preform. To prevent flow of the epoxy into the preform while mounting the preforms, a thin coating of rubber-to-metal cement was applied to the outside surface of the preform and allowed to dry. Prior experimentation showed that the cement penetrated the preforms by less than 0.003" (0.08 mm), which assured that the final dimensions of the porous preform were virtually unchanged. After allowing the rubber cement to dry, one end of the preform was placed in the middle of two strips of electrical tape, lying adjacent to one another with the sticky side up. The sides of the tape overlapped very slightly to prevent leaking of the epoxy. A pregreased phenolic ring form, used for an outer barrier for the epoxy liquid, was placed over the preform, centered, and pressed onto the sticky electrical tape to create a seal. Five-minute epoxy was then mixed and poured in the gap between the preform and ring form until the level of the epoxy reached the top surface of the preform. After

curing, the rubber cement on the faces of the preform was carefully peeled away, exposing the preform fibers. The specimen was then removed from the ring form.

The apparatus for measuring permeability is shown in Figure (4.5). O-rings that were wide enough to fit onto the epoxy mount away from the exposed face of the preform were placed on both sides of the specimen and then pressed between two plexiglass plates over 0.25" pipe-threaded holes drilled through the thickness of each plate. On the opposite side of one plate, a graduated cylinder, used as the standpipe in the permeability experiments, was sealed using silicone adhesive. The bottom of the cylinder had been cored out prior to being glued using a diamond coring drill. The other plate had a 0.25" brass hose fitting.

In order to measure the permeability, the whole apparatus was initially turned over and the brass hose fitting was filled with water. The end was then plugged, quickly inverted, immersed in a constant-level water reservoir, and then unsealed. This procedure prevented bubble entrapment from occurring on the underside of the preform. Water was then poured into the end of the graduated cylinder and the height of the falling head from the water reservoir was recorded as a function of time to deduce the preform permeability (Lambe and Whitman 1979).

Recorded permeability values were found to increase with time from the beginning of water flow, stabilizing after about 30 min. The values of permeability used in this work were steady-state values.

A second, somewhat less rigorous, procedure for measuring permeability was also devised, and is described in Appendix (4.3).

4 - V_f determination in infiltrated specimens

On three samples, the volume fraction fiber V_f along the length of the infiltrated sample was measured by a weighing method. The infiltrated sample was cut lengthwise with a low speed diamond saw. One half was used as a metallographic sample. The other half was cut into slices 2 to 2.5 mm thick using a diamond saw. Each individual slice was weighed and dissolved in a dilute solution of HCl, with the residual fiber mass being used to determine the V_f of the slice.

The Grafoil™ sheath allowed easy separation of the inner core of the cut composite slices. The volume of each slice was then calculated after measuring the thickness and widths of the specimen using a micrometer, using the formula:

$$\text{Volume} = C \times \left\{ r^2 \sin^{-1} \left[\frac{\alpha}{r} \right] + \alpha \sqrt{r^2 - \alpha^2} \right\} \quad (4.2)$$

where:

$$r = \frac{A^2}{8B} + \frac{B}{2},$$

$$\alpha = r - B$$

and other terms are defined in Figure (4.6). The tip of the infiltration front had a somewhat irregular shape and the preform entrance was usually too thin to get an accurate measurement, so these parts were not used.

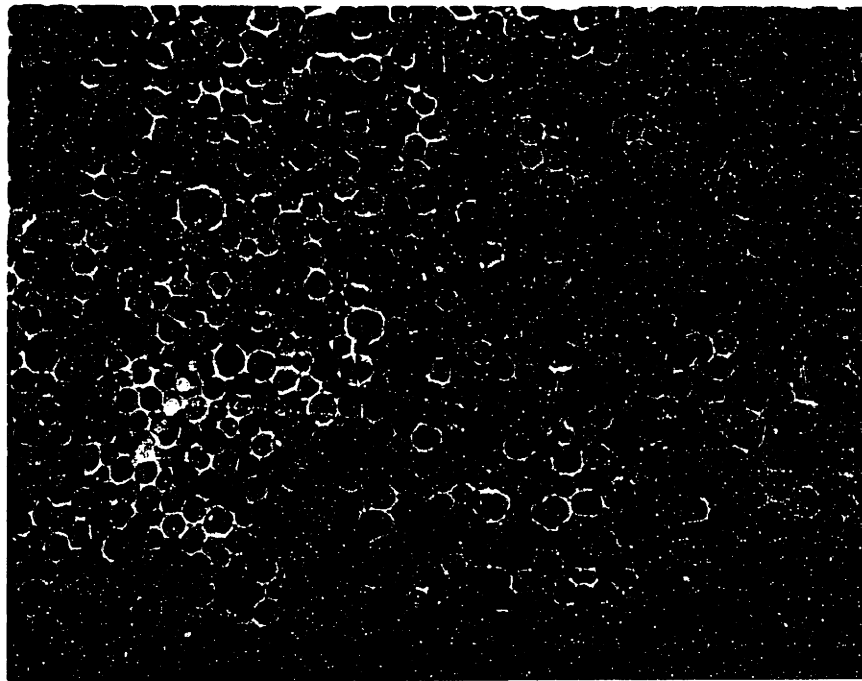
After measurement of their dimensions, the slices were immersed in a 20% HCl solution to dissolve the matrix. The residual fibers were

then filtered using 0.45 μm Duropore™ Neoprene filter membranes from Millipore Corporation, Bedford MA. The fibers were dried at 383 K and weighed to determine volume fractions of the individual slices. The volume fraction of each slice was assigned to its longitudinal midpoint. Experimental error in the resulting measurement of V_f was estimated as $\Delta V_f/V_f \approx 7\%$ in Appendix (5.3-C).

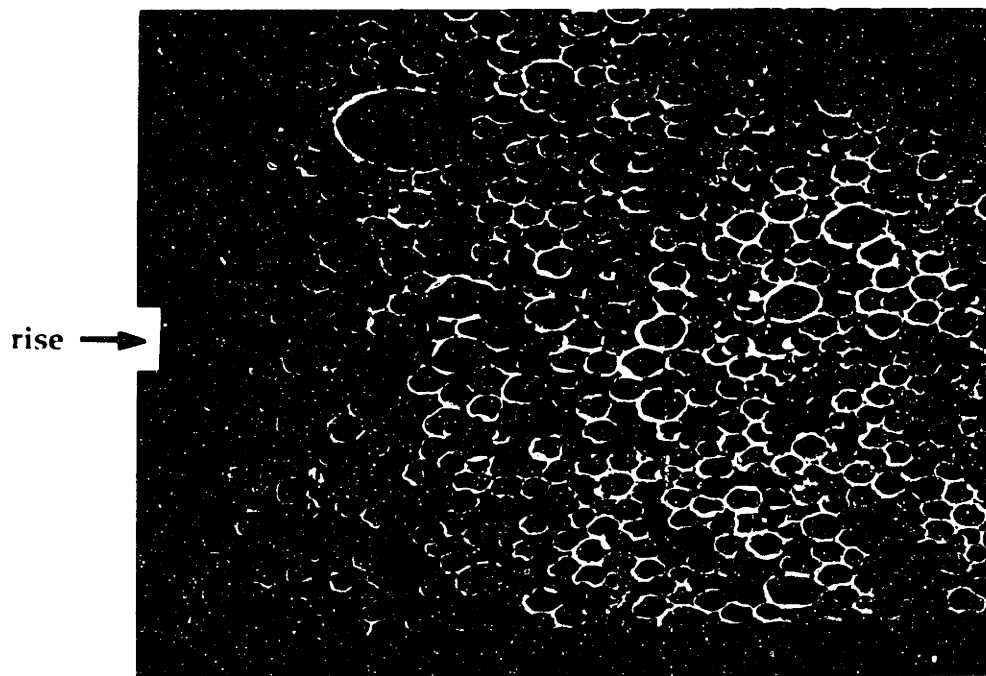
5 - Metallography

Longitudinally cut samples were mounted in epoxy resin and ground on SiC papers from 240 grit to 600 grit, using distilled water as a lubricant. 6 μm diamond paste with water was used on perforated Texmet™ (trademark of Buehler, Lake Bluff, IL) cloth for 20 min, followed by final polishing with a colloidal silica suspension on Chemomet™ (trademark of Buehler, Lake Bluff, IL) cloth. The samples were agitated by ultrasound in ethanol after each step, rinsed afterwards with ethanol, and then blown dry.

To distinguish the position of the remelting front in samples infiltrated with superheated metal (Mortensen, Masur et al. 1989), these were etched in a mixture of 50 ml HCl (37%), 47 ml HNO₃ (70.3%), and 3 ml HF (51%) for about 5-10 s and then immediately washed in water. This etchant produces small etch pits in pure aluminum, facets of which are parallel to the [100] planes of the metal crystals (Brandes 1983).



A



B

Figure (4.1) -
(a) Micrographs of the polyurethane foam viewed along the rise direction.
(b) Micrographs perpendicular to the rise direction.

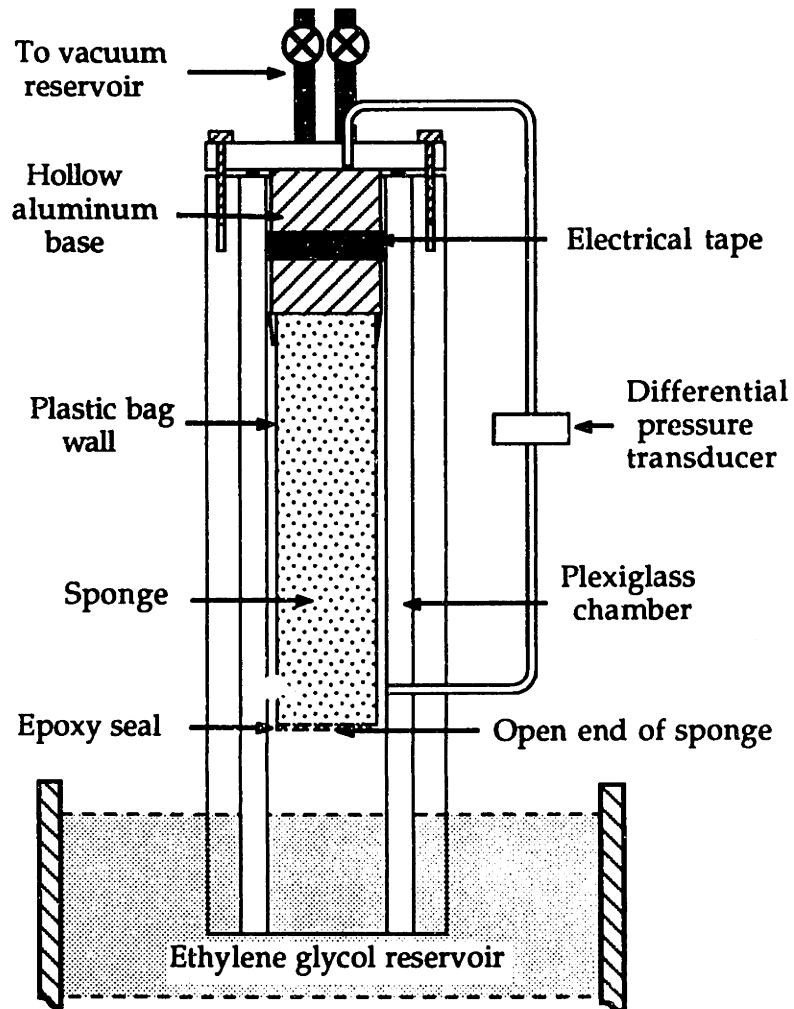


Figure (4.2) - Schematic of the chamber used to infiltrate the sponge with ethylene glycol.

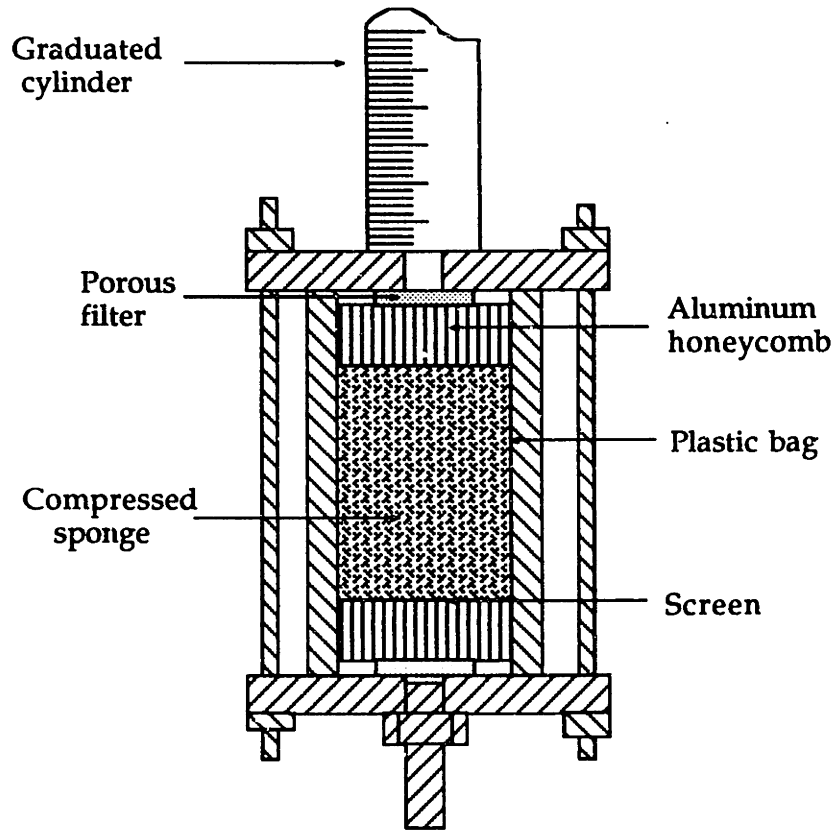


Figure (4.3) - Setup to test permeability of sponge in same conditions as the actual hydrostatic infiltration

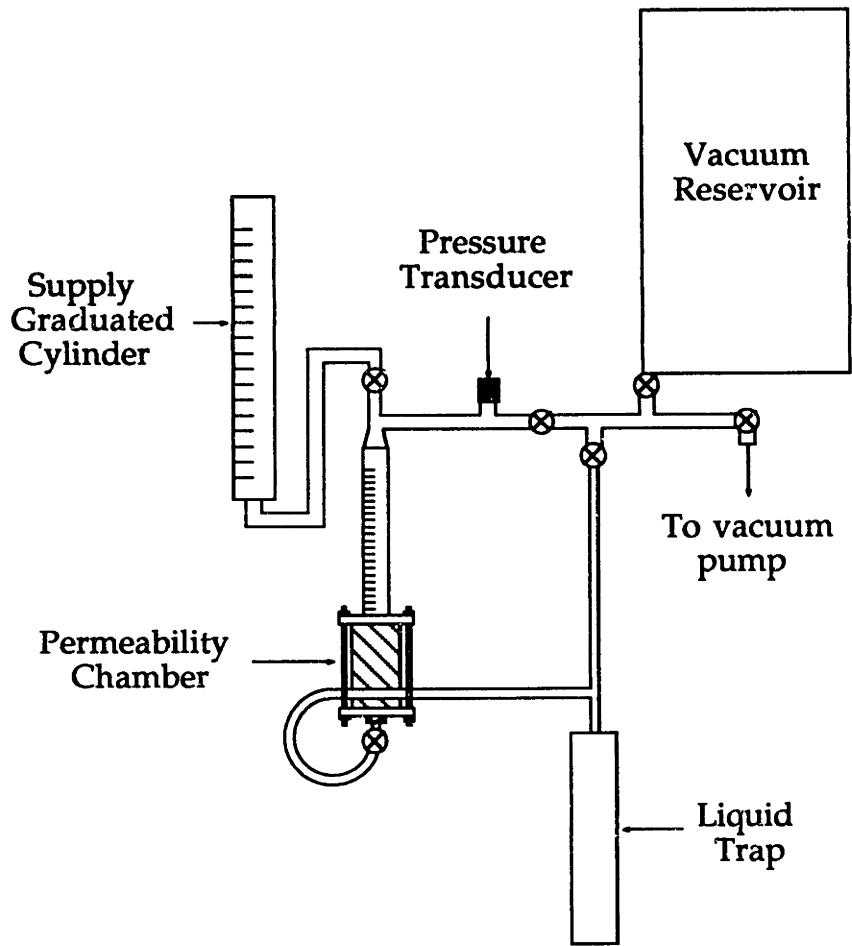


Figure (4.4) - Overview of the apparatus used to test sponge permeability under various strain and saturation conditions.

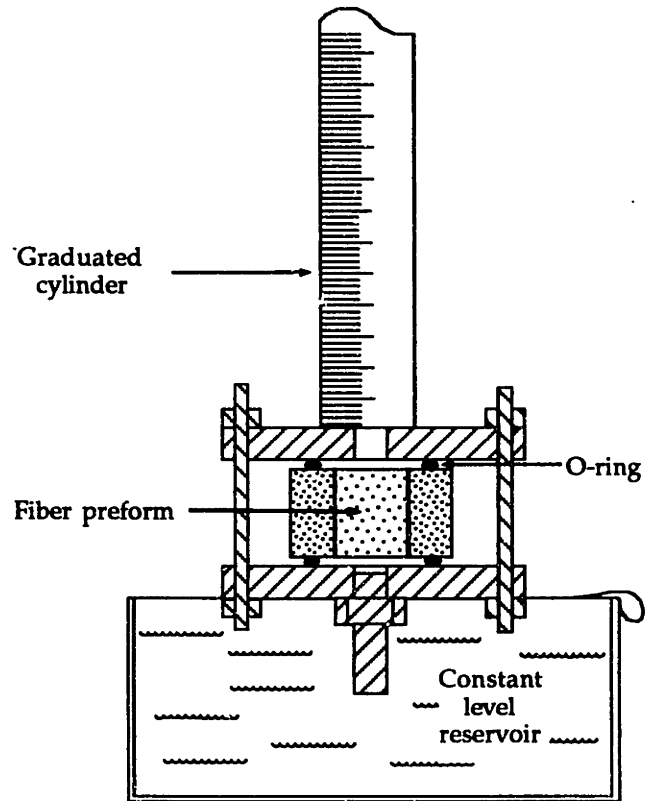


Figure (4.5) - Illustration of method used to determine the permeability of Saffil™ fibers with water using the falling head method.

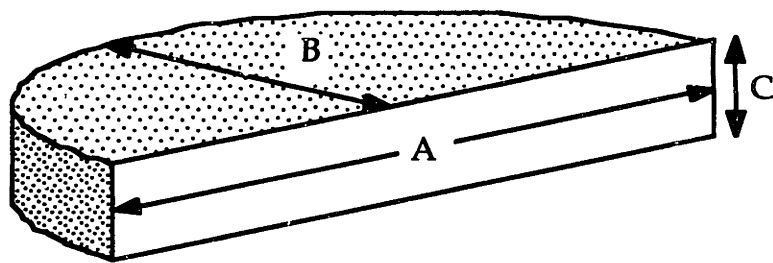


Figure (4.6) - Dimensions used in calculating volume of composite slices for volume fraction measurements.

V - RESULTS

A - INFILTRATION OF POLYURETHANE FOAM

1 - Hydrostatic pressure vs V_f

The results of the hydrostatic pressure test are shown in Figure 5.1. The curves resemble qualitatively those of Beavers (Beavers and Wilson 1975; Beavers, Wittenberg et al. 1981), Parker (Parker, Mehta et al. 1987), and Lanir (Lanir, Saub et al. 1990), although direct comparison is difficult because the sponges in this study were hydrostatically compressed, whereas previous studies compression was performed uniaxially. Also, the densities of the sponges used in this study were on the order of six times higher.

There was no noticeable difference between data from the two tests done two hours apart from each other. For modeling purposes, the average of both curves was fit with a seventh-order polynomial:

$$\sigma = A + B*V_f + C*V_f^2 + \dots H*V_f^7 \quad (5.1)$$

where:

$$A = -2.329164 \times 10^7 \text{ Pa}$$

$$B = 7.1349318 \times 10^8 \text{ Pa}$$

$$C = -9.255285 \times 10^9 \text{ Pa}$$

$$D = 6.597487 \times 10^{10} \text{ Pa}$$

$$E = -2.791823 \times 10^{11} \text{ Pa}$$

$$F = 7.0165383 \times 10^{11} \text{ Pa}$$

$$G = -9.702267 \times 10^{11} \text{ Pa}$$

$$H = 5.698018 \times 10^{11} \text{ Pa}$$

The high order of the polynomial was necessary to preserve the shape of the curve at the sharp transitional points, as Equation (3.16) dictates that $V_f'(\chi)$ will approach infinity as σ' approaches zero. The error in measuring the V_f with the calipers and ruler is calculated in Appendix (5.2-A) to be 0.03.

2 - Viscoelastic behavior of the sponge

Curves of sponge volume fraction V_f vs. time are shown in Figures (5.2a) and (5.2b). As seen from Figure (5.2a), V_f changes relatively little after the vacuum has been applied for more than 20 seconds. The change of V_f between 20 seconds and 60 seconds is approximately 0.012. V_f for longer relaxation times is shown in fig (5.2b). The average V_f of the sponge between 20 s and 60 s is only lower than the V_f of the sponge at 40 minutes by about 0.021. This suggests that the sponge reaches a pseudo-steady state condition in 20 s, and continues to relax slowly afterwards.

3 - Sponge permeability

Table (5.1) and Figure (5.3) summarize sponge permeability measurements. The data points are fitted well by an exponential curve:

$$K = K_0 * 10^{(-M V_f)} . \quad (5.2)$$

K_0 and the exponential term, M , were determined to be $1.4729 \cdot 10^{-10} \text{ m}^2$ and -6.9654 , respectively. The viscosity of ethylene glycol as a function of temperature is given in Appendix (5.1). The error calculated for the permeability is approximately $\frac{\Delta K}{K} \approx 0.10$, as shown in Appendix (5.2-B).

In Table (5.1), θ_v represents the fraction of unfilled void space at a total pressure of one atmosphere and liquid pressure P , assuming there is complete saturation at $P = 1$ atmosphere. It was also observed that the ethylene glycol did not spontaneously wet the sponge, i.e., θ_v equals 1.0 for a liquid pressure $P = 0$.

Table 5.1 - Polyurethane foam permeability

Effective stress (MPa)	Liquid pressure (MPa)	Occupied chamber volume (cm ³)	Δ ml liquid change	V_f	K (m ²)	θ_v unsaturated void fraction
0.025	0.075	143	0	0.163	$1.0 \cdot 10^{-11}$	0
0.03	0.07	119	0.5	0.195	$7.1 \cdot 10^{-12}$	0.005
0.037	0.063	99.3	1.0	0.234	$3.5 \cdot 10^{-12}$	0.013
0.052	0.048	82.3	1.5	0.283	$1.5 \cdot 10^{-12}$	0.025

4 - Experimental results for sponge infiltration

The temperature of the ethylene glycol immediately before infiltration was 25.8° C. The pressure drop registered between the infiltration front and the back of the sponge during the actual event was 14.44 psi (99500 Pa). Various times during the infiltration are reproduced

from the video images in Figures 5.4a through 5.4d. In these figures, the infiltration front is highlighted using the digital video recorder, as described above. This enhancing mode tended to add visually 1.0 mm to the widths of the sponge while the vertical distances were unaffected. The conversion factors used to change screen distances to actual distances in the horizontal and vertical directions also varied slightly.

A plot of L^2 vs time is shown in Figure 5.5. As can be seen in the figure, the curve becomes a straight line after approximately 17 seconds. The value of ψ^2 obtained from the slope of the line was $1.2 \cdot 10^{-4} \text{ m}^2 \text{ s}^{-1}$ with an experimental error of 10% (Appendix (5.2-D)).

Measured volume fraction V_f of the sponge vs. χ during infiltration is shown in Figure 5.6. As the infiltration front moves through the sponge, the volume fraction profile within the infiltrated portion of the sponge should remain constant in this transformed axis. At earlier times, the curves tend to be shifted more to the left, i.e., to greater values of V_f . At longer times, greater than 17 seconds, the sponge profile tends to stabilize, although there still is a small shift to the right as the sponge continues to relax.

B - INFILTRATION OF ALUMINA FIBER PREFORMS BY ALUMINUM

1 - Infiltration experiments

Table (5.2) lists all infiltration experiments along with their processing parameters. Virtually all samples were well infiltrated, except for the small porous region that existed in the tip region. At high applied pressures, the porous regions were only a few percent of the total length

of the sample. The matrix microstructure is similar to that found in previous experiments (Masur, Mortensen et al. 1987; Masur 1988; Mortensen, Masur et al. 1989): the matrix is fine-grained, except in the remelted zone, as shown in Figure (5.7). Within this zone, long columnar grains extended parallel to the infiltration direction. In most samples, the remelting front separating the fine-grained from the large-grained regions exhibited some curvature, with the concave side toward the preform entrance.

It was observed that none of the outer preform rings had undergone compression after infiltration, since the base of the preforms in the solidified samples was still located flush against the indentation or alumina cement in the fused quartz tubes. On the other hand, it was observed that in several samples (marked as such in Table 5.2), the central core of the preform had moved relative to the outer ring, with the implication that this portion of the preform had undergone visible compression during infiltration, Figure 5.8. In some instances, only a portion of the central preform core had compressed, after tearing away from the remainder of the preform, which remained at its original position near the entrance, Figure 5.9.

It was found by measuring the length of infiltrated outer preform rings, or central cores of samples that did not compress, that these were somewhat smaller than preform lengths measured before packing and coring the preforms. Since these preforms had not moved during infiltration, this slight increase in their volume fraction resulted from packing and coring operations. The nominal volume fraction of fiber for these samples was therefore corrected when possible by computing V_f from the lengths of the outer infiltrated rings instead of the preform

heights measured before preform packing and coring. The corrected volume fractions are listed in Table 5.2 as " V_f^a ".

Distributions of V_f in three composite cores, samples I, J, and K, were measured and are plotted in Figures 5.10, 5.11, and 5.12. Horizontal and vertical error bars for these experimental data points were calculated as described in Appendix (5.3-C) and Appendix (5.3-D) for the measurement of V_f . The V_f distribution of two other samples were also measured but not recorded because no reliable ψ^2 value was obtained during infiltration and excessive damage or compression may have occurred to the preforms during the packing procedure.

In samples that apparently underwent no compression, curves of L^2 versus time, t , were similar to those found in preceding investigations (Masur, Mortensen et al. 1989; Mortensen and Wong 1990). For these samples, ψ was determined, as in previous investigations, using the linear portions of these curves.

By comparison of infiltration lengths measured with the SiC monofilament with the position of the infiltration front in samples, it was determined that in some instances, the SiC monofilament had moved, whereas in other samples, it had remained stationary. Therefore, in samples that underwent preform compression, some uncertainty exists in measured values of L , because it is uncertain whether the SiC monofilament remained stationary, or moved with the preforms as they compressed during infiltration. It must therefore be kept in mind that infiltration distances, L , measured with the SiC monofilament are records of the position of the infiltration front relative to the SiC monofilament, rather than the infiltration front position measured in a fixed reference frame or relative to fibers contained in the final infiltrated composites.

Records of L^2 versus t display three regions, similar to those described by Masur (Masur 1988), with the central portion of the curves linear, as for samples exhibiting no compression. The difference between these curves and those for samples in which the preform did not compress is in a pronounced decrease of the slope of L^2 versus t before, or at the onset of, the linear portion of the curve. We take this abrupt change in slope of L^2 versus t as an indication of sudden preform compression, during which most motion of the SiC monofilament and preform entrance takes place (this is substantiated in the discussion below). The length of infiltrated composite at time t , $L_{c(t)}$ was then computed as the final length of the infiltrated composite, \mathcal{L} , minus $(L_f - L(t))$ where L_f is the final value of L recorded by the SiC monofilament, and $L(t)$ is the infiltration front position recorded by the SiC monofilament at time t (Figure 5.13). For samples where delamination occurred, the fiber-free gap was not included in \mathcal{L} . Ψ was then computed from the slope of the linear portion of plots of L_c^2 versus t . The relative experimental error in L_c thus computed arises mostly from uncertainty in the position of the preform entrance at time t . $\Delta L_c/L_c$ was therefore estimated as equal to the distance separating the initial from the final preform entrance positions in the composite, ΔL_c , divided by \mathcal{L} . The relative experimental error in ψ is then roughly equal to $\frac{\Delta L_c}{L_c}$, since time is measured with much greater precision. When no compression occurred, ΔL_c is estimated to be about 1.5 mm. ΔL_c , \mathcal{L} , and experimental error in ψ^2 are tabulated in Table 5.3.

Table 5.2 - Experimental conditions for the aluminum/alumina fiber composite samples.

Exp #	Exp # (lab book)	V_f^o	V_f^a	T_f (°C)	T_o (°C)	P (MPa)	Purity (% en measured)	Grafoil™ Wrap (mm)	ψ^2 (m s ⁻¹) (· 10 ⁻⁵)	$\frac{dP_{max}}{dx}$ (MPa · m ⁻¹)	Com- pressed
A	14.58	.184	.190	98	660	2.05		76	21.9	116	N
B	14.60	.178	.185	75	660	2.14		76	24.7	97	N
C	14.66	.191	.191	74	660	2.07	.9999	38	3.7	150	Y
D	14.67	.191	.194	100	660	2.10	.9997	38	7.1	119	Y
E	14.69	.190	.200	60	660	2.66	.9999	38	3.9	116	Y
F	14.72	.194	.198	100	660	1.34	.9999	38	12.6	88	N
G	15.13	.185	.196	300	660	2.07		38	98.0	58	N
H	15.02	.195	.205	100	714	2.14	.9996	76	9.7	227	Y
I	15.20	.190	.190	100	714	2.12	.9994	70	3.2	366	Y
J	15.22	.188	.193	100	704	3.69		70	-	842	Y
K	15.23	.185	.188	150	709	2.11		70	13.2	176	Y
L	15.27	.192	.193	100	714	1.45		70	5.3	114	N
M	15.64	.192	.192	167	771	2.15		70	40.3	116	Y

Table 5.3 - Compression distances, final infiltration distances, and experimental errors in L_c .

Exp #	ΔL_c experimental (mm)	\mathcal{L} experimental (mm)	$\frac{\Delta L_c}{\mathcal{L}}$	Compressed
A	-	28.7	0.05	N
B	-	29.4	0.05	N
C	3.8	6.3	0.60	Y
D	2.9	12.5	0.23	Y
E	5.2	10.9	0.48	Y
F	-	11.6	0.13	N
G	-	34	0.04	N
H	0.3	13.8	0.11	Y
I	3.3	6.4	0.57	Y
J	8.3	7.5	1.11	Y
K	2.3	27.1	0.08	Y
L	-	10.7	0.14	N
M	0.5	37.2	0.04	Y

2 - Compressibility of Saffil™ alumina fiber preforms

Figure 5.14 shows the unidirectional compression curve of fiber preforms for various values of initial fiber volume fraction V_f^0 . Virtually all tests were done in a cyclic manner (Figure 5.15), successively increasing the load from 200 psi (1.38 MPa) to 500 psi (3.45 MPa), the highest pressure that was used for infiltration experiments.

Curves of uniaxial stress, σ , versus V_f first exhibit a region of elastic deformation in which the apparent modulus is high and where

unloading curves superimpose on loading curves. This is followed by a plastic region of lower apparent modulus, in which unloading shows significant permanent deformation of the preform.

Overall, there is a trend for preforms to compress to higher V_f for a given stress as V_f^0 decreases. At higher strains, data were only found almost to converge if V_f^0 was greater than about 0.19.

The thickness of the Grafoil™ sheath surrounding the inner core of the preforms (which varied with the initial length of foil used) had no apparent effect on the compression behavior of the samples. No effect of compression strain rate on preform compressibility was found. No effect of temperature was found provided the temperature exceeded 100°C. Therefore, temperature variations over the length of the samples, estimated to be below 50°C, had no influence on the data. Below 100°C, a sharp reduction in apparent modulus of the preforms was observed.

A summary of the compression test data is given in Table 5.3.

Table 5.3 - Summary of alumina fiber compression tests done at $T_f = 150^\circ\text{C}$

Preform #	V_f^o	Wrap length (mm)	Preform Length (mm)	Crosshead speed	Heating
A-8-2-47	0.176	70	13.2	0.02"/min	tape
A-8-2-48	0.180	70	13.2	0.05"/min	tape
A-8-2-14	0.188	38	11.8	0.02"/min	tape
A-8-2-3	0.194	38	11.7	0.02"/min	tape
A-7-2-24	0.195	70	11.5	0.05"/min	furnace

3 - Permeability of the fiber preforms

The first measurement of preform permeability, K , obtained after 30-40 s flow of water, was defined as the initial permeability. Thereafter, the measured permeability increased to reach a steady-state value after about 30 minutes. Plots of initial and steady-state permeability vs. V_f are given in Figure 5.16 and summarized in Table 5.4 for preforms used in this work, as well as for two earlier preforms used in the work of Masur et al. (Masur, Mortensen et al. 1987; Masur, Mortensen et al. 1989).

From these data, Equation (26) of reference (Mortensen, Masur et al. 1989) was used to compute the apparent fiber radius r_f in the preforms, as in preceding investigations (Masur, Mortensen et al. 1989; Mortensen and Wong 1990). r_f is plotted as a function of V_f for the two preform types in Figure 5.17. It is found that r_f is relatively constant for each type of

preform, but differs with the type of preform, being equal to 2.72 μm and 2.34 μm for steady-state permeability of preforms used here and in previous investigations, respectively. Values for initial hydraulic radii are 2.45 μm and 1.95 μm , respectively, this last value being in agreement with measurements of Masur (Masur 1988; Masur, Mortensen et al. 1989).

In the present work, the steady state value of the apparent fiber radius $r_f = 2.72 \mu\text{m}$ is used to compute the preform permeability, rather than the initial value. It is seen from Figure 5.17 that Equation (26) of reference (Mortensen, Masur et al. 1989) provides a value in reasonable agreement with measured steady-state K for the preforms.

Table 5.4 - Fiber permeability summary

Source	V_f^o	K (initial) ($\cdot 10^{-12} \text{ m}^2$)	r (initial) ($\cdot 10^{-6} \text{ m}$)	K (steady state) ($\cdot 10^{-12} \text{ m}^2$)	r (steady state) ($\cdot 10^{-6} \text{ m}$)
A	0.187	1.90	2.46	2.42	2.77
	0.196	1.70	2.45	2.45	2.76
	0.197	1.68	2.44	2.01	2.67
	0.200	1.67	2.49	2.00	2.72
	0.208	1.42	2.40	1.77	2.67
B	0.222	-	-	1.11	2.31
	0.223	0.80	1.95	1.17	2.36

Fiber Source: A- Thermal Ceramics, B- Vernaware

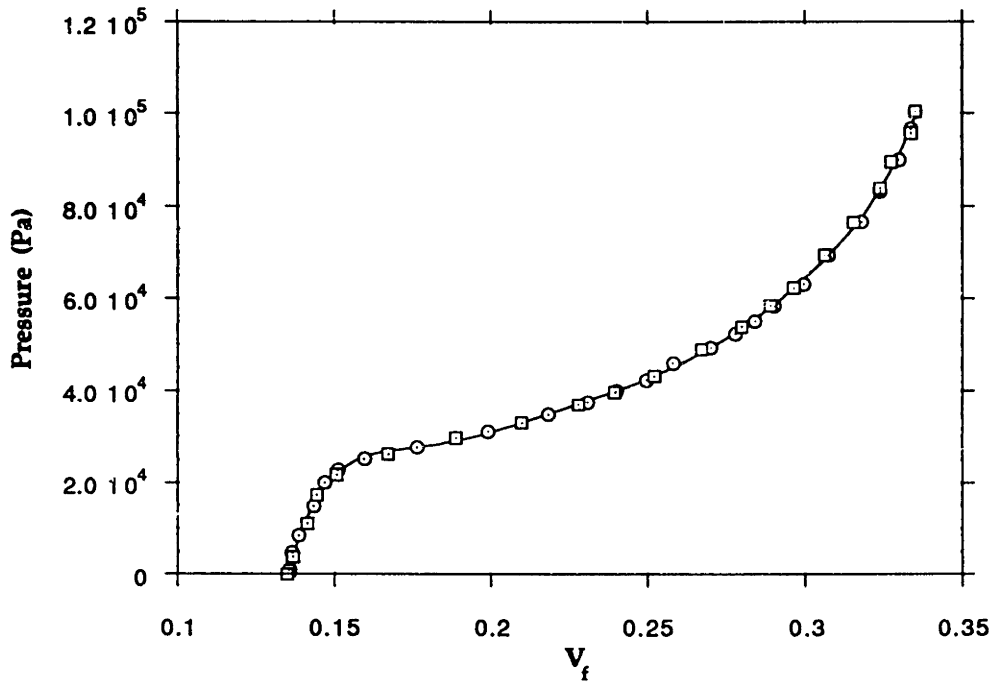
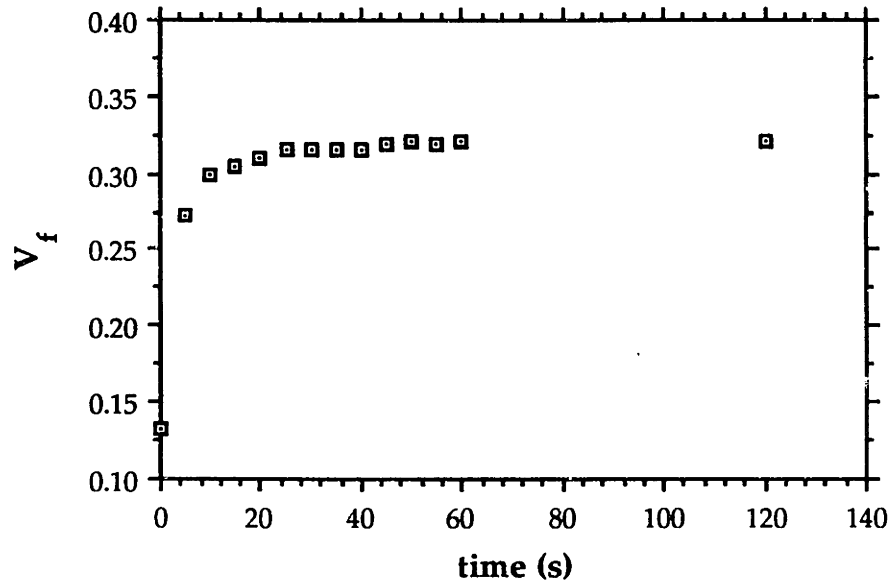
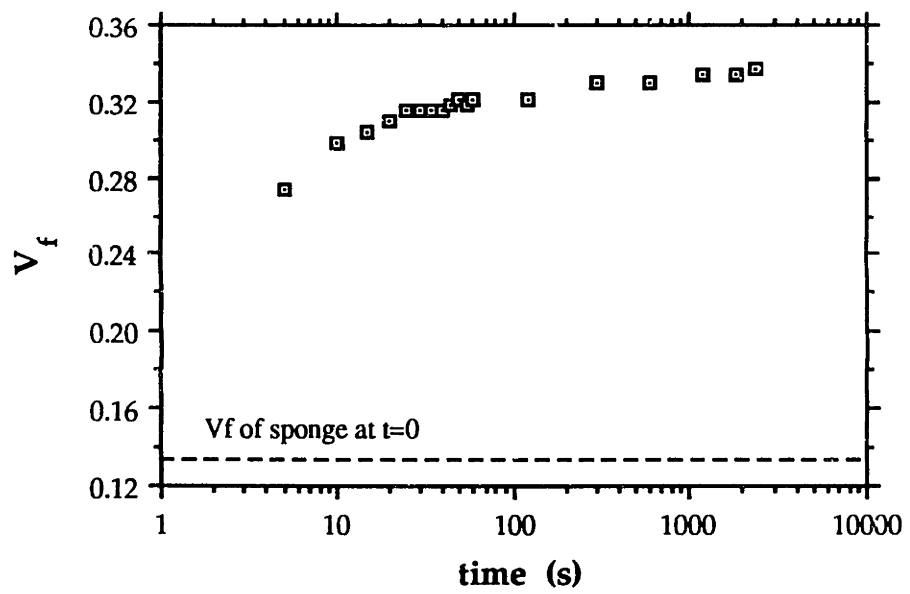


Figure (5.1) - Plot of the results for two separate foam hydrostatic pressure tests, done approximately two hours apart on the same sponge used for the actual infiltration. Squares and circles are from two separate experiments.



A



B

Figure (5.2) -
 (a) Plot of V_f of sponge under 0.1 MPa hydrostatic pressure for short times (0 to 60 s).
 (b) Plot of same experimental data for longer times (1 s to 40 min).

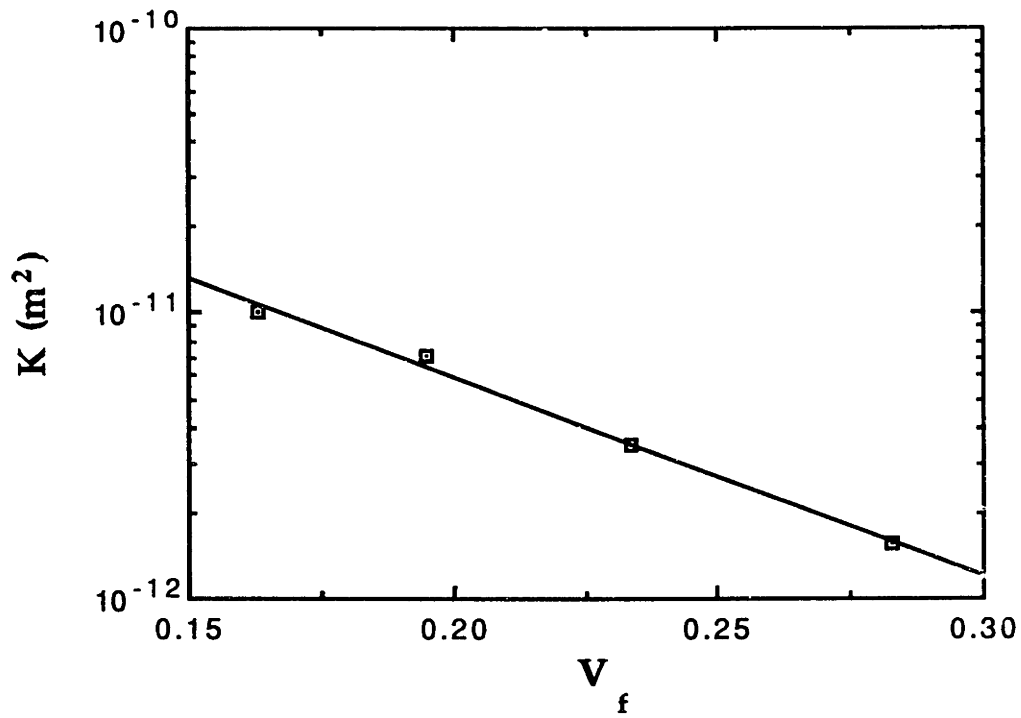
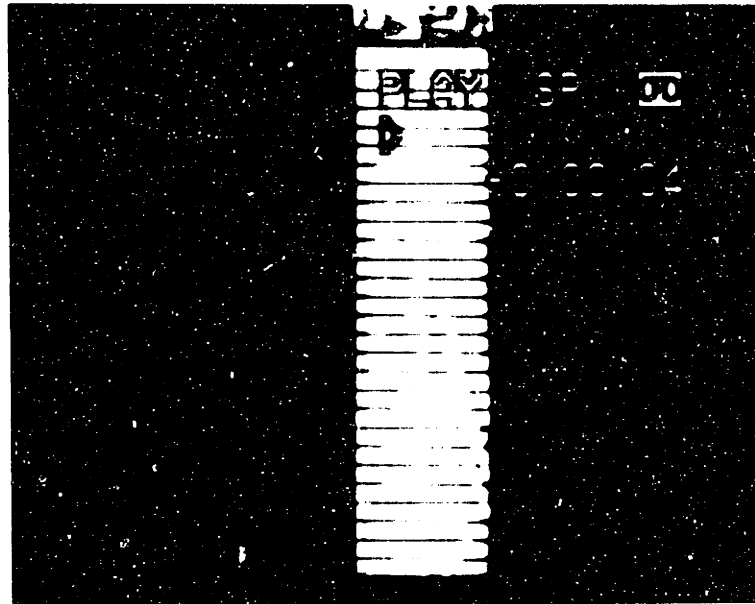
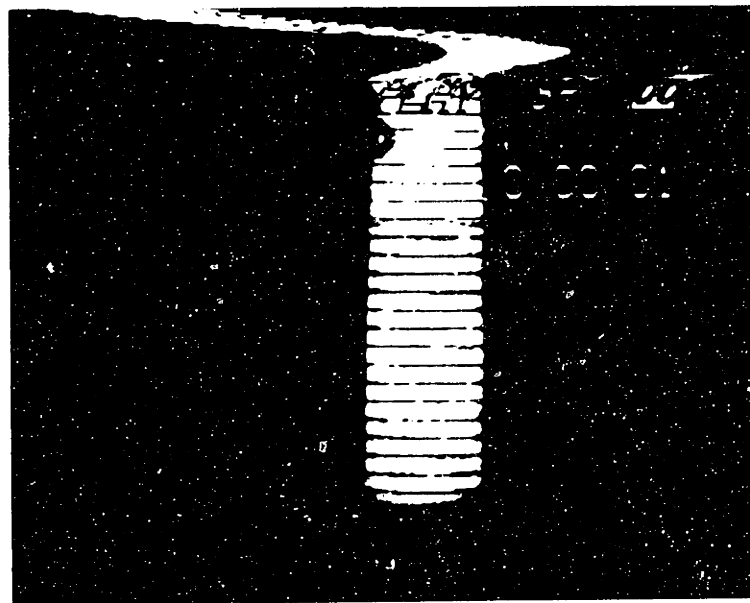


Figure (5.3) - Experimental sponge permeability as a function of volume fraction. Straight line corresponds to: $K = 1.4729 \cdot 10^{-10} m^2 \cdot 10^{(-6.9654 \cdot V_f)}$.



A



B

Figure (5.4) - Video images of sponge infiltration experiment at: (a) $t < 0$ s, (b) $t = 1$ s, (c) $t = 31$ s, (d) $t = 67$ s. Distortion of the image occurred on the top of the screen when the image was in the digitized mode.

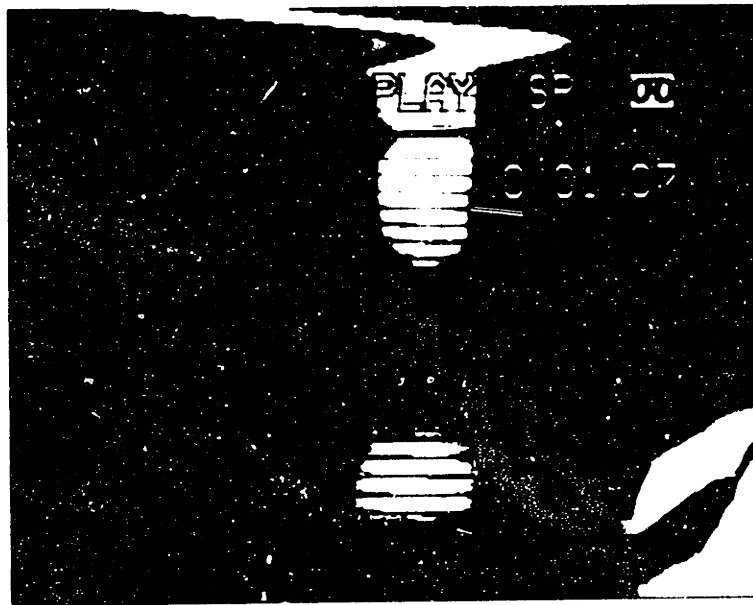
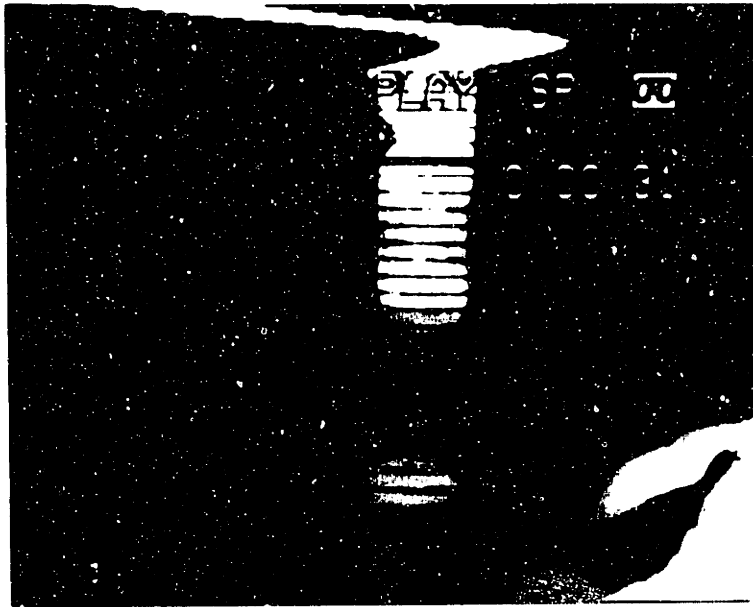


Figure (5.4) (continued) - Reproduced video images of sponge infiltration experiment at: (a) $t < 0$ s, (b) $t = 1$ s, (c) $t = 31$ s, (d) $t = 67$ s.

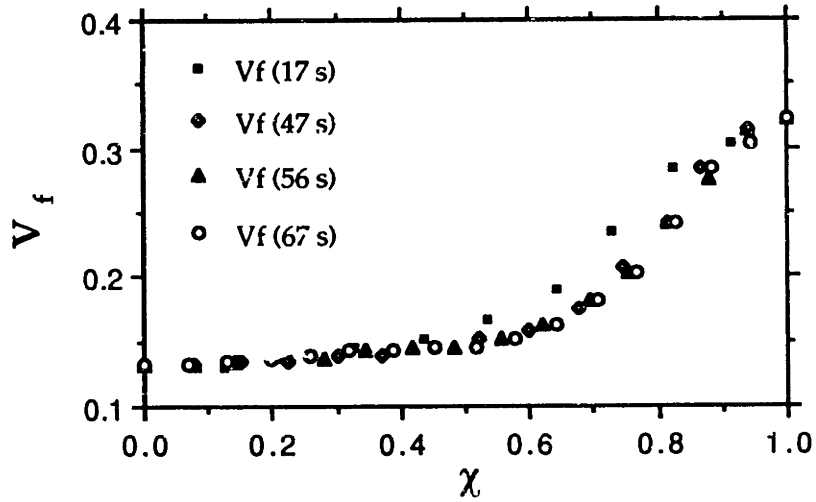
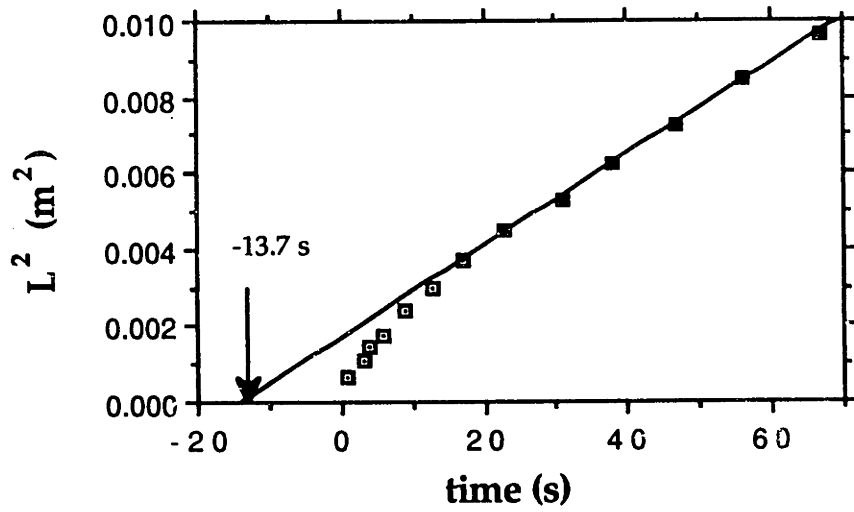


Figure (5.5) - Total infiltrated length L^2 as a function of time.

Figure (5.6) - Experimental V_f distribution along infiltrated length of sponge at various times.

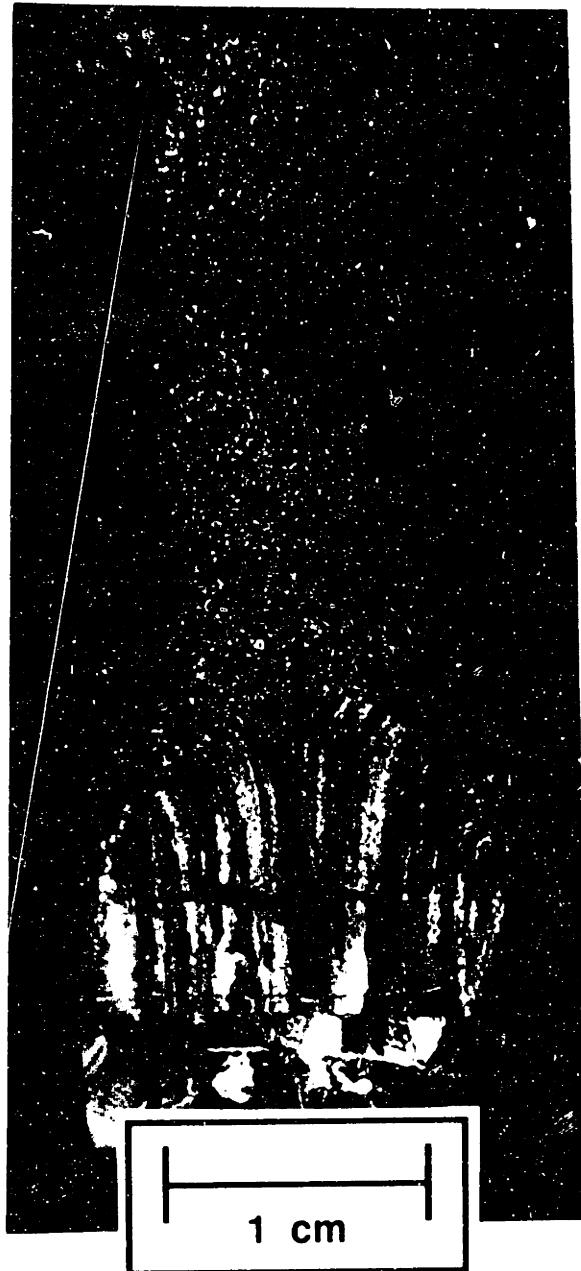


Figure (5.7) - Macrostructure of a longitudinal section of sample M (etched). The matrix consists of fine grains with long columnar grains extending within the remelted region. A small delaminated region in the composite also exists within the remelted region.

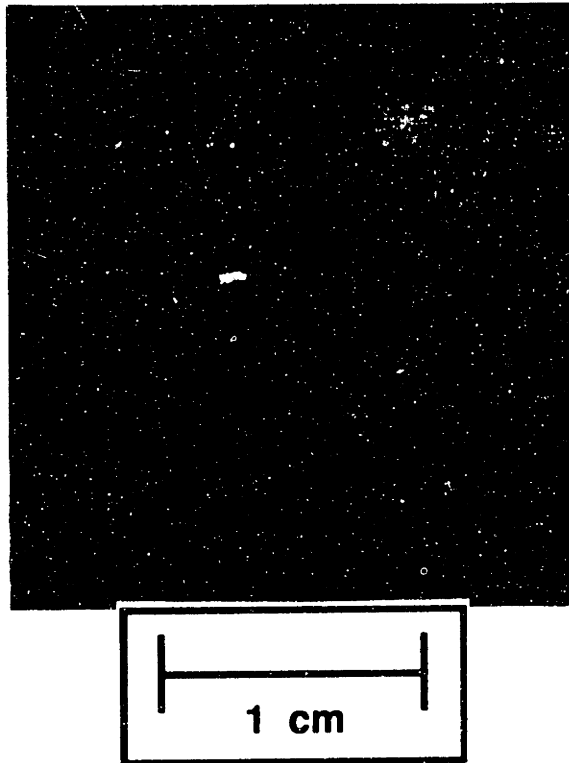


Figure (5.8) - Macrostructure of a longitudinal section of compressed sample E.

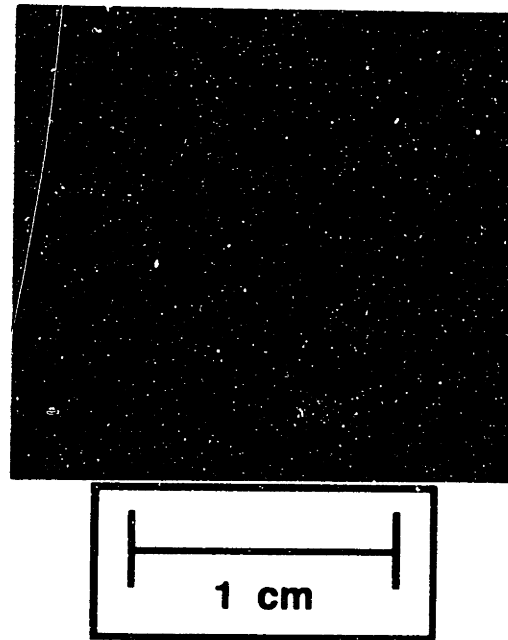


Figure (5.9) - Macrostructure of a longitudinal section of sample K (etched). Remelted zone extends into compressed fiber region.

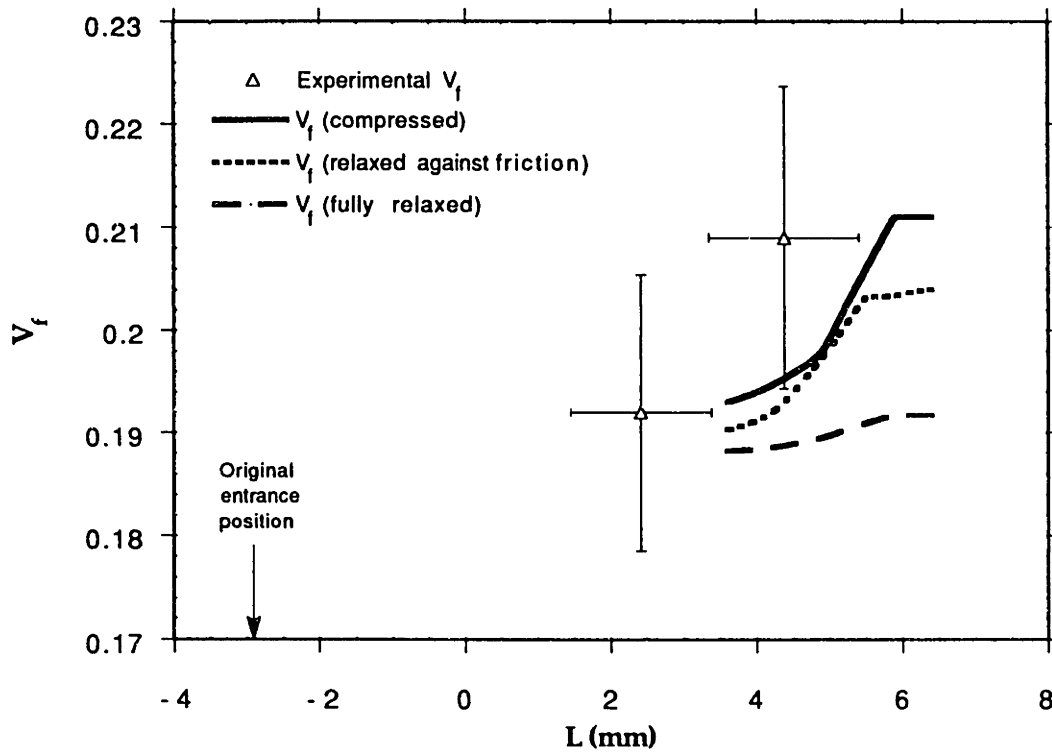


Figure (5.10) - Measured V_f distribution along infiltrated length with predicted values of V_f for no relaxation, $\sigma = \frac{2\tau_s}{R_i}$, and full relaxation (sample I).

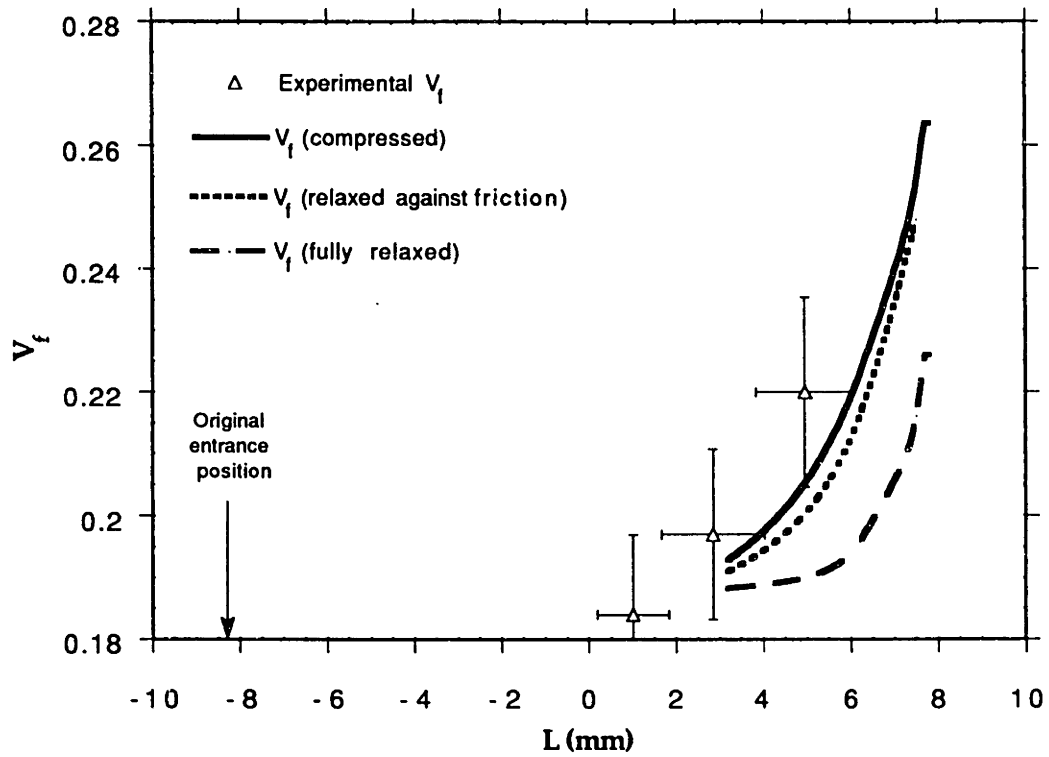


Figure (5.11) - Measured V_f distribution along infiltrated length with predicted values of V_f for no relaxation, $\sigma = \frac{2\tau_s}{R_j}$, and full relaxation (sample J).

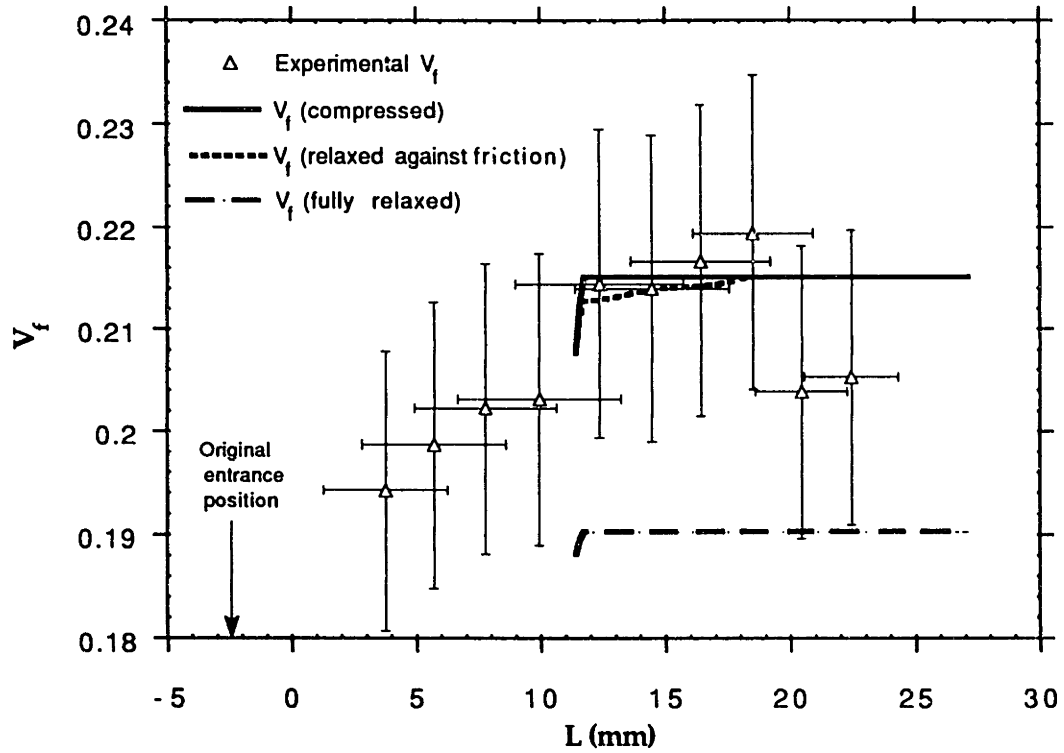


Figure (5.12) - Measured V_f distribution along infiltrated length with predicted values of V_f for no relaxation, $\sigma = \frac{2\tau_s}{R_i}$, and full relaxation (sample K).

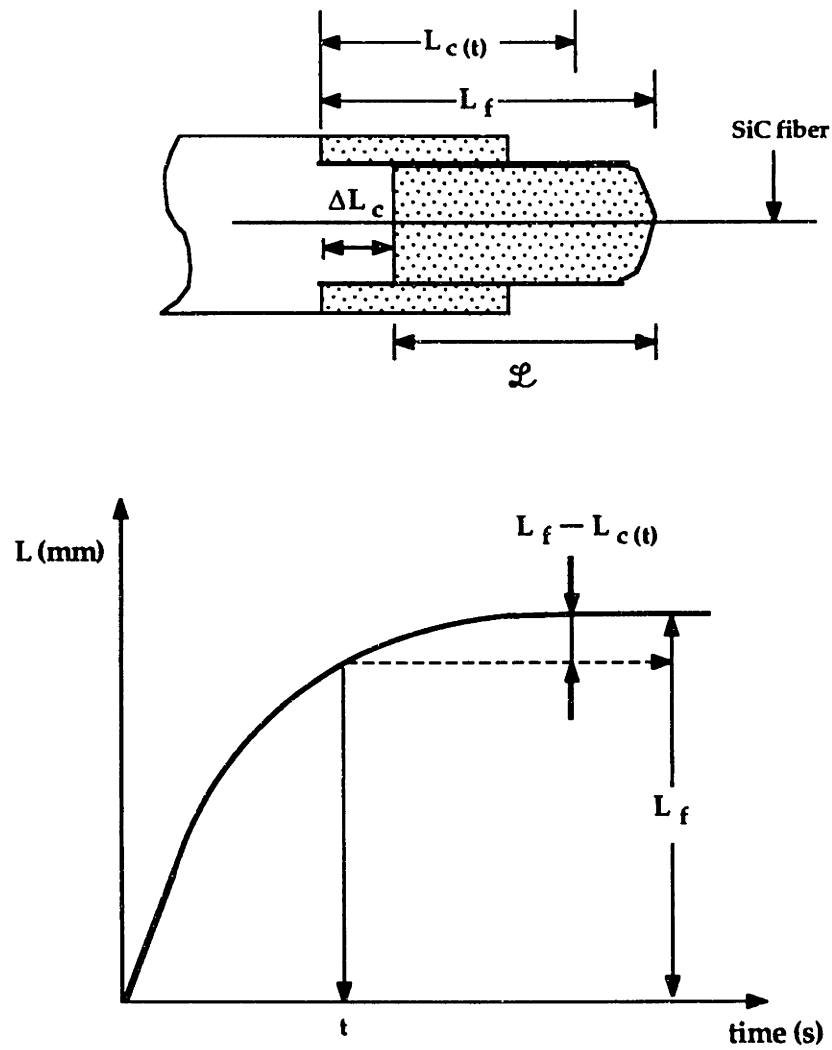


Figure (5.13) - Schematic illustration of method of data collection from SiC monofilament when preform compression occurs.

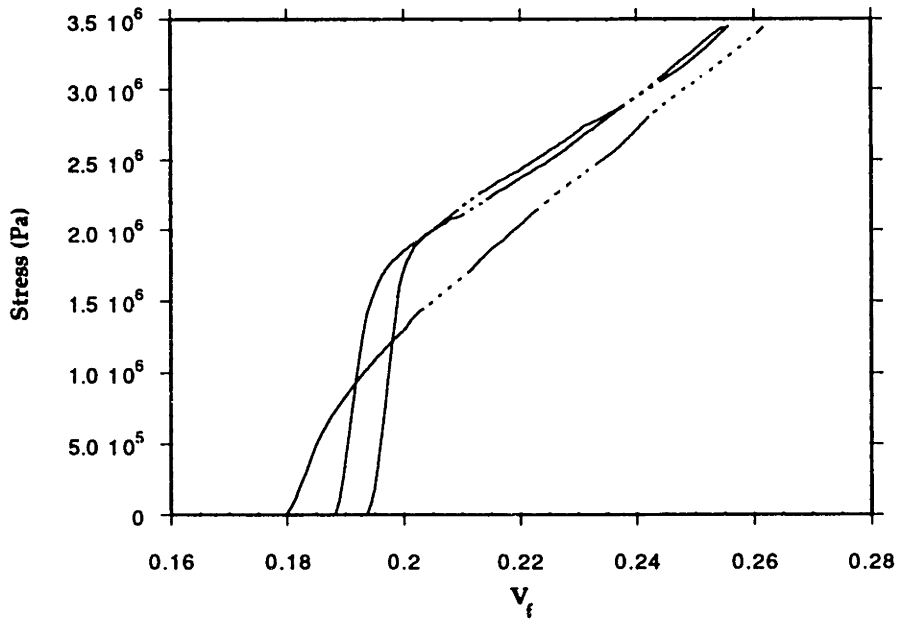


Figure (5.14) - Unidirectional compression curves for fiber preforms of $V_f^0 = 0.180, 0.188, \text{ and } 0.194$ and $T_f = 150^\circ\text{C}$. The dotted line indicates extrapolation of the data between unloading - reloading cycles.

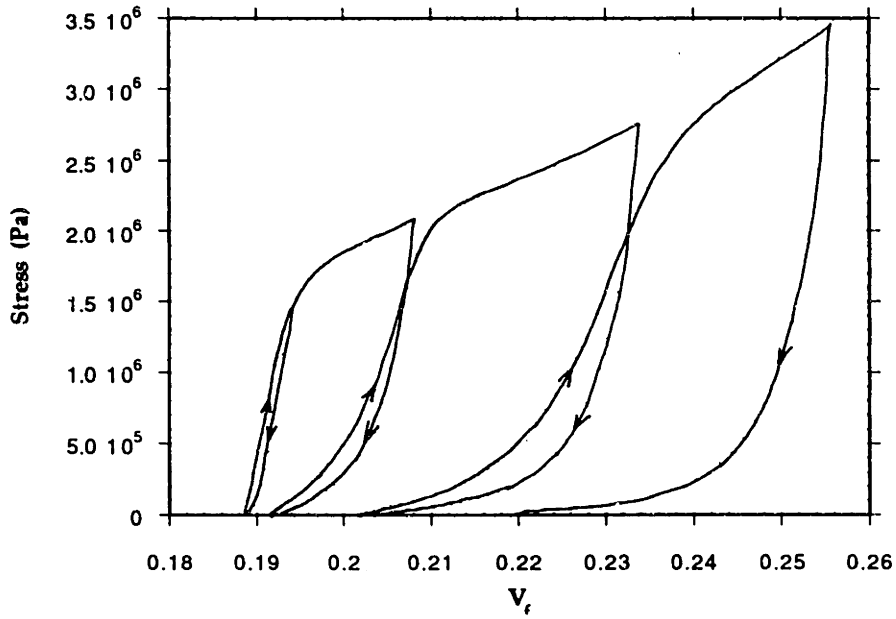


Figure (5.15) - Stress-strain cyclic compression of a fiber preform of $V_f^0 = 0.189$ and $T_f = 150^\circ\text{C}$, increasing the maximum load from 1.38 MPa (200 psi) to 3.45 MPa (500 psi).

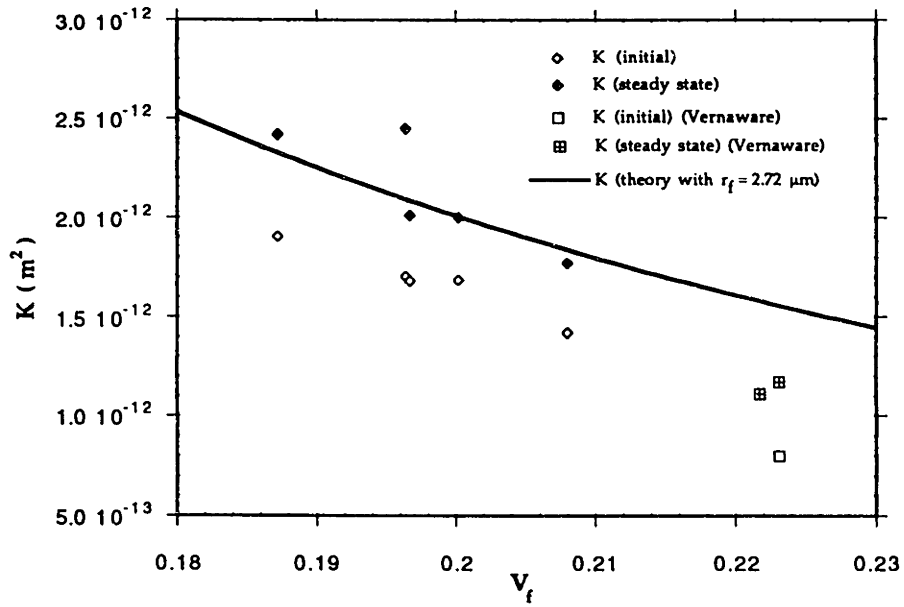


Figure (5.16) - Plots of initial and steady-state permeabilities vs. various V_f^0 . Permeability results for two preforms used by Masur (Masur, Mortensen et al. 1989) are also shown in the diagram.

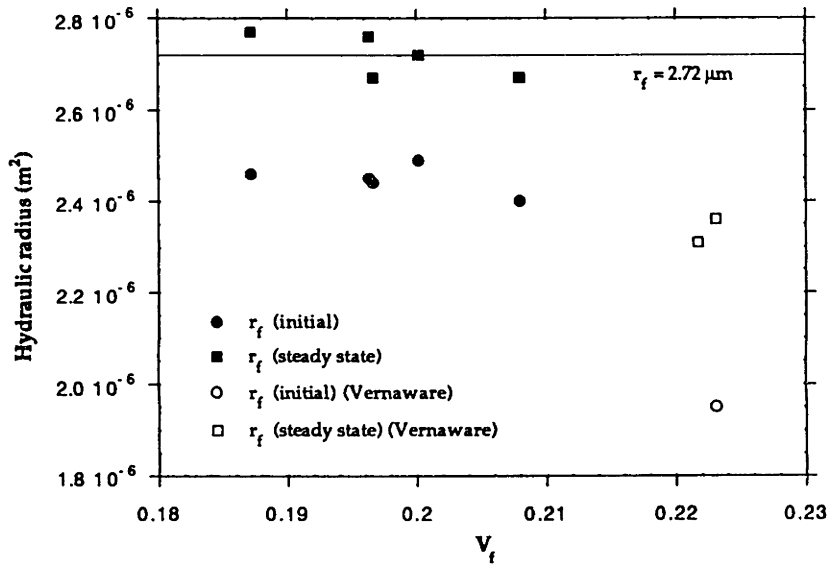


Figure (5.17) - Initial and steady-state hydraulic radii vs. V_f^0 . Hydraulic radii for preforms used in Masur (Masur, Mortensen et al. 1989) are also shown in the diagram.

VI - DISCUSSION

A - INFILTRATION OF POLYURETHANE FOAM

1 - Assumptions of the model

a. Darcy's Law

For Darcy's Law to be valid, the Reynolds number Re defined by:

$$Re = \frac{d \rho v_l}{\mu} \quad (6.1)$$

should be lower than a value of order 1 (Mortensen, Masur et al. 1989). In these present experiments, the liquid velocity varies with time, and is maximum at the infiltration front. The pore velocity at the infiltration front in relation to the solid at $t = 23$ s was measured to be $8.71 \cdot 10^{-4} \text{ m} \cdot \text{s}^{-1}$. This is the highest liquid velocity measured after the sponge reaches pseudo-steady state, whereby its volume fraction depends only on fractional distances along its length.

The foam cell diameter, originally $450 \mu\text{m}$ perpendicular to the rise direction, shrinks in size at the infiltration front due to the hydrostatic pressure according to the following equation:

$$d = d_0 \left(\frac{1 - V_f}{1 - V_f^0} \right)^{1/3} \quad (6.2)$$

where d_0 is the original cell diameter of the relaxed sponge, V_f^0 is the original sponge volume fraction, and d represents the new cell diameter

when the volume fraction equals V_f . Therefore, an overestimate of Re anywhere in the sponge at $t = 23$ s is obtained by taking $d = 450$ μm . Knowing that the liquid pore velocity at the infiltration front relative to the solid phase at 23 seconds was $8.71 \cdot 10^{-4}$ $\text{m} \cdot \text{s}^{-1}$, and the viscosity and density of ethylene glycol are $15.7 \cdot 10^{-3}$ $\text{Pa} \cdot \text{s}$ and 1.109 $\text{g} \cdot \text{cm}^{-3}$, respectively, the resulting Reynolds number equals $2.5 \cdot 10^{-2}$. This is a conservative estimate, in that (i) under hydrostatic pressure the foam cell size actually varies between 450 μm perpendicular to the rise direction to 70 μm at the interconnecting pore between cells, (ii) the cell walls may collapse and lower the sponge cell diameter, and (iii) at later times, the liquid velocity drops considerably.

The influence of gravity is negligible during the infiltration experiment: the maximum infiltration distance measured vertically was 9.8 cm, which corresponds to a pressure drop of 1,066 Pa (0.155 psi), i.e., a 1.1% error, considering that the pressure drop across the sponge during infiltration was 99500 Pa (14.44 psi).

b. Wetting and permeability

The first drainage curve of the dry uncompressed sponge was measured to determine the degree of saturation with applied pressure. It was found there was no spontaneous infiltration, and that when the applied pressure is 14,200 Pa (0.14 atm), the liquid fills approximately 89% of the pore space. Therefore, only a small, positive pressure is required to saturate the sponge with the liquid, reflecting a ΔP_γ at the infiltration front significantly lower than the applied pressure of one atmosphere. According to Mortensen (Mortensen and Wong 1990), ΔP_γ is roughly proportional to S_f , the surface area of solid per unit volume of liquid.

Assuming that surface area of the sponge in the relaxed state is the same as in the compressed state, ΔP_γ should increase by a factor of $(1 - V_f^0)/(1 - V_f) \approx 1.3$, when total atmospheric pressure is applied on the sponge. We have assumed, therefore, in our calculations that the capillary pressure for full infiltration of the sponge under slug flow, ΔP_γ , is negligibly small.

As the applied pressure varies, the saturation changes little. Knowing that small deviations from full saturation exert only a small influence on relative permeability of a porous medium with a non-wetting fluid (Dullien 1979; Anderson 1987) pp. 257-283 (Morel-Seytoux 1969), variations in the permeability K of the sponge with applied pressure are mostly due to variations in V_f .

The equation found by Barry (Barry and Aldis 1990) for permeability of a polyurethane sponge from data of Parker (Parker, Mehta et al. 1987) for unidirectional steady-state flow of liquid did not fit the permeability data as well as Equation (5.2), and so was not used.

c. Experimental error in V_f and χ

V_f was measured using the width of the sponge rather than the separation of lines drawn on the sponge because of the lower error in measuring larger distances on a screen with finite pixel width. The largest error in V_f was at the infiltration front, and is estimated in Appendix (5.2-E) to be $\frac{\Delta V_f}{V_f} \approx 0.04$.

The error in measuring χ , the fractional length along the infiltrated sponge, results mostly from the curvature of the lines drawn on the sponge in highly distorted regions, located between $\chi = 0.65$ and $\chi = 0.85$. The largest error occurs when L , χ , and infiltration times are relatively

small. At $t = 23$ seconds and $\chi = 0.68$, a maximum error of $\frac{\Delta\chi}{\chi} \approx 0.04$ is calculated, Appendix (5.2-F).

d. Effects of air evacuation and viscoelasticity

In the hydrostatic pressure experiment, Figure (5.1), the sponge was fully evacuated and allowed to expand slowly under decreasing hydrostatic pressures in an experiment that lasted over 50 minutes. The results from this test were used to determine the V_f measured on the video recording and the required sponge dimensions for permeability measurements. As infiltration of the sponge only lasted approximately one minute, some error is introduced due to incomplete relaxation of the sponge during infiltration compared to data in the curve of Figure 5.1.

Curves of V_f vs. P and V_f vs. t for fixed P (Figures 5.1 and 5.2a,b) were recorded with the same sponge used in infiltration attached to an additional buffer sponge. Therefore, viscoelasticity effects are the same as in infiltration, but air evacuation is somewhat slower. It is seen in Figure 5.2b that, after 20 seconds, further relaxation of the sponge to $t = 40$ minutes only induces an additional change in V_f on the order of $\Delta V_f = 0.027$. After 60 seconds, the change is even less with $\Delta V_f = 0.015$, or $\frac{\Delta V_f}{V_f} = 0.045$. The total error in volume fraction then becomes about 0.09.

e. Effect of evaporation at the infiltration front

Boiling of the ethylene glycol infiltrant may have occurred at the infiltration front due to the vacuum, though it was not discernable at the liquid-vacuum interface during the actual infiltration. As the liquid evaporates at the infiltration front, heat absorbed and the temperature of

the infiltrated composite will drop. This, in turn, raises the viscosity of the liquid and lowers the infiltration rate.

Assume for simplicity that the polyurethane sponge is adiabatically infiltrated, without expanding laterally, and that no temperature gradient exists within the infiltrated portion of length L . The final average temperature, T_{ave} , within the composite can be estimated by balancing the heat exchanged by the composite during infiltration, and the heat absorbed by evaporation by the following equation:

$$L (T_{ave} - T_0) \left(C_p^l \rho_l (1 - V_f) + C_p^s \rho_s (V_f) \right) = J_{ev} \Delta H_v (1 - V_f) t \quad (6.4)$$

where C_p^l and C_p^s are the heat capacities of the liquid and the solid, T_0 is the initial temperature, and ΔH_v is the heat of vaporization of the liquid. J_{ev} is the molar evaporation flux from the infiltration front.

Experimentally, the ethylene glycol infiltrates the sponge to a distance of 9.8 cm in 67 seconds. At 26°C, the vapor pressure of ethylene glycol is approximately 15 Pa (0.002 psi) (Weast, p. D-487). The maximum flux of molecules, J_{ev} , evaporating from the ethylene glycol liquid surface can be estimated by using kinetic gas theory (Satterfield 1970). Assuming the average radius of the pore diameter in the sponge to be 130 μm and the tortuosity of the sponge matrix to be about 4, the Knudsen diffusion coefficient, D_K , is estimated to be 45.8 $\text{cm}^2 \cdot \text{s}^{-1}$. The binary gas diffusion coefficient, D_B , of ethylene glycol diffusing in air is estimated to be approximately 8.3 $\text{cm}^2 \cdot \text{s}^{-1}$, assuming the pressure of the air in the sponge and vacuum reservoir to be at most 200 Pa.

Using the infiltration front as the reference frame, the distance that the vapor travels ahead of the liquid can be approximated by the quantity \sqrt{Dt} . Experimentally, the average distance from the infiltration front to the end of the sponge during $t = 23 - 67$ s was approximately 8.2 cm. By using either diffusion coefficient, the calculated time for the ethylene glycol vapor to reach the end of the sponge is calculated to be less than 9 s. It is, therefore, safe to conclude that the concentration gradient of the ethylene glycol in the uninfiltred region of the sponge is approximately constant.

Since neither type of diffusion coefficient strongly predominates, the evaporation kinetics are within the transitional region. As an upper bound estimation, if it is assumed that Knudsen diffusion is rate controlling, that the exiting air moves at the same velocity as the infiltration front, and that the concentration of the ethylene glycol vapor at the end of the sponge zero, the molecular flux from the ethylene glycol infiltration front can be estimated by the following equation:

$$J_{ev} = \frac{-D_K p_{eg}}{RT x}, \quad (6.5)$$

With the average sponge distance ahead of the infiltration, x , approximately equal to 8 cm, J_{ev} is estimated to be $4 \cdot 10^{-8} \text{ mol} \cdot \text{cm}^{-2} \cdot \text{s}^{-1}$. This molecular evaporation flux causes a temperature drop at the infiltration front approximately -0.01 K, which does not influence the infiltration kinetics noticeably. Experimentally, the value of ψ^2 was actually higher than the theoretical value.

f. Influence of the fluid on mechanical properties of the sponge

Beavers (Beavers, Wittenberg et al. 1981) noticed that water-submerged sponges would strain to a further degree under a given applied stress than when in the dry state. This was attributed to liquid lubrication effects that may have occurred within the internal structure of the wet sponge during compression. Since all mechanical testing on the sponge was done in the dry state (to prevent complications in the results induced by flow of the liquid), some added experimental error in the mechanical relaxation properties of the sponge may result from this effect.

2 - Comparison of theory with experiment

Experimental data indicate that after about 17 s, plots of L^2 , x_f^2 , and x_e^2 versus t , Figures 5.5, 6.1a, and 6.1b become linear, in agreement with theory and data which show that time dependence in the mechanical behavior of the sponge, induced by viscoelasticity and air evacuation, becomes negligible after at most 20 s.

The resulting ψ^2 was measured to be $1.2 \cdot 10^{-4} \text{ m}^2 \cdot \text{sec}^{-1}$ while theory predicts $9.1 \cdot 10^{-5} \text{ m}^2 \cdot \text{sec}^{-1}$. At the infiltration front, l was measured to be 0.481 while the theoretical value obtained was 0.401. Experimental error in the measured value of ψ^2 is 10% (Appendix (5.2-D)). The uncertainty in the predicted value of ψ^2 is roughly proportional to the uncertainty in the permeability, K . The uncertainty in K that arises from experimental error in the correlation between K and V_f is on the order of $\Delta K/K \approx 12\%$ (Appendix (5.2-B)). The experimental error in the measurement of V_f , $\Delta V_f/V_f \approx 4\%$ induces additional uncertainty in the predicted permeability

on the order of 60%. The predicted rate of infiltration, measured by ψ^2 , is therefore well within experimental error of the measured value.

By extrapolation of the curve of L^2 versus t to $L = 0$, we can define $t = t_{ss} = -13.7$ s, the time at which at which infiltration should have begun were all assumptions of the theory obeyed from the beginning of infiltration (similar extrapolations of x_L and x_s yield somewhat different values of t_{ss} , in part because of greater experimental error compared to L , induced by uncertainty in the location of $x = 0$). Knowing t_{ss} , experimental values of l and s , defined in Equations (3.14) and (3.15), can then be calculated using the following equations:

$$l(\chi) = \frac{x_l(\chi)}{2\sqrt{\psi^2(t-t_{ss})}} \quad (6.6)$$

$$s(\chi) = \frac{x_s(\chi)}{2\sqrt{\psi^2(t-t_{ss})}} \quad (6.7)$$

A plot of $l(\chi=1) - s(\chi=0)$ is given in Figure (6.2). It is seen that after about 20 s, $l(\chi=1) - s(\chi=0)$ equals 0.5, in agreement with theory, Equation (3.26). The computed values of $l(\chi=1)$ and $s(\chi=0)$ are 0.401 and -0.099, respectively, while the experimental values are 0.480 and -0.020, respectively.

Figure 6.3 shows the volume fraction along the infiltrated sample at different times, as compared with theory. For $t > 20$ s, the curve is invariant in time, in agreement with theory. For $t < 20$ s, the curve is shifted somewhat to the left of the pseudo steady-state value, as expected for incomplete relaxation of the sponge due to its visco-elastic behavior. Comparison between predicted and measured pseudo steady-state curves

of V_f versus χ is very satisfactory. In particular, agreement of V_f at the infiltration front with theory legitimizes the assumption made earlier that $\Delta P_\gamma \approx 0$.

The predicted curve of local permeability, K , as a function of χ during infiltration is shown in Figure 6.4a. K tends to drop off precipitously at higher V_f , near the infiltration front. This region therefore constitutes a "bottleneck" to infiltration, and dominates the kinetics of the process.

Predicted curves of l and s as a function of χ are shown in Figures 6.4b and 6.4c. l increases with increasing V_f . At the infiltration front, the velocity of the sponge is zero because we have assumed $\Delta P_\gamma \approx 0$. Behind the infiltration front, s increases to -0.099 at the mouth of the sponge. Between $\chi = 0$ and 0.6 , s remains roughly constant because V_f is roughly constant, near the V_f corresponding to the fully relaxed state (Figure 6.3).

B - INFILTRATION OF ALUMINA FIBER PREFORMS BY ALUMINUM

1 - Validation of Darcy's Law

The velocities of the infiltrating liquid aluminum in the preform in regions where ψ^2 were calculated were on the order of $1 \text{ cm}\cdot\text{s}^{-1}$. For $T_f = 100^\circ\text{C}$ and $V_f = 0.19$, the corresponding $r_{sf} \approx 5 \mu\text{m}$. The calculated Reynolds number is then $Re \approx 0.185$, which is below the critical value of 1 for validity of Darcy's law. When compression occurs, the liquid velocity drops considerably lower, due to the lower K in the compressed fiber region. The Reynolds number in this case is significantly lower. In all cases, therefore, Darcy's law is valid.

2 - Incidence of preform compression

Stress-strain curves of the fiber preforms show that significant permanent deformation of the preforms takes place for compressive stresses exceeding about 2 MPa (Figure 5.14), this value being strongly dependent upon the initial volume fraction V_f^0 . Irreversible deformation of the preforms is most likely caused by fiber and binder breakage, a process that has been modeled by Clyne and Mason (Clyne and Mason 1987). Since none of these likely preform deformation mechanisms (elastic deformation, fiber breakage, and fiber rearrangement) are time-dependent, data from mechanical tests should remain applicable to preform deformation during infiltration, despite the much higher strain rates experienced by the preforms during infiltration. Because of this irreversible deformation, Saffil™ preforms infiltrated along one direction with no wall friction or external cooling should be shortened in the solidified composite if the applied pressure exceeds about 2 MPa.

It is seen in Table 5.2 that for several samples, the applied pressure ΔP_T exceeded 2 MPa significantly, yet no significant deformation of the central portion of the preforms was found in the final infiltrated composites. This may therefore be a consequence of friction along their boundary with the Grafoil™ insert.

If we assume that the shear stress along the Grafoil™/composite interface must exceed a critical shear stress τ_s , for the infiltrated preform to slide along the Grafoil™ insert, Equation (3.48) must be satisfied for preform compression to occur. This is tested in Figure 6.5, where the

maximum value of dP/dx in region 1 of composites is plotted on the vertical axis. These values were computed using the left-hand side of Equation (3.48), using measured values of χ_s for infiltrated samples with a superheated matrix. The samples are sorted into two columns, according to whether preform compression occurred or not. It is seen that preform compression consistently occurred when dP/dx exceeded $116 \text{ MPa} \cdot \text{m}^{-1}$, showing that Eq. (3.48) provides a valid criterion for preform deformation with $\tau_s = 0.33 \text{ MPa}$.

Closer examination of plots of dP/dx , L^2 , and ΔP_T versus time provide further confirmation of the validity of this criterion for preform compression. Such plots are given in Figure 6.6 for a typical sample (Sample K). It is seen that when dP/dx reaches the critical value of $116 \text{ MPa} \cdot \text{m}^{-1}$, the slope of L^2 versus time decreases suddenly, suggesting that preform compression has just taken place. The requirement for a critical value of dP/dx to be exceeded for preform deformation to occur also explains why preform delamination was observed in Samples H, K, and M. Within region 1, the permeability is much lower than in the remelted zone, region 3. Therefore, according to Darcy's law, dP/dx was far greater in region 1 than in region 3. When dP/dx exceeded the critical value in region 1, therefore, that portion of the preform underwent compression while region 3 was still held in place by the wall friction, since dP/dx was locally lower than the critical value. If the preform tensile strength was insufficient to pull the preform in region 3 when region 1 moved forward, preform delamination could occur, as shown in Figures 5.7 and 5.9. This explanation was confirmed by comparing the location of the tear with the predicted location of the remelting front, χ_s , at the time when dP/dx reached the critical value in region 1 of the composite (2.0 mm

measured versus 2.5 mm calculated for Sample K, 4.5 mm measured versus 5.1 mm calculated for Sample M).

The value $\tau_s = 0.33$ MPa is specific to the Grafoil™/composite interface in these composite samples, and has no general applicability. It is interesting to note that this value is far higher than the friction shear stress between Grafoil™ inserts and uninfiltated preforms in compression experiments, which implies that metal solidification along the Grafoil™ must have played a role in the observed value of τ_s .

In all samples, the outer ring remained at its original position, indicating that it underwent no deformation during infiltration. Previous experiments with Saffil™ preforms having V_f^0 as low as 10% and no Grafoil™ inserts have shown that no preform deformation is observed (Mortensen and Wong 1990), even if ΔP_T far exceeds the threshold pressure for preform plastic deformation. These data imply that along the fused quartz tube, τ_s is much higher than along the Grafoil™ insert. This may be due to the greater thermal mass of the fused quartz tube, which induces matrix solidification in its vicinity, and to preform “sticking” to the tube wall by chemical reaction of the composite with the fused quartz tube.

When necessary conditions for preform deformation are fulfilled, the fiber volume fraction at any location x along the composite is at most equal to V_f^c , corresponding to the applied pressure ΔP_T at the moment when the infiltration front reached x . Plots of experimentally measured values of V_f versus distance from the final infiltration front position along the SiC monofilament are compared with V_f^c (full line) for Samples I, J and K in Figures 5.10, 5.11, and 5.12. It is seen that within

experimental error, measured values of V_f fall close to V_f^c . On this figure, V_f^r (dash-dot line) corresponding to full relaxation of the preforms is plotted (neglecting preform motion due to relaxation). It is seen that experimental values of V_f far exceed V_f^r . Two factors may be invoked to explain the absence of full preform relaxation: (i) wall friction, and (ii) preform stiffening due to solid metal formed at the infiltration front in contact with the cold fibers.

After infiltration, friction at the die wall will leave a residual compressive stress in the preform equal to:

$$\sigma_{(x)} = \frac{2\tau_s}{R_i} \cdot x \quad (6.8)$$

where x is distance from the preform entrance. Plots of V_f versus distance from the final infiltration front, corresponding to compression of the preforms to ΔP_T followed by relaxation to $\sigma_{(x)}$, are also included as dashed lines in Figs. 5.10 to 5.12. It is seen that friction along the preform/Grafoil™ interface can account for the lack of preform relaxation. This does not imply, however, that the solid metal within region 1 of the composite does not also prevent preform relaxation: observations of fiber volume fraction distributions in composites of Saffil™ fiber preforms infiltrated with Al-4.5 wt pct Cu have shown that solid metal in region 1 prevents relaxation of the preforms in that system (Jarry, Dubus et al. 1990).

In conclusion, wall friction effects are very significant. They influence significantly the occurrence of deformation, introducing a second necessary condition in addition to the need for pressure to be high, and they also influence preform relaxation when compression occurs. They provide one mechanism for the creation of preform tears, observed

by several researchers in infiltrated metal-matrix composites (e.g., (Clyne and Mason 1987; Masur, Mortensen et al. 1989)). From a practical standpoint, this conclusion also implies that friction and matrix solidification along the mold/preform interface can be used to prevent preform compression in infiltration processing of metal-matrix composites.

3 - Kinetics of infiltration

Two bounds were given for the kinetics of non-isothermal adiabatic infiltration with no wall friction: cases (i) and (ii) of Section III - B -1. Theoretical values of ψ^2 are plotted in Figs. 6.7, 6.8, and 6.9 for Saffil™ preforms infiltrated by aluminum with plausible values of infiltration parameters for these two bounds. The program for aluminum infiltration into Saffil™ preforms is listed in Appendix (3.2). ΔP_γ for a given V_f was estimated by Equation (3) in Reference (Mortensen and Wong 1990) for the program. It is seen that these two bounds are close, especially if it is kept in mind that permeabilities and infiltration rates are seldom predicted with a precision better than within a factor of about 2. The closeness of these bounds implies that the much simpler lower bound (case (ii)) can be used to predict with adequate precision the kinetics of infiltration of these composites when preform compression occurs.

The lower limits of the bell shape of curves in Figures 6.7 and 6.8 are due to the fact that no infiltration occurs when ΔP_T is lower than the capillary pressure ΔP_γ . The upper limits are reached when ΔP_T produces sufficient deformation of the preforms for $V_f^f + V_s$ (V_s is given in Eq.

(3.38)) to completely block the liquid flow at the infiltration front (corresponding to $K \approx 0$). This is qualitatively shown with the added effect of wall friction in the sequence of Samples L, I, and J, which were infiltrated at increasing ΔP_T with all other parameters constant (Figure 6.10). Sample L was infiltrated to a longer distance, even though the ΔP_T values of the other two specimens were much higher. No ψ value was obtained in sample J due to complete flow blockage after compression occurred.

Experimental values of ψ are compared with theory in Table 6.1. Two calculated values are given for ψ . The first is calculated assuming no preform compression for $V_f = V_f^0$ according to theory of reference (Mortensen, Masur et al. 1989). The second value of ψ is calculated assuming preform compression according to case (ii) of section III-B-1, neglecting for simplicity the influence of superheat (i.e., assuming $T_o = T_m$).

Experimental data are compared with theory assuming no preform compression in Figure 6.11. It is seen that, for samples where no preform compression occurred, experimental values of ψ equal or exceed the theoretical values of ψ by twice that value. This result is analogous to that found in previous studies of infiltration of non-deforming Saffil™ preforms by pure aluminum (Masur, Mortensen et al. 1989; Mortensen and Wong 1990). In a review of permeability by Jackson (Jackson and James 1986), it was noted that permeability is a strong function of fiber orientation and structure. For a given fiber orientation, the scatter in permeability can very easily reach a factor of two for a given fiber volume fraction. When preform compression occurs, measured values of ψ

equal, or are inferior to, predicted values assuming no preform compression. Comparison of experimental values of ψ with theory taking preform compression into account, Figure 6.12, shows that experimental values of ψ equal or exceed the theoretical values by a factor of about 2. This trend is also seen in the experimental data and theory when no preform compression occurs.

In conclusion, the two theoretical bounds derived above for the rate of unidirectional adiabatic non-isothermal infiltration in Section III-B-1 are close in the case of Saffil™ preforms infiltration by aluminum. The lower bound, case (ii), therefore provides a reasonably simple theoretical prediction of the rate of infiltration when preform compression occurs. This lower bound agrees with experimental infiltration rates within the same margin of error as does theory with experiment for infiltration with no preform compression.

Table 6.1 - Comparison of experimental and theoretical infiltration rates.

Exp #	χ_s measured	χ_s theory	ψ experiment ($m \cdot s^{-1/2}$) ($\cdot 10^{-2}$)	ψ theory, no compression ($m \cdot s^{-1/2}$) ($\cdot 10^{-2}$)	ψ full compression, no relaxation, no remelting ($m \cdot s^{-1/2}$) ($\cdot 10^{-2}$)	Corn-pressed
A	-	-	1.5	0.94	-	N
B	-	-	1.6	0.96	-	N
C	-	-	0.61	0.74	0.30	Y
D	-	-	0.84	0.84	0.41	Y
E	-	-	0.62	0.51	0	Y
F	-	-	1.1	0.44	-	N
G	-	-	3.1	2.3	-	N
H	0.40	0.54	0.98	0.79	0.79	Y
I	0.59	0.39	0.57	1.2	0.53	Y
J	0.54	0.27	0	1.8	0	Y
K	0.27	0.31	1.1	1.8	0.70	Y
L	0.22	0.52	0.73	0.87	-	N
M	0.32	0.46	2.0	1.9	0.82	Y

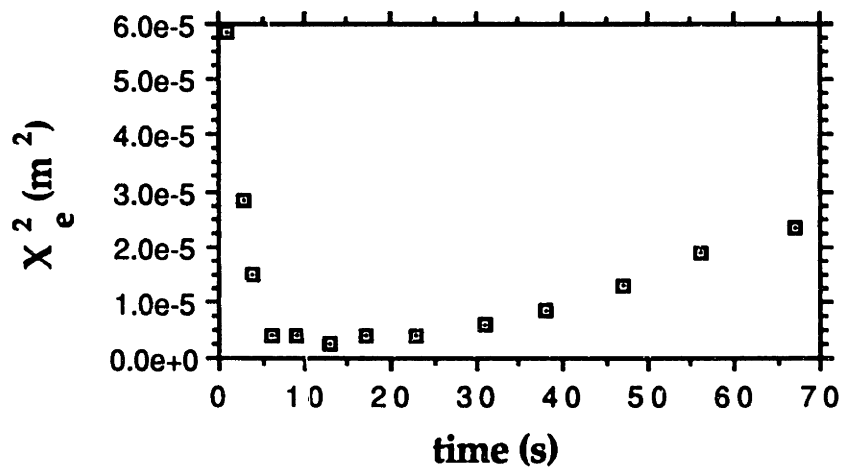
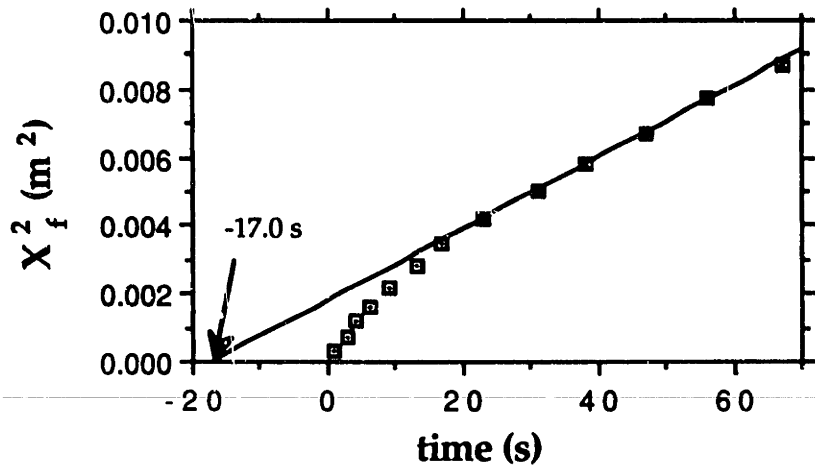


Figure (6.1) - see Figure (3.4) for definitions.

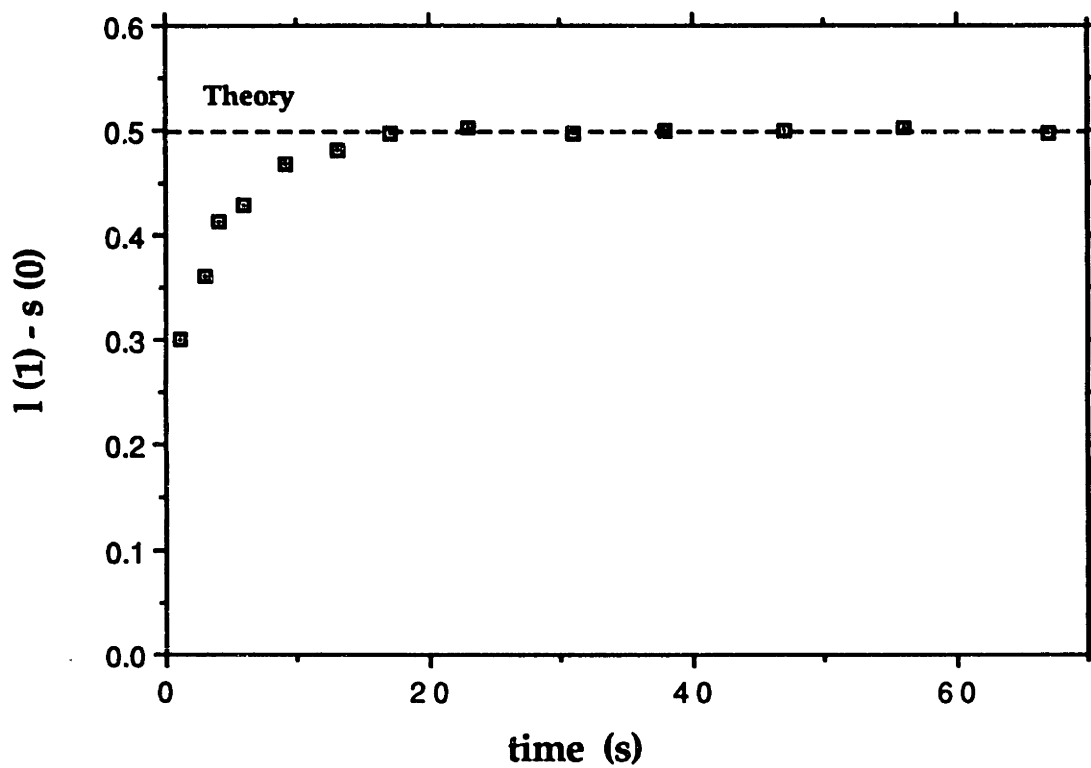


Figure (6.2) - Plot of $l(\chi=1) - s(\chi=0)$ vs. time. Steady state is reached at approximately 20 s.

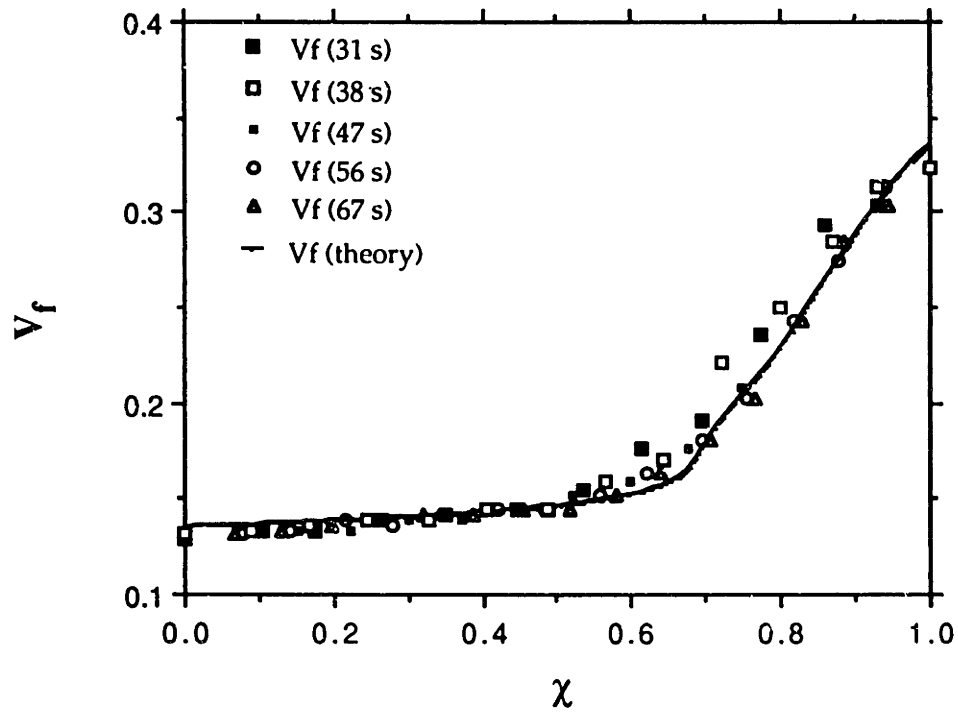


Figure (6.3) - Experimental V_f distribution along infiltrated length of sponge at various times as compared with theoretical predictions.

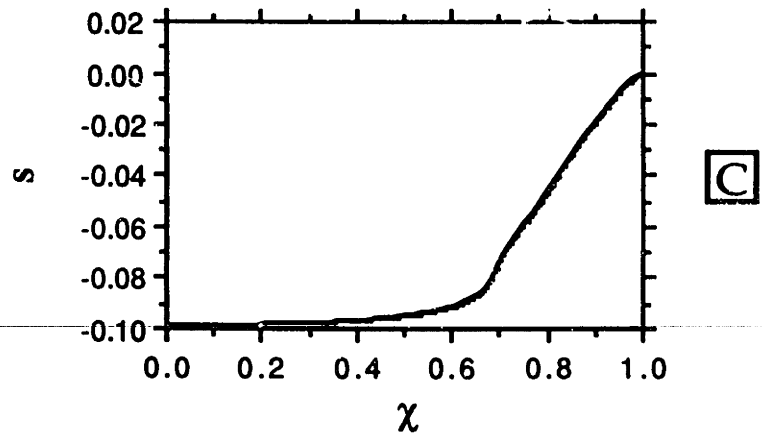
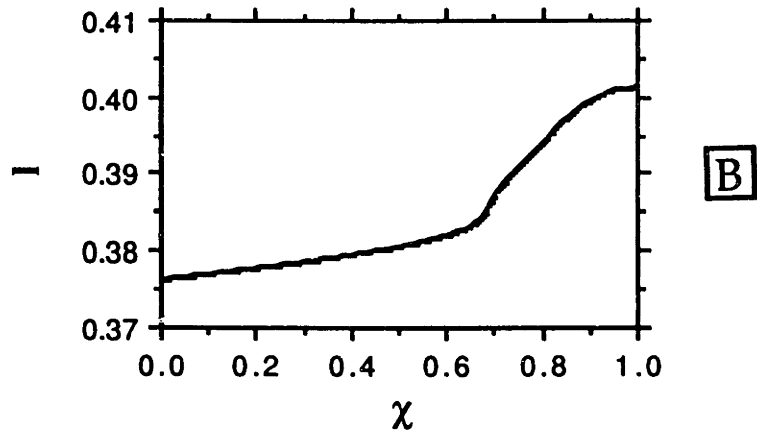
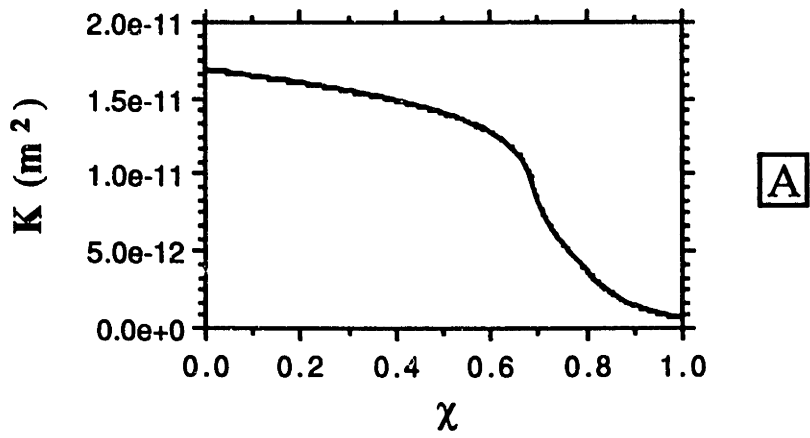


Figure (6.4) - Theoretical predictions along infiltrated length for: (a) K , (b) l , and (c) s

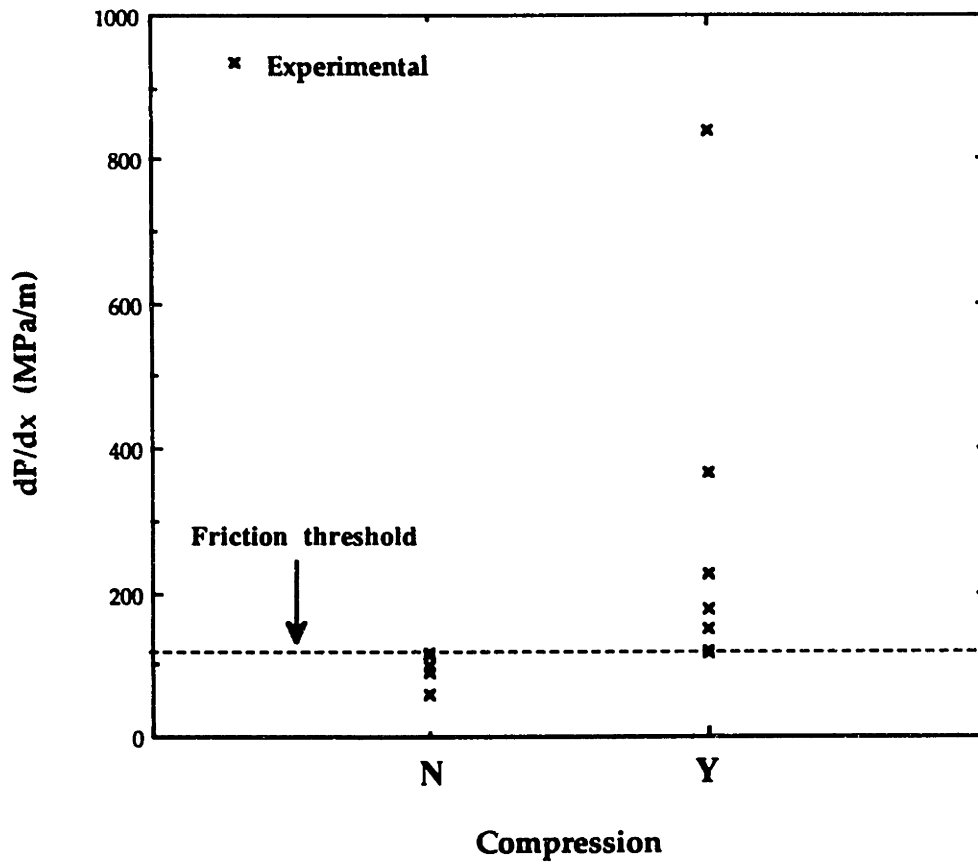


Figure (6.5) - Plot of maximum value of dP/dx vs. experimental compression results. "N" and "Y" correspond to "no compression" and "compression," respectively. Compression occurs when dP/dx exceeds $116 \text{ MPa} \cdot \text{m}^{-1}$.

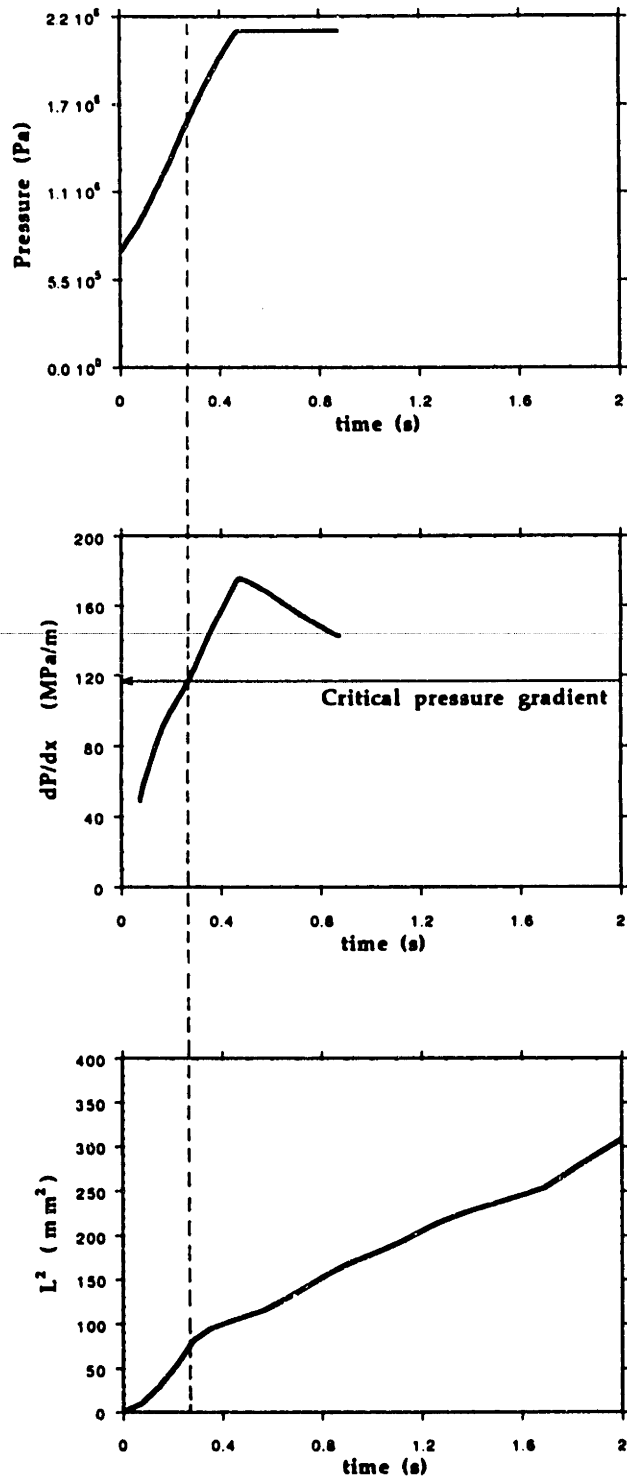


Figure (6.6) - Pressure, dP/dx , and L^2 as a function of time for sample K. At $dP/dx = 116 \text{ MPa} \cdot \text{m}^{-1}$, the slope of L^2 vs t suddenly decreases, indicating preform compression.

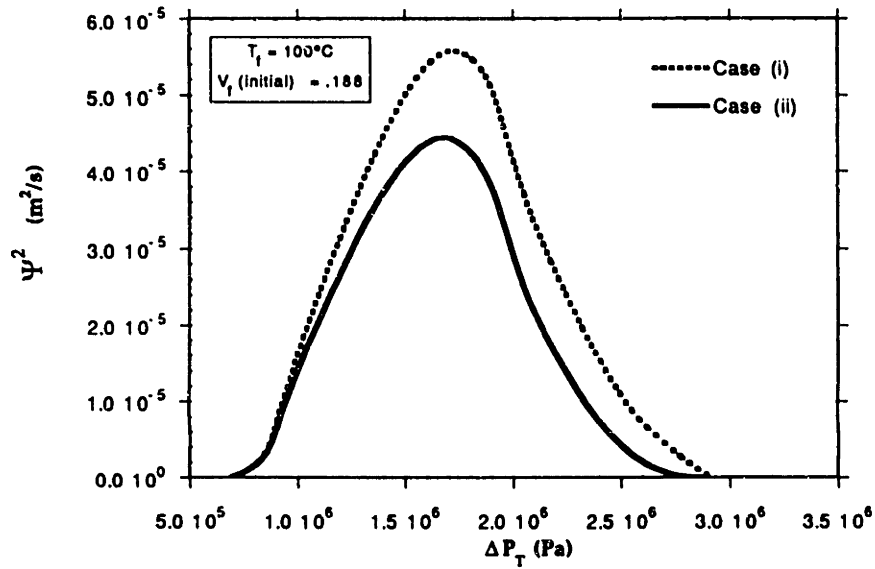


Figure (6.7) - Theoretical values of ψ^2 vs. ΔP_T at $T_f = 100^\circ\text{C}$ and $V_f^0 = 0.188$, assuming non-isothermal adiabatic infiltration and no wall friction.

Case i): The solid metal surrounding the fibers leaves the mechanical properties of the preform unaffected.

Case ii): The solid metal retains the fibers at V_f corresponding to $P = \Delta P_T - \Delta P_\gamma$.

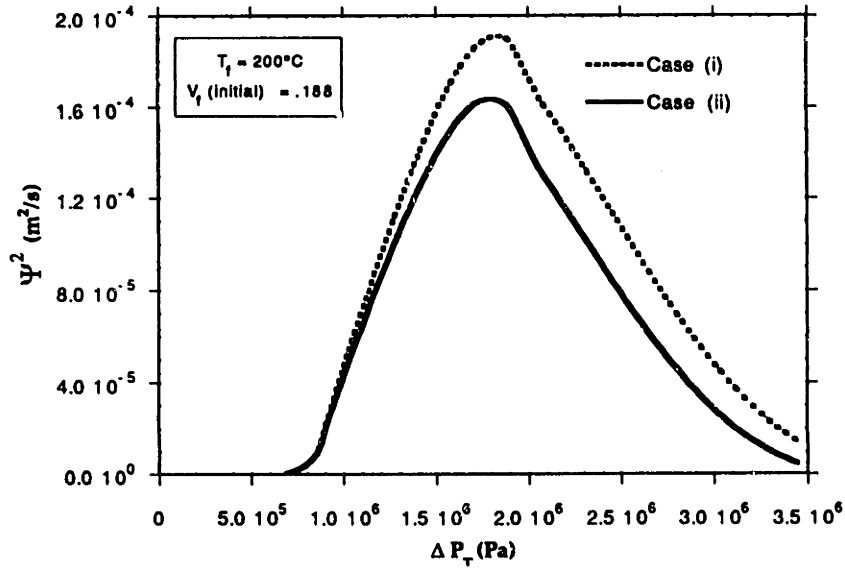


Figure (6.8) - Theoretical values of ψ^2 vs. ΔP_T at $T_f = 200^\circ\text{C}$ and $V_f^0 = 0.188$, assuming non-isothermal adiabatic infiltration and no wall friction.

Case i): The solid metal surrounding the fibers leaves the mechanical properties of the preform unaffected.

Case ii): The solid metal retains the fibers at V_f corresponding to $P = \Delta P_T - \Delta P_\gamma$.

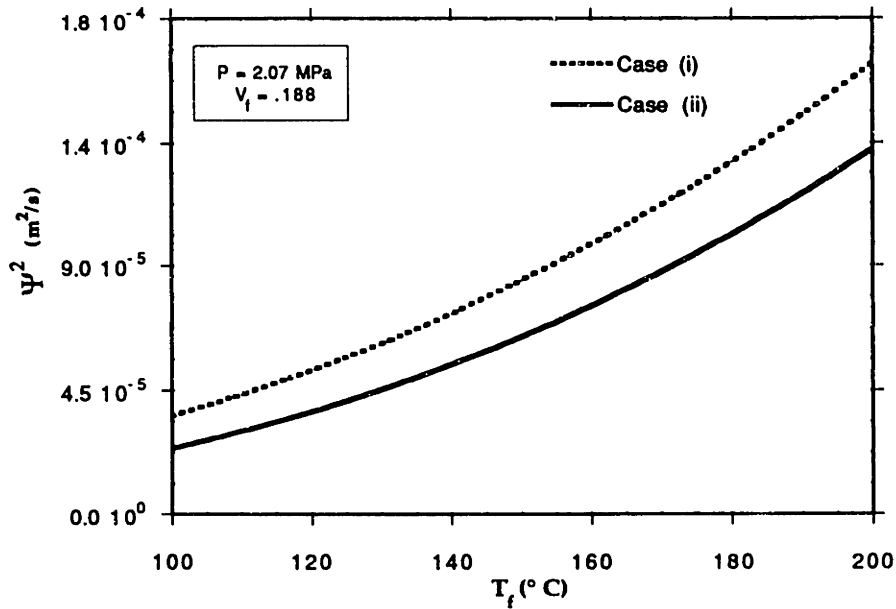


Figure (6.9) - Theoretical values of ψ^2 vs. T_f for $\Delta P_T = 2.07 \text{ MPa}$ and $V_f^0 = 0.188$, assuming non-isothermal adiabatic infiltration and no wall friction.

Case i): The solid metal surrounding the fibers leaves the mechanical properties of the preform unaffected.

Case ii): The solid metal retains the fibers in the compressed V_f corresponding to $P = \Delta P_T - \Delta P_\gamma$.

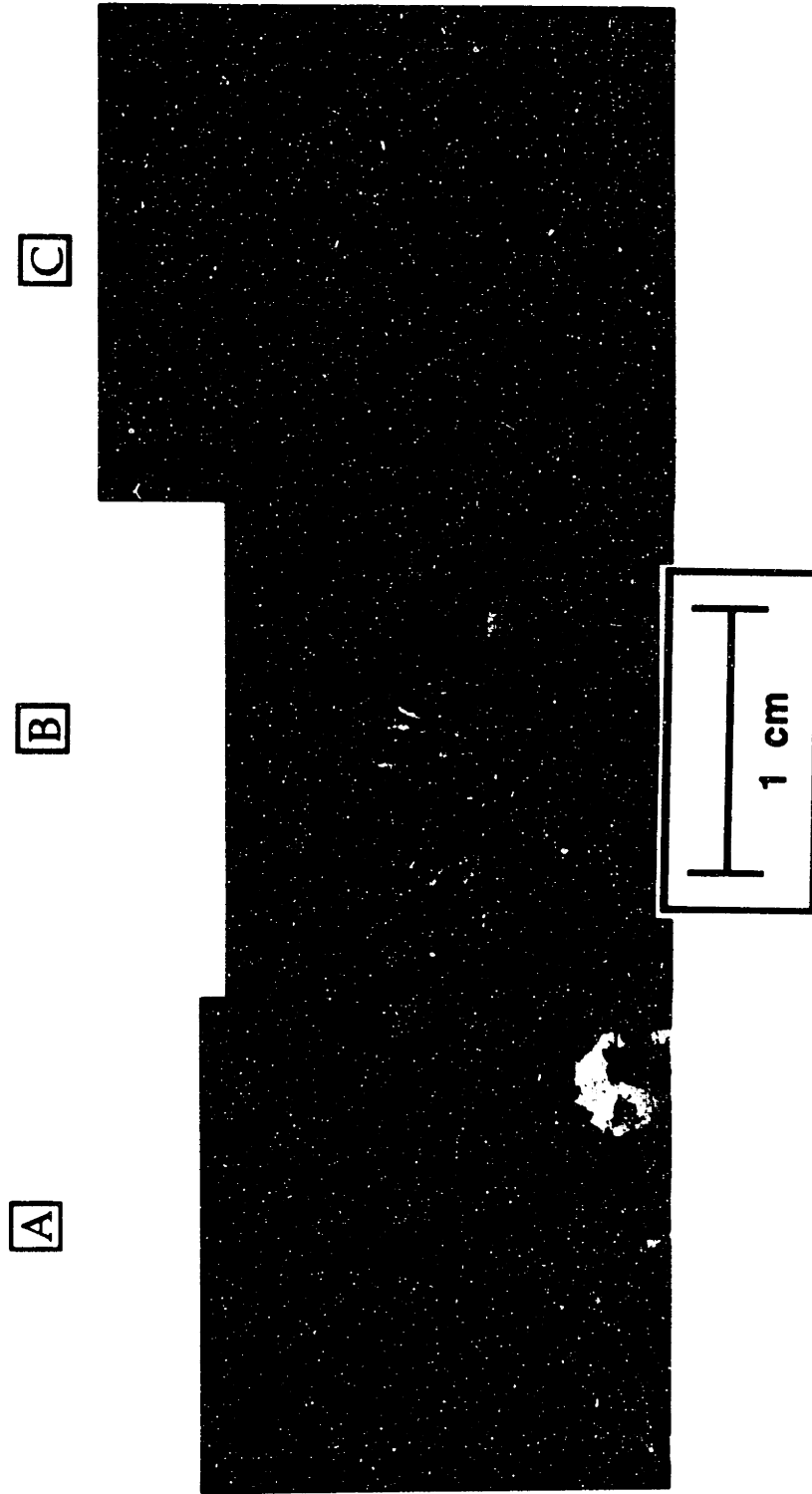


Figure (6.10) - Micrographs showing compression distances and infiltration lengths of etched samples:
(a) Sample L ($\Delta P_T = 1.45$ MPa), (b) Sample I ($\Delta P_T = 2.12$ MPa), and
(c) Sample J ($\Delta P_T = 3.69$ MPa). $T_f = 100^\circ\text{C}$ for all samples.

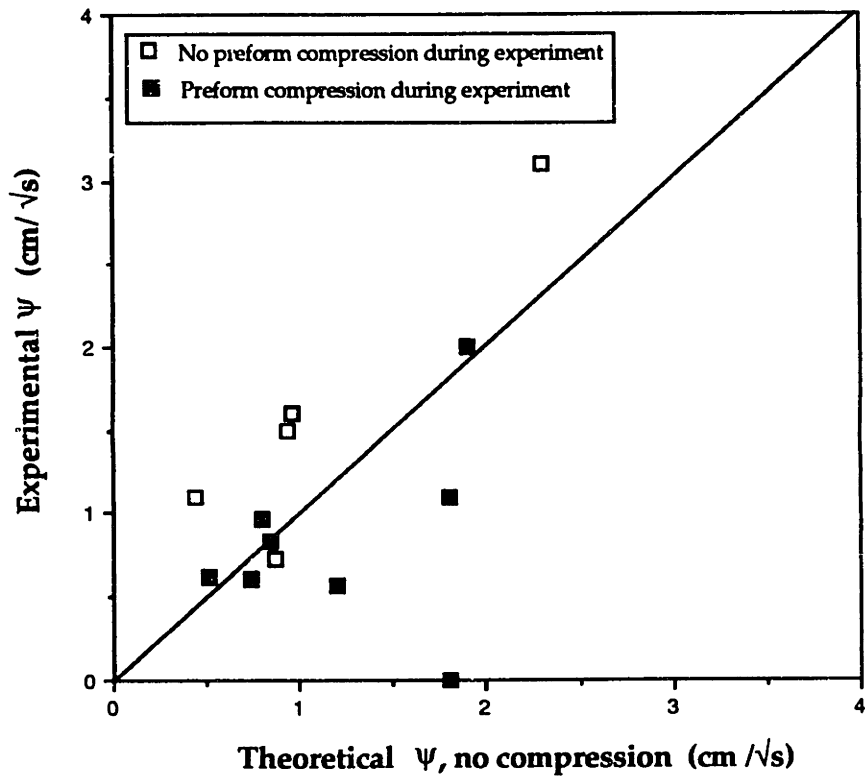


Figure (6.11) - Comparison of experimental data with theory, assuming no preform compression.

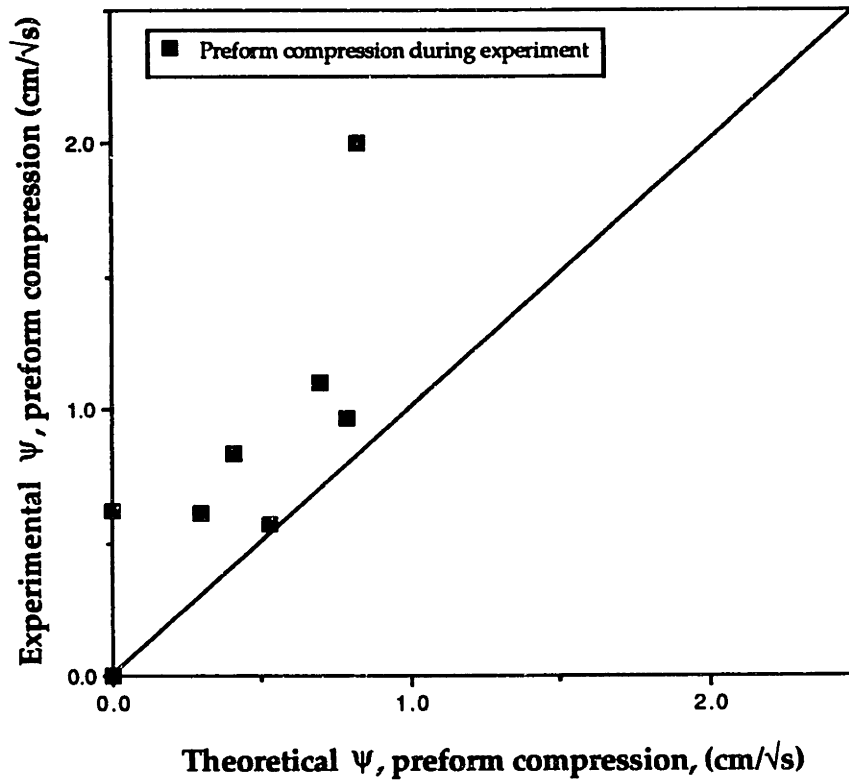


Figure (6.12) - Comparison of experimental values of ψ with theory, assuming compression with no relaxation, according to case (ii) of Section III-B-1.

VI - CONCLUSIONS

- A theoretical model is developed to predict the infiltration kinetics and volume fraction distributions during isothermal infiltration of a deformable porous medium, which can be solved using the Boltzmann transformation when a constant pressure differential drives the liquid flow. It is found that the coupling of fluid flow with porous medium deformation can cause nonuniform strain distributions in the infiltrated matrix and can substantially influence the rate of liquid infiltration.

- The model is verified by analyzing the hydrostatic infiltration of a polyurethane sponge with ethylene glycol.

- The infiltration theory is modified to take into account the effect of solidification for adiabatic infiltration by a pure metal. Two bounds describing the infiltration rate are presented:

Case (i) - the solidified metal contributes no mechanical strength to the fibers (upper bound).

Case (ii) - the preform is held in its compressed state by the solidified metal (lower bound).

- Wall friction and matrix solidification along the composite/mold wall interface can exert a significant influence on preform compression and relaxation and can be utilized to prevent preform compression during infiltration.

- Experimental results on pure aluminum infiltration of Saffil™ preforms agree with theory and suggest that the infiltration kinetics are reasonably well predicted by assuming that no fiber relaxation takes place, i.e., case (ii) above.

Suggestions for future work

- Additional verification of the adiabatic infiltration theory could be done by infiltrating hydrostatically an open-celled polyurethane foam which is held initially at a temperature below the melting point of the infiltrating liquid. This would allow us to study the compression response of the porous medium with simultaneous solidification. Liquids that freeze at room temperature would be preferable, i.e. tertiary butyl alcohol (m.p.= 25°C) or succinonitrile (m.p. = 58°C).
- Modeling of the relaxation of fibers and the kinetics of infiltration with superheated metal is an important topic that needs to be addressed, both for cases (i) and (ii). In the remelted zone region, no solid metal is present and the pressure gradient should be much lower as compared to region 1, thus, the fibers in that remelted region should completely relax if frictional effects are negligible.
- Modeling for variable pressure processes, such as squeeze casting, should be addressed.

Appendix (3.1) - Program for sponge infiltration

```
REM*** Compression of Sponge USING pure Ethylene Glycol*****
' Using the Runge-Kutta scheme for integration
' and converging with Newton-Raphson method for
' non-linear systems, utilizing
' the LU decomposition method to solve
' the ERROR vector of the initial parameters.

DEFDBL A-x
DEFSTR Y
PRINT "This program is to calculate Psisq for a COMPRESSIBLE Sponge"
PRINT
PRINT
Sample$="Sponge"                'Saving in file called 'sponge'
Y$=CHR$(9)
DIM Vf(1000)
DIM VfP(1000)
DIM P(3)
DIM L(1000)
DIM LP(1000)
DIM S(1000)
DIM SP(1000)
DIM K(1000)
DIM SigmaP(1000)
DIM Chi(1000)
DIM F(5)
DIM G(5)
DIM H(5)
DIM Root(3)
DIM A(3,3),Indx(3),VV(3), B(3)
DIM Mat(3,3),Orig(3)

OPEN Sample$ FOR OUTPUT AS #1

REM Setting initial constants:

'*****
'Experimental values:
  Pressure=99532#      ' This is the pressure of the infiltration of the
sponge
  P=Pressure
```

```

Psisq=.0001          'This is the experimental Psisq value

perm=.00000000014729# 'These two equations represent the
permeability of the sponge
top=-6.9654#         'from the equation:
K(m^2)=perm*10^(top*Vf)

      mu=.01563#          'Liquid Ethylene Glycol viscosity
'*****
' These are the constants from graphing Pa vs Vf and curve-fitting with
polynomial
'       where : sigma =
A+B*Vf(n)+C*Vf(n)^2+D*Vf(n)^3+E*Vf(n)^4+F*Vf^5..

A=-23291640.367#
B=713493184.47#
C=-9255284913.299999#
D=65974869633#
E=-279182342130#
F= 701653833430#
G=-970226735080#
H=569801837660#
I=0
'*****

      x=200          'X = number of iterations
'*****

'Using Newton-Raphson to find Vf roots at Chi=0,1 and of unfiltered
preform

Vfcomp=.33          ' These are internal guesses
Vf(0)=.14
Root(2)=Vfcomp
Root(1)=Vfcomp
Root(0)=Vf(0)
      Xacc=.00000001#          ' Describes accuracy of root .....+-Xacc
      Jmax=400          'Number of iterations

FOR R= 2 TO 0 STEP -1
'*****
      IF R=2 THEN
          P(R)=P          'This is the total pressure drop= Pcap+Pvisc
      END IF
'*****
      IF R=1 THEN

```

```

        Pcap=0
        Pvisc=(P-Pcap)
        P(R)=Pvisc
    END IF
'*****
    IF R=0 THEN                ' changing Pressure to find root at chi=0
        P(R)=0
    END IF
'*****
    FOR J=1 TO Jmax
        stress =
A+B*Root(R)+C*Root(R)^2+D*Root(R)^3+E*Root(R)^4+F*Root(R)^5+G*
Root(R)^6+H*Root(R)^7+I*Root(R)^8-P(R)
        SigmaP=
B+2*C*Root(R)+3*D*Root(R)^2+4*E*Root(R)^3+5*F*Root(R)^4+6*G*Ro
ot(R)^5+7*H*Root(R)^6+8*I*Root(R)^7
        dx=stress/SigmaP
        Root(R)=Root(R)-dx
        IF ABS(dx)<Xacc THEN    'testing whether accuracy is within limits
            GOTO Place
        END IF
    NEXT J
Place:
    Vfcomp=Root(2)            ' Vfcomp=Vf the fibers are compressed to initially
    Vffront= Root(1)         'Vffront =Vf right behind infiltration front
    Vf(0)=Root(0)            'Vf(0)=Vf at beginning of preform entrance
    NEXT R
'*****
L(x)=.4043101                'guesses only
L(0)=.393
S(0)=-.0988#

del=.000001#                ' multiplier used to find new value of increment

PRINT "P=";Pressure
PRINT "Pcap="; Pcap
PRINT "Pvisc=";Pvisc
PRINT "Ptotal=";P
PRINT
PRINT "Vfcomp=";Vfcomp
PRINT "Vf (chi=0)="; Vf(0)
PRINT "Vf (chi=1) ="; Vffront
PRINT "psisq=";Psisq
PRINT "L(x)="; L(x)
PRINT "del=";del
PRINT "x=";x

```

```

*****
Integration:

      DelL=L(0)*del           'These are the increments used to minimize
      Delpsisq=Psisq*del     ' the errors of the boundary conditions
      dels=S(0)*del

      Psum=0                  ' summation used to integrate pressure drop

FOR counter%= 1 TO 4        'counter% used for converging method

      constant=mu*Psisq

*****
'Setting new initial values

SigmaP(0)=
B+2*C*Vf(0)+3*D*Vf(0)^2+4*E*Vf(0)^3+5*F*Vf(0)^4+6*G*Vf(0)^5+7*H*
Vf(0)^6+8*I*Vf(0)^7

      K(0)=perm*10^(top*Vf(0))
      VfP(0)= (L(0)-S(0))*(1-Vf(0))*constant/K(0)/SigmaP(0)
      LP(0)= -VfP(0)*(0/2+S(0)-L(0))/(1-Vf(0))
      SP(0)= VfP(0)/Vf(0)*(0/2+S(0)-S(0))/3
      ' These are taken w.r.t. chi

*****
FOR n=0 TO x-2 STEP 2      'Integration begins at chi=0 and
                           'goes forward toward 1. Midpoints
are                          'positions where n= odd number

*****
' We will find the midpoint values of Vf, L, S, etc.

Vf(n+1)=Vf(n)+VfP(n)/x
L(n+1)=L(n)+LP(n)/x
S(n+1)=S(n)+SP(n)/x
SigmaP(n+1)=
B+2*C*Vf(n+1)+3*D*Vf(n+1)^2+4*E*Vf(n+1)^3+5*F*Vf(n+1)^4+6*G*Vf(
n+1)^5+7*H*Vf(n+1)^6+8*I*Vf(n+1)^7
K(n+1)=perm*10^(top*Vf(n+1))
Chi(n+1)=(n+1)/x
*****
' Now find the derivatives at the midpoint

```

```

VfP(n+1)= (L(n+1)-S(n+1))*(1-
Vf(n+1))*constant/K(n+1)/SigmaP(n+1)
LP(n+1)= -VfP(n+1)*(Chi(n+1)/2+S(0)-L(n+1))/(1-Vf(n+1))
SP(n+1)= VfP(n+1)/Vf(n+1)*(Chi(n+1)/2+S(0)-S(n+1))/3

```

```

'*****
'Now find the new values of Vf, L, S, etc. at the new chi value using the
' midpoint derivatives

```

```

Vf(n+2)=Vf(n)+VfP(n+1)*2/x
L(n+2)=L(n)+LP(n+1)*2/x
S(n+2)=S(n)+SP(n+1)*2/x
SigmaP(n+2)=
B+2*C*Vf(n+2)+3*D*Vf(n+2)^2+4*E*Vf(n+2)^3+5*F*Vf(n+2)^4+6*G*Vf(
n+2)^5+7*H*Vf(n+2)^6+8*I*Vf(n+2)^7
K(n+2)=perm*10^(top*Vf(n+2))
Chi(n+2)=(n+2)/x

```

```

'*****
'New value of the derivative at the new value of chi
VfP(n+2)= (L(n+2)-S(n+2))*(1-
Vf(n+2))*constant/K(n+2)/SigmaP(n+2)
LP(n+2)= -VfP(n+2)*(Chi(n+2)/2+S(0)-L(n+2))/(1-Vf(n+2))
SP(n+2)= VfP(n+2)/Vf(n+2)*(Chi(n+2)/2+S(0)-S(n+2))/3

```

```

'*****
' Integrating the pressure drop over the length of infiltrated sponge

```

```

IF counter%=1 THEN
Psum=Psum+(L(n+1)-S(n+1))*constant*(1-Vf(n+1))/-K(n+1)*2/x
END IF

```

```

'*****
NEXT n

```

```

'*****
'Taking new values for Newton-Raphson method

```

```

IF counter%=1 THEN
OrigL=L(0) 'These are the variables to be adjusted
OrigPsisq=Psisq
OrigS=S(0)

```

```

F(counter%)=Vf(x)-Vffront 'These equations want to be zeroed
G(counter%)=L(x)-S(0)-.5

```

H(counter%)=S(x)

```
IF ABS(F(counter%))<.00001 THEN 'Testing final conditions to end
  IF ABS(G(counter%))<.00001 THEN
    IF ABS(H(counter%))<.00001 THEN
      GOTO finish
    END IF
  END IF
END IF
```

Orig(1)=-F(1)
Orig(2)=-G(1)
Orig(3)=-H(1)

L(0)=OrigL+DelL 'changing to (u+∂u) and keeping v,w

END IF

```
IF counter%=2 THEN
  F(counter%)=Vf(x)-Vffront 'F(u+∂u,v,w)
  G(counter%)=L(x)-S(0)-.5 'G(u+∂u,v,w)
  H(counter%)=S(x) 'H(u+∂u,v,w)
  Psisq=OrigPsisq+ Delpsisq 'original u,w and changing to (v+∂v)
  L(0)=OrigL
  S(0)=OrigS
```

END IF

```
IF counter%=3 THEN
  F(counter%)=Vf(x)-Vffront 'F(u,v+∂v,w)
  G(counter%)=L(x)-S(0)-.5 'G(u,v+∂v,w)
  H(counter%)=S(x) 'H(u,v+∂v,w)
  Psisq=OrigPsisq 'original u,v and changing (w+∂w)
  L(0)=OrigL
  S(0)=OrigS+dels
```

END IF

```
IF counter%=4 THEN
  F(counter%)=Vf(x)-Vffront 'F(u,v,w+∂w)
  G(counter%)=L(x)-S(0)-.5 'G(u,v,w+∂w)
  H(counter%)=S(x) 'H(u,v,w+∂w)
```

```
'*****
Mat(1,1)=(F(2)-F(1))/DelL '(F(u+∂u,v,w)-F(u,v,w))/∂u
Mat(1,2)=(F(3)-F(1))/Delpsisq '(F(u,v+∂v,w)-F(u,v,w))/∂v
```

```

Mat(1,3)=(F(4)-F(1))/dels      '(F(u,v,w+∂w)-F(u,v,w))/∂w
Mat(2,1)=(G(2)-G(1))/DelL      '(G(u+∂u,v,w)-G(u,v,w))/∂u
Mat(2,2)=(G(3)-G(1))/Delpsisq  '(G(u,v+∂v,w)-G(u,v,w))/∂v
Mat(2,3)=(G(4)-G(1))/dels      '(G(u,v,w+∂w)-G(u,v,w))/∂w
Mat(3,1)=(H(2)-H(1))/DelL      '(H(u+∂u,v,w)-H(u,v,w))/∂u
Mat(3,2)=(H(3)-H(1))/Delpsisq  '(H(u,v+∂v,w)-H(u,v,w))/∂v
Mat(3,3)=(H(4)-H(1))/dels      '(H(u,v,w+∂w)-H(u,v,w))/∂w
*****
' Determining new values of L(chi=0), psisq, S(chi=0)

Errmatdim=3      'This is the dimension of the error matrix
Errmatdimmax=3  'Max dimension
Exchange=1      'Don't worry about- part of subprogram

CALL Decomp (Mat(),Errmatdim,Errmatdimmax,Indx(),Exchange)
CALL Backsub (Mat(),Errmatdim,Errmatdimmax,Indx(),Orig())
PRINT
*****
L(0)= OrigL+Orig(1)
Psisq=OrigPsisq + Orig(2)      'Adding errors on to original values
S(0)=OrigS+Orig(3)
END IF
*****
NEXT counter%      'Changing delta u,v,or w
*****
PRINT Vf(x)
PRINT "Vdiff=";Vf(x)-Vffront
PRINT "L-s-.5=";L(x)-S(0)-.5
PRINT "S(x)=";S(x)
PRINT "Psisq=";Psisq
PRINT "Integrated Pressure="; Psum
PRINT "Original Pressure drop="; -Pvisc
PRINT "Pressure difference=";-Pvisc-Psum

PRINT
BEEP

GOTO Integration

finish:
PRINT " Final Vdiff=";Vf(x)-Vffront
PRINT " Final L-s-.5=";L(x)-S(0)-.5
PRINT "Final s(x)=";S(x)
PRINT "Final L(x)=";L(x)
PRINT "Final Psisq=";Psisq
PRINT "Final Integrated Pressure="; Psum

```



```

PRINT "Final Original Pressure drop="; -Pvisc
PRINT "Final Pressure difference=";-Pvisc-Psum
PRINT
PRINT "Saved in file called"; Sample$

FOR n=0 TO x STEP 2
  PRINT #1, CSNG(n/x);Y$; CSNG(Vf(n));Y$; CSNG(L(n));Y$;
  CSNG(S(n));Y$; CSNG(K(n));Y$;CSNG(Psisq)
NEXT n
CLOSE #1
BEEP
END
'*****
**
SUB Decomp (A(3),n,NP,Indx(3),D) STATIC

Nmax=3
tiny=1E-20

FOR I=1 TO n
  AAMax=0
  FOR J=1 TO n
    IF ABS(A(I,J))>AAMax THEN AAMax=ABS(A(I,J))
  NEXT J
  IF AAMax=0 THEN
    PRINT "Singular matrix"
  END IF
  VV(I)=1#/AAMax
NEXT I

FOR J=1 TO n      'This is the loop over columns of Crout's method
  FOR I=1 TO J-1
    Sum=A(I,J)
    FOR K=1 TO I-1
      Sum=Sum-A(I,K)*A(K,J)
    NEXT K
    A(I,J)=Sum
  NEXT I
  AAMax=0      'initialize for search for largest pivotal element
  FOR I=J TO n
    Sum=A(I,J)
    FOR K=1 TO J-1
      Sum=Sum-A(I,K)*A(K,J)
    NEXT K
    A(I,J)=Sum
    dum=VV(I)*ABS(Sum)

```

```

        IF dum>=AAMax THEN          'is it better than the best so far?
            IMax=I
            AAMax=dum
        END IF
    NEXT I

    IF J<>IMax THEN
        FOR K=1 TO n
            dum=A(IMax,K)
            A(IMax,K)=A(J,K)
            A(J,K)=dum
        NEXT K
        D=-D
        VV(IMax)=VV(J)
    END IF
    Indx(J)=IMax
    IF A(J,J)=0 THEN A(J,J)=tiny
    IF J<> n THEN
        dum=1#/A(J,J)
        FOR I= J+1 TO n
            A(I,J)=A(I,J)*dum
        NEXT I
    END IF
NEXT J

END SUB
END
*****
SUB Backsub (A(3), n, NP, Indx(3), B(3)) STATIC
    II=0
    FOR I=1 TO n
        LL=Indx(I)
        Sum=B(LL)
        B(LL)=B(I)
        IF II<>0 THEN
            FOR J=II TO I-1
                Sum=Sum-A(I,J)*B(J)
            NEXT J
        ELSEIF Sum<>0 THEN
            II=I
        END IF
        B(I)=Sum
    NEXT I
    FOR I=n TO 1 STEP -1
        Sum=B(I)
        IF I< n THEN

```

```
FOR J=I+1 TO n
  Sum=Sum-A(I,J)*B(J)
NEXT J
END IF
B(I)=Sum/A(I,I)
NEXT I
END SUB
```

Appendix (3.2) - Program for alumina fiber infiltration

```
REM*** Compression of Saffil preforms using pure Aluminum*****
' Using the Runge-Kutta scheme for integration
' and converging with Newton-Raphson method for
' non-linear systems, utilizing
' the LU decomposition method to solve
' the error vector of the initial parameters.
WE ARE FITTING THIS PROGRAM TO THE .1883 COMPRESSION
CURVE
```

```
*****
```

```
DEFDBL A-x,z
DEFSTR Y

Y$=CHR$(9)
DIM Vf$(1000)
DIM Vs$(1000)
DIM Vsf$(1000)
DIM VsfP$(1000)
DIM P(3)
DIM L$(1000)
DIM LP$(1000)
DIM S$(1000)
DIM SP$(1000)
DIM K$(1000)
DIM SigmaP$(1000)
DIM Chi(1000)
DIM F$(50)
DIM G$(50)
DIM Root$(3)
DIM A(3,3),Indx(3),VV(3), B(3)
DIM Mat$(3,3),Orig$(3)
```

```
*****
```

```
INPUT "Name of file=" ;n$
OPEN "clip:" FOR INPUT AS #2
OPEN n$ FOR OUTPUT AS #3
WHILE NOT EOF(2)
INPUT #2, InitVf#,Tf#, Pressure#
```

```
PRINT "This program is to calculate Psisq for a compressible preform"
```

```

PRINT
PRINT
'*****
REM   Finding the initial Vf that the fibers are compressed to:

P#=Pressure#*6893#           'converts Psi into pascals
Pcomp#=P#
PRINT Pcomp#

IF Pcomp#< 300*6893# THEN
PRINT Pcomp#
BEEP

    Vfcompfit#=.18838+5.3766E-09*P#-3.966583D-15*P#^2+5.5275E-21*P#^3-
5.1431848D-27*P#^4+1.865145D-33*P#^5
    PRINT Vfcompfit#

ELSE
    Vfcompfit#=.136477+3.47692E-08*P#
    PRINT Vfcompfit#

END IF

'*****

REM Setting initial constants:

'*****
' These are the physical values of the metal and preform
Psisq#=.0000001

T=.027219
U=55.4816
V=-1169.453
W=8646.153
alpha=.333

    Tm#=660           'Initial metal temperature
    mu=.0013         'Liquid aluminum viscosity
    hydrorad=.00000272# 'hydraulic radius of Saffil
    Fiberheat=4000000# 'equals fiber density*fiber heat capacity
    Alfusion=950000000# ' = Aluminum density * Heat fusion

    LAsurftense=.914 'This is the liquid-atmosphere surface tension of
Al (J/m^2)

```

```

*****
' These are the constants from graphing Pa vs Vf and curvefitting
'   where : sigma =Pcomp#*(1-(T+U(Vfcomp-Vf)/(Vfcomp-
Vf)^alpha..)

*****
      x=300          'X = number of iterations
*****

'Using Newton-Raphson to find Vf roots at Chi=0,1 and of uninfiltreated
preform

Vf#(0)=Vfcompfit#-.000001      ' These are internal guesses
Root#(2)=Vfcompfit#
Root#(1)=Vfcompfit#-.000001
Root#(0)=Vf#(0)
Xacc=.00000001#                ' Describes accuracy of root .....+-
Xacc
Jmax=400                        'Number of iterations

derv=-(Vfcompfit#-.1883)^-(alpha)

FOR r= 1 TO 0 STEP -1
*****
*****
  IF r=1 THEN
    ' This calculates the capillary pressure# drop that the
    ' liquid experiences at the infiltration front
    ' This is taken from labbook 16, p.6 (Terry Wong's paper)
    Sf=-977800! + 2.2217E+07*Vfcompfit#
    Pcap#=-Sf*LASurftense*COS(106/180*3.141592)

    IF Pcap#>Pcomp# THEN
      Pvisq#=0
      Larry=0
      PRINT "Under the capillary pressure-- no infiltration"
      BEEP
      BEEP

      GOTO Frozen
    END IF

    Pvisc#=(P#-Pcap#)
    P(r)=Pvisc#

```

```

END IF
'*****
IF r=0 THEN          ' changing pressure# to find root at chi=0
  P(r)=0
END IF
'*****
FOR J=1 TO Jmax
  stress = Pcomp#*(1-(T+U*((Vfcompfit#-Root#(r))/(Vfcompfit#-
.1883)^.333)+V*((Vfcompfit#-Root#(r))/(Vfcompfit#-
.1883)^.333)^2+W*((Vfcompfit#-Root#(r))/(Vfcompfit#-.1883)^.333)^3))-
P(r)
  SigmaP#= -Pcomp#*(U*derv+2*V*((Vfcompfit#-
Root#(r))/(Vfcompfit#-.1883)^.333)*derv+3*W*((Vfcompfit#-
Root#(r))/(Vfcompfit#-.1883)^.333)^2*derv)
  dx=stress/SigmaP#
  Root#(r)=Root#(r)-dx
  IF ABS(dx)<Xacc THEN  'testing whether accuracy is within limits
    GOTO Place
  END IF
NEXT J

```

Place:

```

Vfcomp#=Root#(2)    'Vfcomp#=Vf the fibers are compressed to
initially
Vffront#= Root#(1)  'Vffront# =Vf right behind infiltration front
Vf#(0)=Root#(0)    'Vf#(0)=Vf at beginning of preform entrance
NEXT r

```

'*****

```

L#(x)=10           'guesses only
L#(0)=5
S#(0)=-1

```

```

del#=.001#        'multiplier used to find new value of increment

```

```

Vsfront#= Fiberheat*Vffront#*(Tm#-Tf#)/Alfusion
Gsfront=Fiberheat*Vffront#*(Tm#-Tf#)/Alfusion/(1-Vffront#)
Vsffront#=Vsfront#+Vffront#
IF Vsffront#>=3.141592/4 THEN
  PRINT "Matrix completely frozen first"
  Psisq#=0
  GOTO Frozen
END IF
solidfibrad#=hydrorad*SQR(Vsffront#/Vffront#)
adj#=(hydrorad/solidfibrad#)^2
d(stress)/dVf*adj=d(stress)/dVsf

```

$$V_{sf}(0) = V_f(0) / \text{adj\#}$$

$$V_{sf}(x) = V_{ffront\#} / \text{adj\#}$$

'Calculating Larry's stuff at the infiltration front:

$$K_{front\#} = 2 * \text{SQR}(2) / 9 * \text{solidfibrad\#}^2 / V_{sffront\#} * (1 - \text{SQR}(4 * V_{sffront\#} / 3.141592))^2.5$$

$$\text{Larry} = 2 * P_{visc\#} * K_{front\#} / \mu / (1 - V_{ffront\#})$$

$$L_{Vsfratio\#} = (1 - V_{fcomp\#}) / (1 - V_{sffront\#})$$

'This $L_{Vsfratio\#}$ = ratio needed to describe the boundary condition
'L @ $\chi=1$ right behind the infiltration front.

$$S_{Vsfratio\#} = (V_{fcomp\#} - V_{ffront\#}) / V_{ffront\#}$$

'This ratio is needed to describe the S after the infiltration front passes the fibers.

```

PRINT "Tf#="; Tf#
PRINT "Tm#="; Tm#
PRINT "P="; Pressure#
PRINT "Pcap="; Pcap#
PRINT "Pvisc="; Pvisc#
PRINT "Ptotal="; P
PRINT
PRINT "Vfcomp#="; Vfcomp#
PRINT "Vf (chi=0)="; Vf(0)
PRINT "Vf (chi=1) =" ; Vffront#
PRINT
PRINT "Vsf (chi=0) =" ; Vsf(0)
PRINT "Vsf (chi=1) =" ; Vsf(x)
PRINT
PRINT "r="; hydrorad
PRINT "Psisq#="; Psisq#
PRINT "L#(x)="; L(x)
PRINT "del="; del#
PRINT "x="; x
PRINT "Gs @ front="; Gscomp
PRINT "Fiber radius="; solidfibrad#

```

Integration:

$$\text{delL\#} = L\#(0) * \text{del\#}$$

$$\text{delPsisq\#} = P_{sisq\#} * \text{del\#}$$


```

        delS#=S#(0)*del#
        Psum#=0

FOR counter%= 1 TO 4          'counter% used for converging method

        constant#=mu*Psisq#

'*****
'Setting new initial values

        SigmaP#(0)= -Pcomp#*(U*derv+2*V*((Vfcomp#-Vf(0))/(Vfcomp#-
.1883)^.333)*derv+3*W*((Vfcomp#-Vf(0))/(Vfcomp#-.1883)^.333)^2*derv)
        ' THE DERIVATIVE OF THE STRESS IS
        ' TAKEN WITH RESPECT TO Vf
        IF Vsf#(0) >= 3.14159/4 THEN
                PRINT "Matrix completely frozen initial"
                Psisq#=0
                GOTO Frozen
        END IF

        K#(0)=2*SQR(2)/9*solidfibrad#^2/Vsf#(0)*(1-
SQR(4*Vsf#(0)/3.141592))^2.5
        VsfP#(0)= (L#(0)-S#(0))*(1-
Vsf#(0))*constant#/K#(0)/SigmaP#(0)/adj#
        LP#(0)= -VsfP#(0)*(0/2+S#(0)-L#(0))/(1-Vsf#(0))
        SP#(0)= VsfP#(0)/Vsf#(0)*(0/2+S#(0)-S#(0))
        ' These are taken w.r.t. chi

'*****
FOR n=0 TO x-2 STEP 2          ' Integration begins at chi=0 and
                                'goes forward toward 1. Midpoints are
                                'positions where n= odd number

'*****
' We will find the midpoint values of Vf, L, S, etc.

Vsf#(n+1)=Vsf#(n)+VsfP#(n)/x
        IF Vsf#(n+1)>=3.141592/4 THEN
                PRINT "Matrix completely frozen 1"
                Psisq#=0
                GOTO Frozen
        END IF

Vf#(n+1)=Vf#(n)+adj#
L#(n+1)=L#(n)+LP#(n)/x

```

```

S#(n+1)=S#(n)+SP#(n)/x
SigmaP#(n+1) =-Pcomp#*(U*derv+2*V*((Vfcomp#-Vf(n+1))/(Vfcomp#-
.1883)^.333)*derv+3*W*((Vfcomp#-Vf(n+1))/(Vfcomp#-
.1883)^.333)^2*derv)
K#(n+1)=2*SQR(2)/9*solidfibrad#^2/Vsf#(n+1)*(1-
SQR(4*Vsf#(n+1)/3.141592))^2.5
Chi(n+1)=(n+1)/x

```

```

'*****

```

```

' Now find the derivatives at the midpoint

```

```

    VsfP#(n+1)= (L#(n+1)-S#(n+1))*(1-
Vsf#(n+1))*constant#/K#(n+1)/SigmaP#(n+1)/adj#
    LP#(n+1)= -VsfP#(n+1)*(Chi(n+1)/2+S#(0)-L#(n+1))/(1-Vsf#(n+1))
    SP#(n+1)= VsfP#(n+1)/Vsf#(n+1)*(Chi(n+1)/2+S#(0)-S#(n+1))

```

```

' These are taken w.r.t. chi

```

```

'*****

```

```

'Now find the new values of Vf, L, S, etc. at the new chi value using the
' midpoint derivatives

```

```

Vsf#(n+2)=Vsf#(n)+VsfP#(n+1)*2/x
IF Vsf#(n+2)>=3.14159/4 THEN
    PRINT "Matrix completely frozen 2"
    Psisq#=0
    GOTO Frozen
END IF

```

```

Vf#(n+2)=Vsf#(n+2)*adj#
L#(n+2)=L#(n)+LP#(n+1)*2/x
S#(n+2)=S#(n)+SP#(n+1)*2/x
SigmaP#(n+2)=-Pcomp#*(U*derv+2*V*((Vfcomp#-Vf(n+2))/(Vfcomp#-
.1883)^.333)*derv+3*W*((Vfcomp#-Vf(n+2))/(Vfcomp#-
.1883)^.333)^2*derv)
K#(n+2)=2*SQR(2)/9*solidfibrad#^2/Vsf#(n+2)*(1-
SQR(4*Vsf#(n+2)/3.141592))^2.5
Chi(n+2)=(n+2)/x

```

```

'*****

```

```

'New value of the derivative at the new value of chi

```

```

    VsfP#(n+2)= (L#(n+2)-S#(n+2))*(1-
Vsf#(n+2))*constant#/K#(n+2)/SigmaP#(n+2)/adj#
    LP#(n+2)= -VsfP#(n+2)*(Chi(n+2)/2+S#(0)-L#(n+2))/(1-Vsf#(n+2))
    SP#(n+2)= VsfP#(n+2)/Vsf#(n+2)*(Chi(n+2)/2+S#(0)-S#(n+2))

```

```

'*****

```

```

IF counter%=1 THEN

```

```

        Psum#=Psum#+(L#(n+1)-S#(n+1))*constant#*(1-Vsf#(n+1))/-
K#(n+1)*2/x
        END IF
'*****
NEXT n

'*****
'Taking new values for Newton-Raphson method

IF counter%=1 THEN
    OrigL#=L#(0)                'These are the variables to be adjusted
    OrigPsisq#=Psisq#
    OrigS#=S#(0)
                                'These equations want to be zeroed

    F#(counter%)=Vf#(x)-Vffront#
    G#(counter%)=L#(x)-(.5+S#(0))*LVsfratio#
    H#(counter%)=S#(x)+(.5+S#(0))*SVsfratio#

        IF ABS(F#(counter%))<.0001 THEN    'Testing final conditions to
end
            IF ABS(G#(counter%))<.0001 THEN
                IF ABS(H#(counter%))<.0001 THEN
                    GOTO finish
                END IF
            END IF
        END IF

    Orig#(1)=-F#(1)
    Orig#(2)=-G#(1)
    Orig#(3)=-H#(1)

    L#(0)=OrigL#+delL#          'changing to (u+∂u) and keeping v,w

END IF

IF counter%=2 THEN
    F#(counter%)=Vf#(x)-Vffront#          'F#(u+∂u,v,w)
    G#(counter%)=L#(x)-(.5+S#(0))*LVsfratio#    'G#(u+∂u,v,w)
    H#(counter%)=S#(x)+(.5+S#(0))*SVsfratio#    'H#(u+∂u,v,w)
    Psisq#=OrigPsisq#+ delPsisq#    'original u,w and changing to (v+∂v)
    L#(0)=OrigL#
    S#(0)=OrigS#

END IF

```

```

IF counter%=3 THEN
  F#(counter%)=Vf#(x)-Vffront#           'F#(u,v+∂v,w)
  G#(counter%)=L#(x)-(.5+S#(0))*LVsfratio# 'G#(u,v+∂v,w)
  H#(counter%)=S#(x)+(.5+S#(0))*SVsfratio# 'H#(u,v+∂v,w)
  Psisq#=OrigPsisq#                       'original u,v and changing (w+∂w)
  L#(0)=OrigL#
  S#(0)=OrigS#+delS#

```

```

END IF

```

```

IF counter%=4 THEN
  F#(counter%)=Vf#(x)-Vffront#           'F#(u,v,w+∂w)
  G#(counter%)=L#(x)-(.5+S#(0))*LVsfratio# 'G#(u,v,w+∂w)
  H#(counter%)=S#(x)+(.5+S#(0))*SVsfratio# 'H#(u,v,w+∂w)

```

```

'*****
  Mat#(1,1)=(F#(2)-F#(1))/delL#           '(F#(u+∂u,v,w)-F#(u,v,w))/∂u
  Mat#(1,2)=(F#(3)-F#(1))/delPsisq#      '(F#(u,v+∂v,w)-F#(u,v,w))/∂v
  Mat#(1,3)=(F#(4)-F#(1))/delS#          '(F#(u,v,w+∂w)-F#(u,v,w))/∂w
  Mat#(2,1)=(G#(2)-G#(1))/delL#           '(G#(u+∂u,v,w)-G#(u,v,w))/∂u
  Mat#(2,2)=(G#(3)-G#(1))/delPsisq#      '(G#(u,v+∂v,w)-G#(u,v,w))/∂v
  Mat#(2,3)=(G#(4)-G#(1))/delS#          '(G#(u,v,w+∂w)-G#(u,v,w))/∂w
  Mat#(3,1)=(H#(2)-H#(1))/delL#           '(H#(u+∂u,v,w)-H#(u,v,w))/∂u
  Mat#(3,2)=(H#(3)-H#(1))/delPsisq#      '(H#(u,v+∂v,w)-H#(u,v,w))/∂v
  Mat#(3,3)=(H#(4)-H#(1))/delS#          '(H#(u,v,w+∂w)-H#(u,v,w))/∂w

```

```

'*****

```

```

' Determining new values of L#(chi=0), Psisq#, S(chi=0)

```

```

Errmatdim=3           'This is the dimension of the error matrix
Errmatdimmax=3       'Max dimension
Exchange=1

```

```

CALL Decomp (Mat#(),Errmatdim,Errmatdimmax,Indx(),Exchange)
CALL Backsub (Mat#(),Errmatdim,Errmatdimmax,Indx(),Orig#())
  PRINT

```

```

'*****

```

```

'Multiplying by increment so the adjustment
'doesn't cause the program to overshoot

```

```

L#(0)= OrigL#+Orig#(1)*.5
Psisq#=OrigPsisq#+Orig#(2)*.5
S#(0)=OrigS#+Orig#(3)*.5
IF Psisq#<0 THEN
  Psisq#=OrigPsisq#

```

END IF

END IF

NEXT counter%

PRINT "Vdiff=";Vf#(x)-Vffront#
PRINT "L-s-.5=";L#(x)-(.5+S#(0))*LVsfratio#
PRINT "S#(x)=";S#(x)+(.5+S#(0))*SVsfratio#
PRINT "Psisq#=";Psisq#
PRINT "Integrated pressure#="; Psum#
PRINT "Original pressure# drop="; -Pvisc#
PRINT "pressure# difference=";-Pvisc#-Psum#
PRINT Vsf#(x)

PRINT
BEEP
GOTO Integration

finish:
PRINT " Final Vdiff=";Vf#(x)-Vffront#
PRINT " Final L-s-.5=";L#(x)-(.5+S#(0))*LVsfratio#
PRINT "Final S#(x)=";S#(x)+(.5+S#(0))*SVsfratio#
PRINT "Final Psisq#=";Psisq#
PRINT "Final Integrated pressure#="; Psum#
PRINT "Final Original pressure# drop="; -Pvisc#
PRINT "Final pressure# difference=";-Pvisc#-Psum#
Pdiff=-Pvisc#-Psum#
PRINT L#(x), S#(0), Pcap

Frozen:
PRINT
#3,CSNG(InitVf#);Y\$;CSNG(Tf#);Y\$;CSNG(Tm#)Y\$;CSNG(P);Y\$;CSNG(P
sisq#);Y\$;CSNG(Larry);Y\$;CSNG(Larryrelax);Y\$;CSNG(Vsf#(x))
BEEP
BEEP
BEEP
WEND
CLOSE #2
CLOSE #3

END

SUB Decomp (A(3),n,NP,Indx(3),D) STATIC

```
Nmax=3
tiny=1E-20
```

```
D=1
FOR I=1 TO n
  AAMax=0
  FOR J=1 TO n
    IF ABS(A(I,J))>AAMax THEN AAMax=ABS(A(I,J))
  NEXT J
  IF AAMax=0 THEN
    PRINT "Singular matrix"
  END IF
  VV(I)=1/AAMax
NEXT I
```

```
FOR J=1 TO n
  Crout's method
  FOR I=1 TO J-1
    Sum=A(I,J)
    FOR K=1 TO I-1
      Sum=Sum-A(I,K)*A(K,J)
    NEXT K
    A(I,J)=Sum
  NEXT I
  AAMax=0
  element
  FOR I=J TO n
    Sum=A(I,J)
    FOR K=1 TO J-1
      Sum=Sum-A(I,K)*A(K,J)
    NEXT K
    A(I,J)=Sum
    dum=VV(I)*ABS(Sum)
    IF dum>=AAMax THEN
      IMax=I
      AAMax=dum
    END IF
  NEXT I

  IF J<>IMax THEN
    FOR K=1 TO n
      dum=A(IMax,K)
      A(IMax,K)=A(J,K)
      A(J,K)=dum
    NEXT K
```

'This is the loop over columns of

'initialize for search for largest pivotal

'is it better than the best so far?

```

    D=-D
    VV(IMax)=VV(J)
END IF
Indx(J)=IMax
IF A(J,J)=0 THEN A(J,J)=tiny
IF J<> n THEN
    dum=1/A(J,J)
    FOR I= J+1 TO n
        A(I,J)=A(I,J)*dum
    NEXT I
END IF
NEXT J

END SUB

SUB Backsub(A(3), n, NP, Indx(3), B(3)) STATIC
    II=0
    FOR I=1 TO n
        LL=Indx(I)
        Sum=B(LL)
        B(LL)=B(I)
        IF II<>0 THEN
            FOR J=II TO I-1
                Sum=Sum-A(I,J)*B(J)
            NEXT J
        ELSEIF Sum<>0 THEN
            II=I
        END IF
        B(I)=Sum
    NEXT I

    FOR I=n TO 1 STEP -1
        Sum=B(I)
        IF I< n THEN
            FOR J=I+1 TO n
                Sum=Sum-A(I,J)*B(J)
            NEXT J
        END IF
        B(I)=Sum/A(I,I)
    NEXT I

    END SUB

```

Appendix (4.1) - Coring apparatus and coring procedure.

The coring apparatus consisted of a modified hand-cranked tensile testing unit with a 12" (30.5 cm) caliper mounted to its side to measure shaft displacements to 0.001" ($2.5 \cdot 10^{-2}$ mm). A 0.625" (15.9 mm) diameter pivot head with a 0.375" (9.5 mm) hole drilled through its side was on the end of the shaft. The cutter or pusher could easily be attached to this pivoting head, either by an O-ring Cajon fitting or by a 0.375" (9.5 mm) pin.

The preforms and fused quartz tube were centered and braced using the cap guide, outside bracing tube, the small, inner, and outer plungers, and the aluminum base. The cap guide was primarily used to center the cutter on the top of the preform and prevent the preforms and fused quartz tube from coming out during the extraction of the inner preform cores. The outside bracing tube and outer plunger were used to brace and center the fused quartz tube. The small plunger was used to push the cut inner cores into the cutter further after cutting so they could be extracted without delamination.

The detailed procedure to cut the preforms was as follows:

- 1) Each fused quartz tube was premeasured to fit within the coring apparatus, both inside the outer bracing tube and the outer plunger. The tubes were cut to 9" (22.9 cm) and each end of the tube was sanded with 180 grit paper on a lathe to make the ends parallel, and afterwards flashed with an acetylene flame to remove any cracks on the ends.

2) The tube was placed over the inner and outer plungers, which were then adjusted so that distance between the plunger tops and the fused quartz tube top matched the total length of the preforms to be cut.

3) The pusher was attached to the pivot and lowered until it contacted the inside plunger and could not be lowered any more under gentle pressure. This distance was recorded and was used to calculate the cutting distance and pushing distances. The pusher and fused quartz tube were then removed.

4) After the inside plunger was lowered while keeping the outer plunger stationary, the small plunger was inserted inside with the narrow beveled end face up. The inside plunger was then re-adjusted until the small plunger top was exactly flush with the outer plunger top.

5) The fused quartz tube was again placed over the outer plunger until it rested on the aluminum base surface. The preforms were then inserted carefully inside the fused quartz tube. The preform top surface should be flush with the top of the fused quartz tube edge. The outer bracing tube, along with the cap guide, were then placed over the fused quartz tube and carefully screwed onto the outside of the aluminum base, totally encapsulating and immobilizing the fused quartz tube and fiber preforms (see Figure A-4.1-a)

6) The cutter was then attached to the pivot. The cutter was slowly lowered downward through the cap guide hole, cutting through the fiber preform until the appropriate distance was measured on the calipers, upon which time the small plunger was pushed slightly upward, forcing the cut preform cores slightly inside the cutter, as shown in Figure A-4.1-b. The cutter was then extracted from the cap guide. The small and inner plungers were then removed from the apparatus through the bottom of

the outer plunger, after which the cap guide was then unscrewed from the outside bracing tube.

7) A Grafoil™ insert was prerolled around a small diameter dowel and stabilized with a small paperclip attached to the edge of the rolled Grafoil™ from the inside. The paper also acted as a guide to insert the Grafoil roll up the hole of the outer plunger. The inner plunger was then inserted in the bottom to push the coiled Grafoil the remaining distance. Upon reaching the top of the outer plunger, the bottom of the Grafoil expands to fill the cavity left by the cutter. The paperclip is removed at this point (Figure A-4.1-c).

8) The cutter knife edge was inserted within the Grafoil roll and supported with an aluminum brace. The pusher was then placed in the cutter base mouth until the end of the pusher contacted the surface of the inner preform cores. The pivot was then brought down, causing the pusher to eject the cut preform cores from the inside of the cutter, as shown in Figure A-4.1-d. The cutter and brace were then removed and the pusher was continued downward to the correct distance where the inside cores match the distances of the outside cores in the fused quartz tube. The Grafoil™ sheath was then trimmed off, using a new razor blade.

Appendix (4.2) - Monofilament insertion procedure

The procedure for drilling the SiC fiber into preforms is as follows:

1) The cored preforms are slid into the fused quartz tube far enough to allow the aluminum cylinder to protrude from the end of the fused quartz tube slightly.

2) An elastic band, wrapped loosely around the 100 $\mu\ell$ tube end and 5 $\mu\ell$ mid-section, is used to prevent the tubes from collapsing. The bare end of the SiC fiber is threaded through the 100 $\mu\ell$ and 5 $\mu\ell$ glass pipettes in that order and the extended end of the 5 $\mu\ell$ tube is inserted in the centered hole of the aluminum cylinder. A pin vice, mounted in a drill press chuck, is lowered around the nickel-coated end of the SiC fiber until the pin vice mouth contacts the upper end of the 100 $\mu\ell$ pipette upon which time it is carefully tightened on the fiber circumference. (See Figure A-4.2)

3) The drill press is then turned on and the fiber is slowly drilled through the preforms. The 100 $\mu\ell$ pipette collapses as the pin vice mouth pushes against the top of the tube during the drilling process. Once total penetration is achieved, the rotation is stopped and the mouth of the pinvice is opened, releasing the SiC fiber. The bare fiber end is then pulled from the opposite end until the nickel coating contacts the surface of the top preform.

Appendix (4.3) - Alternative method for measuring preform permeability

The second method to test permeability involved taking the cut preform cylinder, greasing its sides with silicone grease, and then placing the cylinder in a fused quartz tube that was polished on its ends to take off any sharp edges. The mouth of a typical long circus balloon was then partially rolled inside out and stretched over the end of the fused quartz tube. By blowing in the opposite end of the tube and pulling gently on the balloon end, the preform would slip straight inside the balloon, leaving a tight rubber seal around its periphery. The sealed end of the

balloon was then cut off. The preform was then reinserted inside the fused quartz tube and both ends of the balloon are stretched over the ends of the fused quartz tube, suspending the preform in the middle of the tube. This procedure not only effectively sealed the sides of the preform but also exposed the faces of the preform fully to the flow of liquid. Electrical tape was wrapped over one end of the balloon to prevent the balloon from slipping. The other end of the tube was inserted into a double-ended O-ring fitting and tightened. Another long fused quartz tube, used for the standpipe, was inserted into the opposite side of the fitting. This tube was marked out along its length at various intervals in order to have distance markers during the experiment. The procedure for measuring permeability was then the same as described previously.

Appendix (5.1) - Viscosity of ethylene glycol

The viscosity of ethylene glycol can be expressed as a function of temperature using an Arrhenius type equation:

$$\eta = A \exp\left(\frac{\Delta G^*}{RT}\right) \quad (\text{A-5.1})$$

where η = viscosity (poise), A = constant (poise), T = temperature (K), R = gas constant (cal/K/mol), and ΔG^* = activation energy of viscosity (cal/mol). Ethylene glycol was chosen because its viscosity is high enough to allow the infiltration to be in the Darcy's Law regime and yet low enough to preform meaningful permeability experiments. Data for the viscosity of ethylene glycol was found in (Weast, p. F-39). By plotting

logarithm of viscosity versus $1/T$, the activation energy of viscosity can be calculated from the slope of the line. The activation energy of viscosity for ethylene glycol was calculated to be 6751 cal/mole with a constant of $1.81 \cdot 10^{-4}$ centipoise. The temperature of the liquid at the time of infiltration of the sponge was 25.75°C , giving a viscosity of 15.6 cp. During the permeability experiments, the temperature was approximately 23.5°C with the viscosity being approximately 17.0 cp.

Although the water content was not measured, the ethylene glycol used was obtained prepackaged from a source that was designated $<0.1\%$ H_2O by the manufacturer and sealed with a tight metal punch and metal cap. Approximately 2 ml water-based colorant per 2 gallons ethylene glycol, amounting to $<0.03\%$, was added to add contrast to the infiltration front. Therefore, the liquid viscosity of the ethylene glycol is assumed not to have changed significantly from theoretical values of pure liquid and should be well within experimental error.

Appendix (5.2) - Estimation of experimental error for sponge experiments

A. Hydrostatic pressure V_f measurements

As the mass and density of the sponge is fixed, the V_f will vary according to the following equation:

$$\frac{\Delta V_f}{V_f} = \frac{\Delta L}{L} + \frac{\Delta w_1}{w_1} + \frac{\Delta w_2}{w_2}$$

where w_1 and w_2 are both widths of the sponge, measured by a caliper, and L is the total length of the sponge, measured by an accurate ruler. At

high volume fractions of solid, the sponge was quite rigid; therefore, accurate measurements could be obtained. With $\Delta L \approx 0.25$ mm, $L = 159.5$ mm at 14.55 psi (10300 Pa), Δw_1 and $\Delta w_2 \approx 0.015$ " (0.38 mm), w_1 and $w_2 = 1.23$ " (31.24 mm) and 1.29" (32.77 mm), respectively, $\frac{\Delta V_f}{V_f} = 0.026$ error.

B. Permeability

Permeability K is determined from Equation (4.1) to be:

$$Kt = \frac{\mu L}{\rho g} \frac{A_c}{A_s} \ln \left(\frac{H}{H_o} \right) \quad (4.1)$$

The equation for the logarithmic error is:

$$\frac{\Delta K}{K} = \frac{\Delta \mu}{\mu} + \frac{\Delta L}{L} + \frac{\Delta \ln \left(\frac{H}{H_o} \right)}{\ln \left(\frac{H}{H_o} \right)} + \frac{\Delta A_s}{A_s}$$

Factors that vary most in this equation are μ , L , A_s , and the logarithmic portion of the equation. μ contributes the greatest error due to the temperature change. The temperature of the liquid in the permeability colume was taken within 0.1°C immediately after the permeability test. The temperature of the sponge and box was unknown, although the difference between room temperature and the liquid was never more than 1.2°C. As a conservative estimate, ΔT will be taken as $\pm 2^\circ\text{C}$, reflecting a change in ethylene glycol viscosity of ± 1.5 cp from the original average of 17.04 cp at $T = 23.5^\circ\text{C}$.

The largest error will occur in the boxes that have the smallest sponge dimensions. The widths of the smallest box were 1.373" (34.9 mm) and 1.317" (33.5 mm), with an error of ± 0.01 " (± 0.254 mm) on each

side, corresponding to an error in the cross-sectional area, A_s , of $\frac{\Delta A_s}{A_s} \approx 0.015$.

The error associated with the liquid heights were $\Delta H \approx \pm 1$ mm, which makes the term negligible. The height was determined to be $\Delta L \approx \pm 1$ mm at an original length of 69.9 mm in the smallest permeability box, giving an error of $\frac{\Delta L}{L} \approx 0.014$. Overall error in permeability K , therefore, is calculated to be:

$$\frac{\Delta K}{K} = \frac{\Delta \mu}{\mu} + \frac{\Delta L}{L} + \frac{\Delta A_s}{A_s} = 0.12$$

C. Infiltration length L

L was determined by measuring the distance of the infiltrating liquid from the entrance of the sponge to the liquid front as it straddled the line drawn across the sponge face. The major part of the error, therefore, will be in measuring the distance between the two points when the infiltration distance is the smallest, i.e. 23 seconds. Difficulty arises in measuring distances on the curved video monitor with a finite pixel width. As a conservative estimate, $\Delta L \approx 0.5$ mm from measuring from the screen, corresponding to 0.47 mm in actual length. At 23 seconds, the actual infiltration distance in the sponge was approximately 66.8 mm, corresponding to an error of $\frac{\Delta L}{L} \approx 0.7$ %.

D. Value of ψ^2

Although L was between two fixed points on the screen, error occurs in determining the time necessary for the liquid to reach L . The

infiltration front appeared to be somewhat curved and difficulty arose as the lighting of the distorted sponge interfered in determining the exact position of the non-planar front. It is estimated that the error involved in determining the time is approximately $\Delta t \approx 2$ seconds. As $\psi^2 = \frac{L^2}{t}$:

$$\frac{\Delta(\psi^2)}{\psi^2} = 2 \frac{\Delta L}{L} + \frac{\Delta t}{t}$$

For $t = 23$ seconds, the error will be approximately 10%.

E. Volume fraction V_f

A conservative error in measuring the distance on the screen is ± 0.5 mm. This corresponds to ± 0.45 mm (0.018") in actual length when measuring vertically. The smallest distance measured on the sponge is at the infiltration front, which in actual distance was measured as 33.18 mm (1.306"). The conversion of sponge width, w (inches), is made by the following equation:

$$V_f = 2.5589 - 3.194*w + 1.414*w^2 - 0.2134*w^3$$

Inserting the error in the equation, $\frac{\Delta V_f}{V_f}$ will be approximately 4%.

F. χ

At 23 seconds and $\chi = 0.67$,

$$x = 45.2 \text{ mm} \qquad \Delta x = 1.5 \text{ mm}$$

where x is the distance along the infiltration portion of the sponge. At this point the curvature of the lines drawn on the sponge tend to be the greatest. Therefore:

$$\frac{\Delta\chi}{\chi} = \frac{\Delta L}{L} + \frac{\Delta x}{x} \approx 4\%$$

Appendix (5.3) - Estimation of experimental error for composite experiments.

A. Volume fraction measurements

The volume fractions of the preforms used in experimentation were calculated from their mass in the as-received state. Due to moisture adsorbed on the surface of the fibers, the error in mass of a given preform at room temperature varied by approximately ± 0.005 grams from day to day, depending upon the humidity. However, if all the moisture was desorbed, the weight of the preform may vary by as much as ± 0.050 gm. The actual fiber preform V_f is obtained when all moisture is desorbed. The V_f of the Saffil™ fiber preform will vary by the following equation:

$$\frac{\Delta V_f}{V_f} = \frac{\Delta L}{L} + 2 \frac{\Delta D}{D} + \frac{\Delta m}{m}$$

where D is the diameter, L is the length of the preform, measured by a caliper, and m is the mass of the fiber preform.

L = 0.443" (11.3 mm)	$\Delta L \approx 0.005"$ (0.13 mm)
D = 0.669" (17 mm)	$\Delta D \approx 0.008"$ (0.25 mm)
m = 1.56 g	$\Delta m \approx 0.05$ g

$$\frac{\Delta V_f}{V_f} \approx 0.07 \text{ error}$$

The error calculated above assumed that the water adsorbed on the fiber surface is the major contribution to the change in mass. In comparing the V_f of preform to preform, as received from the manufacturer, the error in measuring the preform weight, due to scale inaccuracy and humidity change, is estimated to be approximately $\Delta m \approx 0.008\text{g}$, resulting in an error in V_f of $\frac{\Delta V_f}{V_f} \approx 0.04$.

B. Permeability

The equation for the logarithmic error is:

$$\frac{\Delta K}{K} = \frac{\Delta \mu}{\mu} + \frac{\Delta L}{L} + \frac{\Delta \ln \left(\frac{H}{H_0} \right)}{\ln \left(\frac{H}{H_0} \right)} + \frac{\Delta A_s}{A_s}$$

Factors that vary most in this equation are μ , L , and A_s . As a conservative estimate, ΔT will be taken as $\pm 0.5^\circ\text{C}$, reflecting a change in water viscosity of ± 0.012 cp from the original average of 0.98 cp at $T = 21.0^\circ\text{C}$.

Other errors include:

D = 0.65" (16.5 mm)	$\Delta D = 0.015"$ (0.4 mm)
L = 0.48" (12.2 mm)	$\Delta L = 0.010"$ (0.25 mm)

$$\frac{2\Delta D}{D} = \frac{\Delta A_s}{A_s} \approx 0.015$$

Therefore:

$$\frac{\Delta K}{K} = \frac{\Delta \mu}{\mu} + \frac{\Delta L}{L} + \frac{\Delta A_s}{A_s} \approx 0.08$$

C. V_f determination from dissolution

The volume of each slice of composite that was dissolved was determined by Equation (4.2). The distances of the slice were all measured accurately with a micrometer, therefore, minimal error was accrued due to the actual measuring device. The largest error occurred in measuring the width of the slice, because of the unparallel sides caused by the pliant diamond saw blade, and in measuring the weight of the slice itself. The smallest distances are used, therefore, in calculating V_f error by inserting the values in Equation (4.2).

$$c = 0.06" (1.5 \text{ mm}) \quad \Delta c = 0.003" (0.08 \text{ mm})$$

$$m = 0.041 \text{ g} \quad \Delta m = 0.001 \text{ g}$$

$$\frac{\Delta V_f}{V_f} \approx 0.07$$

D. V_f distance errors

In calculating ψ values for compressed samples, it was uncertain whether the SiC moved. What is known for certain is L_f at the end of the

infiltration. The positions of the various measured experimental values of V_f , shown in Figs. 5.9, 5.10, and 5.11, were therefore not necessarily resting at that point when the infiltration front came, but will be at most within the distance that the SiC fiber may have shifted during compression, relative to that point. This distance is $\Delta x_s = \pm (L_f - L(t)) \cdot \Delta e$, where Δe is the strain measured for the pressure when the infiltration front is at $L(t)$ on a similar V_f^0 in the dry compression tests. Other error that occurred was due to the width of the slice- or $\Delta x_w = \pm (\text{slice width})/2$. The total error in distance for dissolving, therefore, is $\Delta x_s + \Delta x_w$.

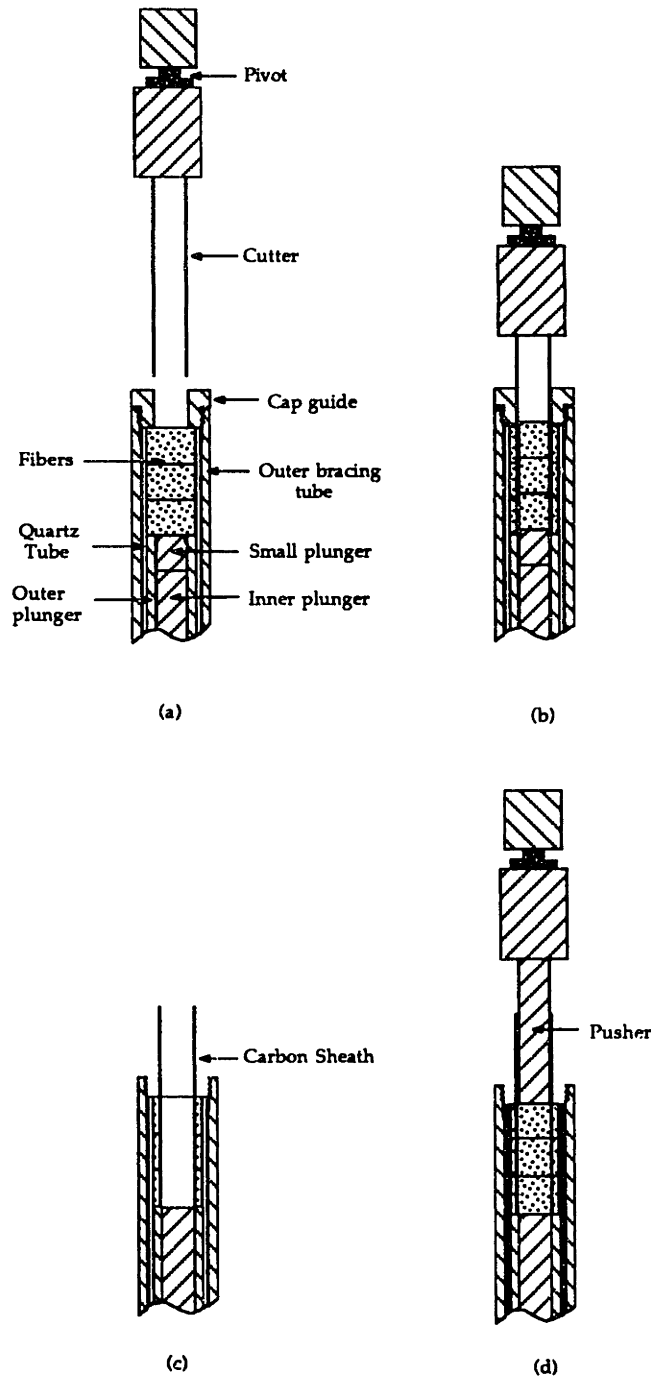


Figure (A-4.1) - Procedure for coring Saffil™ fibers (see Appendix (4.1) for details):

- (a) Sample encapsulated in apparatus
- (b) Fibers cut and pushed into knife-edge cutter
- (c) Carbon sheath inserted
- (d) Inner cores of preform replaced inside Grafoil™ sheath

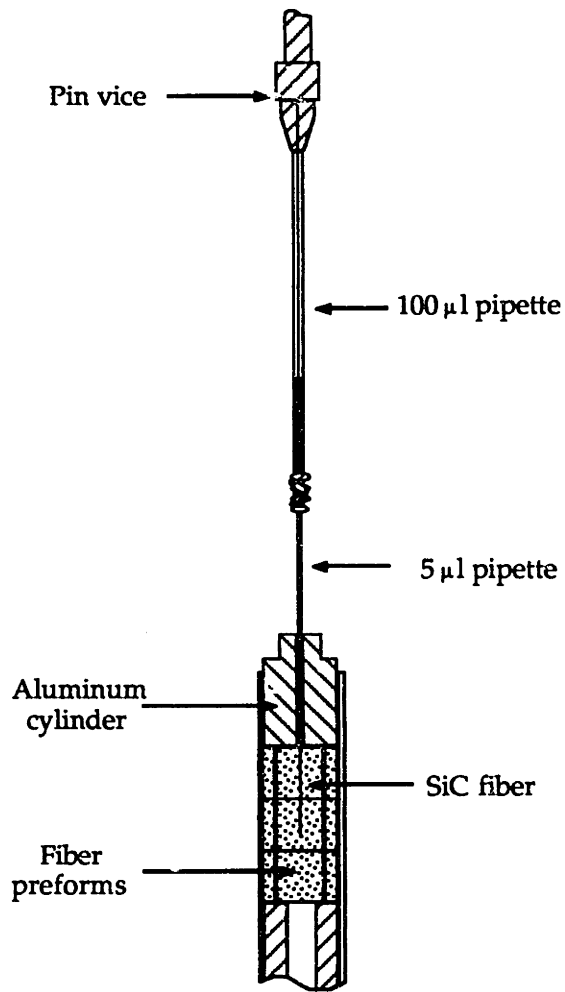


Figure (A-4.2) - Schematic illustrating the method of drilling the SiC monofilament into the preform core.

REFERENCES

- Anderson, W. G. (1987). "Wettability Literature Survey - Part 5: The Effects of Wettability on Relative Permeability." Journal of Petroleum Technology 39(11): 1453-1468.
- Andrews, R. M. and A. Mortensen (1991). "Lorentz Force Infiltration of Fibrous Preforms." Metallurgical Transactions : in print.
- Ban, K., T. Arai, et al. (1985). Method for Production of Fiber-Reinforced Composite Material. 4,506,721. U.S..
- Barry, S. I. and G. K. Aldis (1990). "Comparison of Models for Flow Induced Deformation of Soft Biological Tissue." Journal of Biomechanics 23(7): 647-654.
- Bear, J. (1972). Dynamics of Fluids in Porous Media. New York, American Elsevier.
- Bear, J. and Y. Bachmat (1990). Introduction to Modeling of Transport Phenomena. Dordrecht, The Netherlands, Kluwer Academic Publishers.
- Beavers, G. S., A. Hajji, et al. (1981). "Fluid Flow Through a Class of Highly Deformable Porous Media Part I: Experiments with Air." Journal of Fluids Engineering 103(9): 432-439.

- Beavers, G. S. and T. A. Wilson (1975). "Flow through a Deformable Porous Material." Journal of Applied Mechanics (9): 598-602.
- Beavers, G. S., K. Wittenberg, et al. (1981). "Fluid Flow Through a Class of Highly Deformable Porous Media Part II: Experiments with Water." Journal of Fluids Engineering 103(9): 440-444.
- Biot, M. A. (1955). "Theory of Elasticity and Consolidation for a Porous Anisotropic Solid." Journal of Applied Physics 26(2): 182-185.
- Biot, M. A. (1957). "The Elastic Coefficients of the Theory of Consolidation." Journal of Applied Mechanics 24: 594-601.
- Brandes, E. A., Ed. (1983). Smithells Metals Reference Book. London, Butterworths.
- Clyne, T. W. and J. F. Mason (1987). "The Squeeze Infiltration Process for Fabrication of Metal-Matrix Composites." Metallurgical Transactions 18A(August): 1519-1530.
- Dave, R. (1990). "A Unified Approach to Modeling Resin Flow During Composite Processing." Journal of Composite Materials 24(1): 23-41.

- Dave, R., J. L. Kardos, et al. (1987). "A Model for Resin Flow During Composite Processing: Part 1- Gneral Mathematical Development." Polymer Composites 8(1): 29-38.
- Dullien, F. A. L. (1979). Porous Media, Fluid Transport and Pore Structure. New York, Academic Press.
- Fisher, R. F. (1982). "The Water Permeability of Basement membrane Under Increasing Pressure: Evidence for a New Theory of Permeability." Proceedings of the Royal Society of London B 216: 475-496.
- Fisher, R. F. (1988). "The Derformation Matrix Theory of Basement Membrane: A Study of Water Flow Through Elastic and Rigid Filaments in the Rat." Journal of Physiology 406: 1-14.
- Fukunaga, H. (1988). Squeeze Casting Processes for Fiber Reinforced Metals and their Mechanical Properties. International Symposium on Advances in Cast Reinforced Metal Composites, Chicago, Illinois, USA, ASM International.
- Fukunaga, H. and K. Goda (1984). "Fabrication of Fiber Reinforced Metal by Squeeze Casting (Pressurized Infiltration Process of Molten Aluminum to Continuous Glass Fiber Bundle)." Bulletin of the Japan Society of Mechanical Engineers 27(228): 1245-1250.
- Fukunaga, H. and K. Goda (1985). "Formation and Role of the Solidified Layer on a Fiber during the Fabrication of Fiber Reinforced Metal

by the Liquid Process." Journal of the Japan Institute of Metals 49(1): 78-83.

Garg, S. K. and A. Nur (1973). "Effective Stress Laws for Fluid-Saturated Porous Rocks." Journal of Geophysical Research 78(26): 5911-5921.

Greenkorn, R. A. (1983). Flow Phenomena in Porous Media. New York, Marcel Dekker.

Gutowski, T. G., T. Morigaki, et al. (1987). "The Consolidation of Laminate Composites." Journal of Composite Materials 21(2): 172-188.

Holmes, M. H. and V. C. Mow (1990). "The Nonlinear Characteristics of Soft Gels and Hydrated Connective Tissues in Ultrafiltration." Journal of Biomechanics 23(11): 1145-1156.

Hubbert, M. K. and W. W. Rubey (1959). "Role of Fluid Pressure in Mechanics of Overthrust Faulting. I. Mechanics of Fluid-Filled Porous Solids and Its Application to Overthrust Faulting." Journal of the Geological Society of America 70: 115-166.

Imai, T., Y. Nishida, et al. (1987). "Potassium Titanate Whisker-Aluminum Composite." Journal of Materials Science Letters 6: 343-345.

Jackson, G. W. and D. F. James (1986). "The Permeability of Fibrous Porous Media." The Canadian Journal of Chemical Engineering 64(June): 364-374.

Jarry, P., A. Dubus, et al. (1990). Influence of Matrix Solidification during Infiltration on the Structure of a Cast Fibre Reinforced Alloy. F. Weinberg International Symposium on Solidification Processing, Hamilton, Ontario, Canada, Pergamon Press.

Kenyon, D. E. (1976). "The Theory of an Incompressible Solid-Fluid Mixture." Archive for Rational Mechanics and Analysis 62: 131-147

Kenyon, D. E. (1976). "Thermostatistics of Solid-Fluid Mixtures." Archive for Rational Mechanics and Analysis 62: 117-130.

Kloucek, F. and R. F. Singer (1986). Influence of Processing on the Mechanical Properties of SiC Whisker Reinforced Aluminum Composites. Materials Science for the Future: 31st International SAMPE Symposium and Exhibition, Los Angeles, CA, SAMPE.

Kwan, M. K., W. M. Lai, et al. (1990). "A Finite Deformation Theory for Cartilage and other Soft Hydrated Connective Tissues- I. Equilibrium Results." Journal of Biomechanics 23(2): 145-155.

Lambe, T. W. and R. V. Whitman (1979). Soil Mechanics. New York, John Wiley and Sons.

- Lanir, Y., S. Saub, et al. (1990). "Nonlinear Finite Deformation Response of Open Cell Polyurethane Sponge to Fluid Filtration." Journal of Applied Mechanics 57(6): 449-454.
- Lewis, R. W. and B. A. Schrefler (1987). The Finite Element Method in the Deformation and Consolidation of Porous Media. Chichester, UK, John Wiley and Sons.
- Li, X., O. C. Zienkiewicz, et al. (1990). "A Numerical Model for Immiscible Two-Phase Fluid Flow in a Porous Medium and its Time Domain Solution." International Journal for Numerical Methods in Engineering 30: 1195-1212.
- Masur, L. J. (1988). Infiltration of Fibrous Preforms by a Pure Metal. Department of Materials Science and Engineering, Massachusetts Institute of Technology.
- Masur, L. J., A. Mortensen, et al. (1987). Pressure Casting of Fiber-Reinforced Metals. Sixth International Conference on Composite Materials, ICCM 6, London, Elsevier Applied Science, London.
- Masur, L. J., A. Mortensen, et al. (1989). "Infiltration of Fibrous Preforms by a Pure Metal: Part II. Experiment." Metallurgical Transactions 20A: 2549-2557.

- Michaud, V. J. (1991). Infiltration of Fiber Preforms by a Binary Alloy.
Department of Materials Science and Engineering, Massachusetts
Institute of Technology.
- Michaud, V. J. and A. Mortensen (1991). "Infiltration of Fiber Preforms by a
Binary Alloy. Part II: Further theory and Experiments."
Metallurgical Transactions A submitted:
- Morel-Seytoux, H. J. (1969). Introduction to Flow of Immiscible Liquids in
Porous Media. Flow through Porous Media. New York, Academic
Press. 455-516.
- Mortensen, A. (1991). "Interfacial Phenomena in the Solidification
Processing of Metal Matrix Composites." Materials Science and
Engineering A135: 1 - 11.
- Mortensen, A., L. J. Masur, et al. (1989). "Infiltration of Fibrous Preforms by a
Pure Metal: Part I. Theory." Metallurgical Transactions 20A: 2535-
2547.
- Mortensen, A. and T. Wong (1990). "Infiltration of Fibrous Preforms by a
Pure Metal: Part III. Capillary Phenomena." Metallurgical
Transactions 21A(August): 2257-2263.
- Nishida, Y., H. Matsubara, et al. (1988). Silicon Nitride Whisker Reinforced
Aluminum Alloys Fabricated by Squeez Casting. Fourth Japan-

U.S. Conference on Composite Materials, Washington, D.C.,
Technomic Publishing Co., Lancaster - Basel.

Nur, A. and J. D. Byerlee (1971). "An Exact Effective Stress Law for Elastic Deformation of Rock with Fluids." Journal of Geophysical Research 76(26): 6414-6419.

Parker, K. H., R. V. Mehta, et al. (1987). "Steady Flow in Porous, Elastically Deformable Materials." Journal of Applied Mechanics 54: 794-800.

Press, W. H., B. P. Flannery, et al. (1989). Numerical Recipes: The Art of Scientific Computing (Fortran version). New York, Cambridge University Press.

Rasmussen, N. W., P. N. Hansen, et al. (1991). "High Pressure Die Casting of Fibre-Reinforced Aluminium by Preform Infiltration." Materials Science and Engineering A135: 41-43.

Rasmussen, N. W., P. N. Hansen, et al. (1991). Some Properties of Fibre Reinforced Aluminium Produced by a High Pressure Die Casting Process. Metal Matrix Composites - Processing, Microstructure and Properties, 12th Risø International Symposium on Materials Science, Risø, Denmark, Risø National Laboratory, Roskilde, Denmark.

Rice, J. R. and M. P. Cleary (1976). "Some Basic Stress Diffusion Solutions for Fluid-Saturated Elastic Porous Media with Compressible

Constituents." Reviews of Geophysics and Space Physics 14(2):
227-241.

Scheidegger, A. E. (1974). The Physics of Flow through Porous Media.
Toronto, University of Toronto Press.

Scherer, G. W. (1989). "Measurement of Permeability- I. Theory." Journal of
Non-Crystalline Solids 113: 107-118.

Trevino, L., K. Rupel, et al. (1991). "Analysis of Resin Injection Molding in
Molds with Preplaced Fiber Mats. I: Permeability and
Compressibility Measurements." Polymer Composites 12(1): 20-
29.

Weast, R. C., Ed. CRC Handbook of Chemistry and Physics. Boca Raton, FL,
CRC Press, Inc.

Yang, Y. W., G. Zografis, et al. (1988). "Capillary Flow Phenomena and
Wettability in Porous Media. II - Dynamic Flow Studies." Journal
of Colloid and Interface Science 122(1): 35-46.

Young, W. B., K. Rupel, et al. (1991). "Analysis of Resin Injection Molding in
Molds with Preplaced Fiber Mats. II: Numerical Simulation and
Experiments of Mold Filling." Polymer Composites 12(1): 30-38.

Zienkiewicz, O. C. and T. Shiomi (1984). "Dynamic Behaviour of Saturated
Porous Media; the Generalized Biot Formulation and its

Numerical Solution." International Journal for Numerical and Analytical Methods in Geomechanics 8: 71-96.

BIOGRAPHICAL NOTE

Jared Lee Sommer was born in Salt Lake City, Utah on October 31, 1960. He is the third of nine children. He attended Woods Cross High School, was involved in math clubs, band, and forensics, and earned money by teaching piano lessons.

After graduation, Jared was called to serve on an LDS (Mormon) mission to Fukuoka, Japan. He lived in various cities and villages throughout southern Japan for approximately two years.

After returning in 1982, Jared attended the University of Utah and graduated Cum Laude in June 1985 with a B. S. in Metallurgy. During the summers of 1983 to 1985, he was employed at Technical Research Associates (Salt Lake City, Utah) as a Research Technician.

Jared entered the graduate school of Massachusetts Institute of Technology in Metallurgy in September 1985. He minored in Japanese and graduated with a doctorate in October 1991.